Numerical Investigation and Extension of Quadrature-Based Moment Methods for Population Balances

Von der Fakultät 1 MINT - Mathematik, Informatik, Physik,
Elektro- und Informationstechnik
der Brandenburgischen Technischen Universität Cottbus-Senftenberg
genehmigte Dissertation
zur Erlangung des akademischen Grades eines

Doktors der Naturwissenschaften
(Dr. rer. nat.)

vorgelegt von

Michele Pütz
geboren am 5. Mai 1988 in Lindlar

Vorsitzender:	Prof. Dr. rer. nat. habil. Michael Breuß
Gutachter:	Prof. Dr.-Ing. Michael Oevermann
Gutachter:	Prof. Dr. rer. nat. Carsten Hartmann
Gutachter:	Prof. Dr. rer. nat. habil. Volker John

Tag der mündlichen Prüfung: 29. November 2023

DOI: https://doi.org/10.26127/BTUOpen-6575

Abstract

Particulate systems can be statistically described by a number density function (NDF) that maps an N-dimensional vector of internal coordinates, which represent relevant particle properties such as size and velocity, to a number density. The evolution of the NDF is governed by a partial integro-differential equation, referred to as population balance equation (PBE). In the general case of transient and spatially inhomogeneous systems where additional dependencies on time and three-dimensional physical space must be considered, the PBE is $(N + 4)$-dimensional. Thus, numerically solving the PBE using common discretization methods requires a vast amount of computational resources and is, in many cases, practically impossible. Whenever only macroscopic quantities are of interest, a common approach to reduce the dimensionality of the problem is to eliminate the dependence on the N-dimensional internal-coordinate vector by solving not for the NDF but only for a set of its moments. The governing system of moment equations can be derived directly from the underlying PBE. This moment transformation, however, results in unclosed integral terms where the unknown NDF still appears in the integrand. One way to close the system of moment equations is to approximate the unclosed integral terms using an n-point Gaussian quadrature formula whose nodes and weights can be computed from $2n$ moments. The procedure of taking a set of moments to compute a Gaussian quadrature rule, which is, in turn, used to close the moment equations, is known as the quadrature method of moments (QMOM). It gave rise to an entire family of derived methods, the quadrature-based moment methods (QBMMs). The objective of this thesis is to contribute to the advancement of QBMMs, which includes the formulation of quadrature-based moment models for different physical phenomena and, in particular, the investigation and development of numerical methods. The research presented in this thesis can be divided into three major parts.

The first part involves the formulation of an established Lagrangian model for the breakup of droplets for QBMMs with droplet diameter as the only internal coordinate, and the numerical investigation with the QMOM as well as the extended QMOM (EQMOM), a QBMM that combines the idea of the QMOM with the reconstruction of a continuous NDF. The numerical tests include two simple configurations characterized by initially monodisperse populations, which can theoretically be exactly represented by the QMOM, and a more realistic configuration with initially log-normally distributed diameters. The results indicate that the approximations are reasonably accurate when the solved system consists of at least six moment equations, with the EQMOM providing no advantages for the specific configurations investigated.

In the second part, a quadrature-based moment model for the effects of fluid turbulence on particle velocities is formulated based on a simplified microscopic model and the derived PBE, which takes the form of a Fokker-Planck equation with nonlinear and non-smooth terms. The corresponding integrals in the derived moment equations are the source of large errors when using the QMOM with an n-point Gaussian quadrature, with the sign depending on the parity of n. Based on this information, the Gauss/anti-Gauss QMOM (GaG-QMOM) is proposed that uses an alternative quadrature formed by the average of an ordinary Gaussian and an anti-Gaussian quadrature. The conducted numerical studies of univariate test cases with analytical reference solutions show that the GaG-QMOM is able to significantly reduce the errors compared to the QMOM and the EQMOM. In addition to the GaG-QMOM, another novelty is the modification of the second-order strong-stability preserving Runge-Kutta method to guarantee the preservation of moment realizability, which is the property of a moment sequence to correspond to at least one valid non-negative NDF, in the presence of phase-space diffusion. The numerical results show that it can serve as a suitable alternative scheme in cases where moment realizability is expected to be critical.

The third part is concerned with the numerical exploration of the core algorithm of most QBMMs in terms of performance and accuracy. The algorithm consists of, first, computing n pairs of recurrence coefficients of the associated orthogonal polynomials from $2n$ moments, second, solving a symmetric tridiagonal eigenvalue problem of size n to obtain n quadrature nodes and weights, and

third, evaluating the integral terms in $2n$ moment equations. The results indicate that the contribution of the first step to compute the recurrence coefficients from moments to the overall computational costs is negligible. Instead, the primary focus should be on the fast solution of the eigenvalue problem and, possibly, on the efficient implementation of the moment source term evaluation, which becomes important when second-order processes, i.e. processes with particle-particle interactions, are involved.

The derived models and the conducted numerical investigations summarized above as well as the software implemented in the course of this work provide a solid foundation for future research tasks like the extension and application of the developed methods to multivariate problems.

Kurzfassung

Teilchensysteme können statistisch durch eine Anzahldichtefunktion (number density function, NDF) beschrieben werden, die einen N-dimensionalen Vektor von internen Koordinaten, welche relevante Teilcheneigenschaften wie Größe und Geschwindigkeit darstellen, auf eine Anzahldichte abbildet. Die Änderung der NDF folgt einer partiellen Integro-Differentialgleichung, die Populationsbilanzgleichung (population balance equation, PBE) genannt wird. In dem allgemeinen Fall eines transienten, räumlich inhomogenen Systems, bei dem Abhängigkeiten von der Zeit und vom dreidimensionalen physikalischen Raum zu berücksichtigen sind, ist die PBE $(N + 4)$-dimensional. Daher erfordert die numerische Lösung der PBE mit üblichen Diskretisierungsmethoden enorme Rechenressourcen and ist in vielen Fällen praktisch nicht durchführbar. Ist man nur an makroskopischen Größen interessiert, so ist ein üblicher Ansatz zur Reduktion der Dimensionalität die Eliminierung der Abhängigkeiten vom Vektor der internen Koordinaten durch Lösung nicht etwa nach der NDF selbst, sondern lediglich nach einigen ihrer Momente. Das entsprechende System von Momentengleichungen kann direkt aus der zugrundeliegenden PBE hergeleitet werden. Diese Momententransformation hat jedoch ungeschlossene Integralterme zur Folge, welche die NDF noch immer im Integranden enthalten. Ein Mittel das Gleichungssystem zu schließen ist, die Integrale durch eine n-Punkt-Gauß-Quadraturformel anzunähern, deren Stützstellen und Gewichte aus $2n$ Momenten berechnet werden können. Dieses Vorgehen, aus einer Menge von Momenten eine Gauß-Quadratur zu berechnen und diese wiederum zu verwenden, um die Gleichungen für selbige Momente zu schließen, ist als QMOM (quadrature method of moments) bekannt. Aus dieser Methode entstand eine ganze Familie von Verfahren: die quadraturbasierten Momentenmethoden (quadrature-based moment methods, QBMMs). Das Ziel dieser Arbeit ist es, einen Beitrag zur Weiterentwicklung von QBMMs zu leisten, der die Formulie-

rung von Modellen für verschiedene physikalische Vorgänge und insbesondere auch die Untersuchung und Entwicklung numerischer Methoden umfasst. Die vorgestellte Forschungsarbeit lässt sich im Wesentlichen in drei Teile gliedern.

Der erste Teil befasst sich mit der Formulierung eines weit verbreiteten Lagrange'schen Modells für den Zerfall von Tropfen für QBMMs, wobei die einzige interne Koordinate der Tropfendurchmesser ist, sowie der numerischen Untersuchung mit QMOM und EQMOM (extended QMOM), einer Quadraturmethode, die die grundlegende Idee von QMOM mit der Rekonstruktion einer stetigen NDF verbindet. Die numerischen Untersuchungen umfassen zwei einfache Konfigurationen mit anfangs monodispersen Teilchenpopulationen, die theoretisch exakt durch QMOM dargestellt werden können, sowie eine realistischere Konfiguration mit zu Beginn log-normal verteilten Teilchendurchmessern. Die Ergebnisse zeigen, dass eine relativ hohe Genauigkeit der Näherungslösung erreichbar ist, sofern das gelöste Gleichungssystem aus mindestens sechs Momentengleichungen besteht, wobei EQMOM speziell für die hier untersuchten Fälle keinerlei Vorteile bringt.

Im zweiten Teil wird ein quadraturbasiertes Momentenmodell für die Effekte von Turbulenz in einem umgebenden Fluid auf die Teilchengeschwindigkeit hergeleitet, das auf einem vereinfachten Mikroskalenmodell und der daraus abgeleiteten PBE beruht, die die Form einer Fokker-Planck-Gleichung mit nicht-linearen und nicht-glatten Termen annimmt. Die entsprechenden Integrale in den daraus folgenden Momentengleichungen sind die Ursache großer Fehler, wenn QMOM mit einer n-Punkt-Gauß-Quadratur verwendet wird, wobei die Parität von n deren Vorzeichen bestimmt. Darauf basierend wird eine neue Methode, die sogenannte Gauss/anti-Gauss-QMOM (GaG-QMOM), vorgestellt, die eine alternative Quadraturformel, nämlich das Mittel aus einer gewöhnlichen Gauß-Quadratur und einer Anti-Gauß-Quadratur verwendet. Die durchgeführten numerischen Untersuchungen von univariaten Testfällen mit analytischen Referenzlösungen zeigen, dass GaG-QMOM die Fehler verglichen mit QMOM und EQMOM in signifikantem Maß verringern kann. Eine weitere Neuheit neben GaG-QMOM ist eine Modifikation des stark stabilitätserhaltenden Runge-Kutta-Verfahrens zweiter Ordnung (RK2SSP), die die bedingungslose Erhaltung der Momentenrealisierbarkeit (die Eigenschaft einer Menge von Momenten, mindestens einer nicht-negativen NDF zu entsprechen) in Anwesen-

heit von Phasenraumdiffusion sicherstellt. Die Berechnungsergebnisse weisen darauf hin, dass das Verfahren eine geeignete Alternative für Anwendungen darstellt, in denen Probleme in Zusammenhang mit Momentenrealisierbarkeit zu erwarten sind.

Der dritte Teil beschäftigt sich mit der numerischen Untersuchung des Kernalgorithmus der meisten QBMMs in Hinblick auf Rechenkosten und Genauigkeit. Im Wesentlichen besteht der Algorithmus erstens aus der Berechnung von n Paaren von Rekursionskoeffizienten der zugehörigen orthogonalen Polynome aus $2n$ Momenten, zweitens der Lösung eines tridiagonalen symmetrischen Eigenwertproblems der Größe n, um die Quadraturknoten und -gewichte zu erhalten, und drittens der Auswertung der Integralterme in den $2n$ Momentengleichungen. Die Ergebnisse weisen darauf hin, dass der Beitrag des ersten Schrittes zur Berechnung der Rekursionskoeffizienten bezogen auf die gesamten Rechenkosten vernachlässigbar ist. Stattdessen sollte die schnelle Lösung des Eigenwertproblems im Vordergrund stehen und gegebenenfalls die effiziente Auswertung der Momentenquellterme, die bei Vorgängen zweiter Ordnung, also Vorgängen mit Teilchen-Teilchen-Interaktionen, bedeutend werden.

Die hergeleiteten Modelle sowie die durchgeführten numerischen Untersuchungen und die im Rahmen dieser Arbeit implementierte Software bilden eine solide Grundlage für weiterführende Forschungsarbeiten wie zum Beispiel die Erweiterung und Anwendung der entwickelten Verfahren auf multivariate Probleme.

Acknowledgements / Danksagungen

Ich möchte nun die Gelegenheit nutzen, um jenen meinen Dank auszusprechen, ohne deren wertvolle Unterstützung die Fertigstellung dieser Arbeit kaum möglich gewesen wäre. Auch wenn es viele Dinge und vor allem Menschen gibt, denen Dankbarkeit gebührt, werde ich mich an dieser Stelle namentlich auf diejenigen beschränken, die direkt zur Fertigstellung dieser Dissertation beigetragen haben.

Zuallererst gilt mein Dank Prof. Dr.-Ing. Michael Oevermann, der meine Arbeit über sieben Jahre lang betreut hat, mir die Freiheit ließ, wissenschaftliche Aufgabenstellungen eigenständig auszuwählen und zu bearbeiten, mir jedoch bei Bedarf immer mit Rat und Tat zur Seite stand. Seine hervorragende Betreuung, aber auch das gute private Verhältnis und die angenehme Arbeitsatmosphäre, die er geschaffen hat, haben dafür gesorgt, dass die zahlreichen Tiefen während meiner Promotionszeit fast immer durch die Freude an der Arbeit überwogen wurden.

Außerdem möchte ich mich besonders bei Dr.-Ing. Martin Pollack bedanken, der mir die ganze Thematik durch seine ausführlichen Erklärungen erst zugänglich gemacht hat und auch im weiteren Verlauf durch den interessanten Austausch eine wertvolle Unterstützung war.

Des Weiteren danke ich dem Vorsitzenden der Promotionskommission Prof. Dr. rer. nat. habil. Michael Breuß sowie den Gutachtern Prof. Dr. rer. nat. Carsten Hartmann und Prof. Dr. rer. nat. habil. Volker John, die ihre wertvolle Zeit für die Begutachtung meiner Arbeit geopfert haben.

Neben den Personen, die ich nun namentlich genannt habe, möchte ich mich auch bei den Institutionen und den entsprechenden verantwortlichen Personen bedanken, die mir durch Zurverfügungstellung eines geeigneten Arbeitsum-

feldes und/oder Finanzierung meine Promotion ermöglicht haben. Das betrifft die Chalmers University of Technology in Göteborg, bei der ich 2016 meine wissentschaftliche Arbeit als Doktorand begann, und die schwedische Energieagentur (Energimyndigheten) für die Finanzierung dieser Stelle, das Fachgebiet STFS der TU Darmstadt für die Ermöglichung meiner dortigen Forschungsaufenthalte und selbstverständlich die BTU Cottbus-Senftenberg, an der ich von 2019 bis 2023 als wissenschaftlicher Mitarbeiter tätig war und letztendlich meine Promotion abschließen konnte.

Zu guter Letzt gilt mein Dank natürlich auch meiner Familie und Freunden, die ein wertvoller Rückhalt waren und mich auch während der von Frust geplagten Phasen ertragen haben. Vielen Dank.

Notation

To improve readability of the presented mathematical relationships, some notational conventions used throughout this thesis are clarified below.

Scalars, vectors and matrices

The notation of scalar, vector and matrix variables will, if not explicitly stated otherwise, follow some general conventions:

- Scalar variables are denoted by italic letters (Latin or Greek), e.g. x.
- Vector variables are written as bold italic letters, e.g. $\boldsymbol{x}$.
- Random and Lagrangian scalar or vector variables are indicated by upper case, e.g. X or $\boldsymbol{X}$, respectively.
- Matrices are denoted by upright bold letters, e.g. $\mathbf{X}$.
- Besides bold type, vectors and matrices may be denoted in terms of their elements in parentheses, i.e. $\boldsymbol{x} = (x_i)$ and $\mathbf{X} = \left(x_{ij}\right)$.

Einstein summation notation

Some of the mathematical relationships in this thesis, in particular those involving multivariate calculus, will make use of the Einstein summation convention, where repeated indices imply summation. For example, consider a matrix $\mathbf{A} = \left(a_{ij}\right) \in \mathbb{B}^{m \times n}$ and a vector $\boldsymbol{b} = \left(b_j\right) \in \mathbb{B}^n$ for some field $\mathbb{B}$. Then the matrix-vector product $\boldsymbol{c} = (c_i) = \mathbf{A}\boldsymbol{x}$ can be written as

$$c_i = \sum_{j=1}^{n} a_{ij} b_j = a_{ij} b_j, \quad i = 1, \ldots, m. \tag{1}$$

Similarly, multiple repeated indices imply multiple sums.

Integration with respect to vectors

Let $\boldsymbol{y} = (y_i) \in \mathbb{B}$ be an n-dimensional vector and $g : \mathbb{B} \to \mathbb{R}$ an arbitrary integrable function. Then, for brevity, the definite integral over $\mathbb{B}$ is written as

$$\int_{\mathbb{B}} g(\boldsymbol{y})\,\mathrm{d}\boldsymbol{y} \coloneqq \iint \cdots \int_{\mathbb{B}} g(\boldsymbol{y})\,\mathrm{d}y_1\,\mathrm{d}y_2 \cdots \mathrm{d}y_n. \tag{2}$$

Probability theory

Consider an n-dimensional random variable $\boldsymbol{Y} \in \mathbb{B}$ with the distribution $\mathcal{P}$, which is denoted by

$$\boldsymbol{Y} \sim \mathcal{P}. \tag{3}$$

Then, if $\mathcal{P}$ has probability density $p(\boldsymbol{y})$, the expectation of a general expression $g(\boldsymbol{Y})$ is denoted by

$$\langle g(\boldsymbol{Y}) \rangle \coloneqq \mathrm{E}\left[g(\boldsymbol{Y})\right] = \int_{\mathbb{B}} g(\boldsymbol{y}) p(\boldsymbol{y})\,\mathrm{d}\boldsymbol{y}. \tag{4}$$

The explicit labeling as a random variable is not necessarily employed here as it is clearly evident from the context, i.e. $\langle g(\boldsymbol{Y}) \rangle = \langle g(\boldsymbol{y}) \rangle$. Moreover, the definition in (4) is extended to not only PDFs but any non-negative weight or density function p.

The probability of an event A is denoted by $\Pr\{A\}$. For example, the probability of finding the value of the random variable Y on the interval (a, b) is expressed as

$$\Pr\{a < Y < b\} = \int_a^b p(y)\,\mathrm{d}y. \tag{5}$$

Contents

1. Introduction

1.1. Motivation: Some Physical Problems

A population balance equation (PBE) provides a statistical description of a particulate system. Technically, considering that matter is composed of atoms and molecules, everything can be thought of as a particulate system. For example, single-phase flows can be statistically described by a form of the well-known Boltzmann equation, which governs the behavior of a collection of molecular entities (particles) constituting a non-equilibrium gas and is mathematically very similar to a generalized PBE. However, in many of the interesting particulate systems, the relevant length scales are significantly larger than the molecular scale and particles interact with a surrounding fluid. In that case, the system is referred to as dispersed multiphase flow. More precisely, dispersed multiphase flows are dynamic systems comprising two or more phases, at least one of which consists of fine particles in any state of matter—solid, liquid or gaseous—dispersed in a fluid. They are ubiquitous in nature and technology, which has led to tremendous research efforts to gain a thorough understanding of the underlying physics and the ability to accurately predict the evolution of such systems. For that purpose, numerical simulation is an important tool besides theoretical and experimental work.

Sprays are an example of liquid droplets dispersed in gas. They play a major role in numerous industrial applications, e.g. spray drying, a widely used technology to produce powders for foods, detergents and pharmaceuticals [102, 110]. Understanding and improving the technology is crucial since inadequate design of the spray dryer significantly affects the efficiency of the process as well as product quality and may, in the case of foods and pharmaceutical products, even be hazardous to human health. Therefore, considerable research has been carried out into the proper numerical modeling and simulation of the pro-

cess [11, 163]. Another example of droplet-gas flows that has recently received increased attention over the course of the COVID-19 pandemic is the airborne transmission of infectious diseases, where numerical simulation has been used to predict the concentration of virus-laden droplets and the associated risk of infection in various situations [168, 174, 176].

Solid-gas flows are very common in a wide range of technical systems, e.g. fluidized-bed reactors [109, 169], which are used for many chemical processes. One application of fluidized-bed reactors is biomass gasification [68], a process that has gained significance due to the need of renewable energy resources and has been the subject of countless numerical studies in recent years, e.g. [118, 175]. Solid-gas systems also appear in many natural phenomena, e.g. avalanches and landslides, where accurate numerical models may predict the extent of such disasters and thus help reduce the damage [128].

Bubbly flows, i.e. flows involving dispersed gaseous particles in liquid, are also common in technical applications. An example is the flow of water occurring in the coolant systems of nuclear reactors, where the absorption of heat from nuclear fuel rods results in boiling and the formation of bubbles [39]. It is well known that a failure of the coolant system may lead to a catastrophic accident. To prevent that, different tools are employed for safety analysis, one of which is numerical simulation [39, 79].

The examples above are only a few[1] highlighting the importance of dispersed multiphase flows and the need to develop accurate mathematical models and adequate methods for the efficient numerical solution.

1.2. Current State of Research

Owing to their omnipresence in nature and technology, particulate systems and dispersed multiphase flows have been topics of research for centuries. With the rapid growth in computing power over the past decades, the development of suitable models for the numerical simulation of such systems has become

[1] Several of the mentioned examples, in particular those of industrial applications, were taken from Refs. [109] and [110], where the interested reader can find more detailed descriptions accompanied by explanatory illustrations as well as further examples.

increasingly important. Two fundamental criteria for the classification of those models are, first, the distinction between Eulerian and Lagrangian descriptions of the particulate system, and second, the considered range of length scales and the corresponding physical phenomena that must be taken into account. Based on the latter, models can be classified as microscale, mesoscale or macroscale model, which is illustrated in Figure 1.1.

Microscale models aim to capture physics on the particle or sub-particle scale. Examples of microscale models are the volume of fluid method [69], the level-set method [117] and the immersed boundary method with direct forcing [162]. While the former two are commonly applied to problems involving deformable (typically liquid or gaseous) particles, the latter is suitable when the dispersed

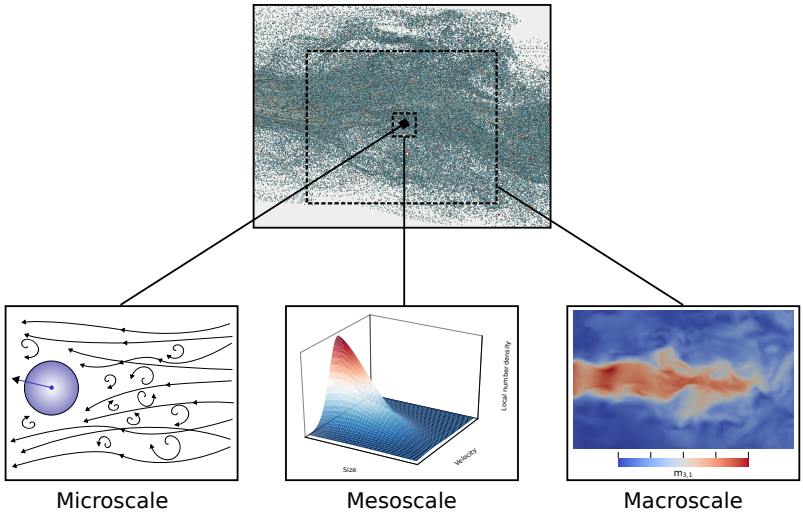

Figure 1.1.: Schematic illustration of different modeling length scales for dispersed systems. Microscale models (left) are illustrated by a single particle in a turbulent flow field, mesoscale models (center) by a bivariate number density function for size and velocity, and macroscale models (right) by a qualitative visualization of the (3,1)th-order moment of the size-velocity distribution, which is proportional to the total local momentum.

phase consists of solid particles. All mentioned examples have in common that the dispersed particles are resolved on the spatial numerical grid while other methods treat particles as discrete entities, e.g. the discrete element method (DEM), a Lagrangian approach that is primarily employed for the simulation of granular flows, i.e. systems of solid particles [25, 66]. Naturally, microscale models provide the highest level of detail, though at the price of computational requirements that may be prohibitive in many physical applications.

Mesoscale models contain no information on the state of individual particles but, instead, provide a statistical description of a particle population in the form of some distribution function. One such distribution function is given by the number density function (NDF) $f(\boldsymbol{\xi}, \boldsymbol{x}; t)$ that maps a vector of internal coordinates $\boldsymbol{\xi}$, representing relevant particle properties such as size and velocity, to a number concentration at position $\boldsymbol{x}$ and time t. For probabilistic systems, a probability density function (PDF) may be a more suitable and intuitive mesoscopic description. However, it is important to note that, even though the physical interpretations may differ, the only mathematical difference between the two is a normalization constant. Thus, the methods suitable for the numerical solution are practically identical. Here it will be assumed that the particulate system of interest is described by a NDF. The evolution of the particle population is then governed by a transport equation for the NDF referred to as population balance equation (PBE). In a very general form, it can be expressed as

$$\frac{\partial f(\boldsymbol{\xi}, \boldsymbol{x}; t)}{\partial t} = \mathcal{D} f(\boldsymbol{\xi}, \boldsymbol{x}; t) + \mathcal{S}(f, \boldsymbol{\xi}, \boldsymbol{x}), \tag{1.1}$$

where $\mathcal{D}$ is a linear differential operator with respect to $\boldsymbol{x}$ and $\boldsymbol{\xi}$, and $\mathcal{S}$ is a functional representing the source term due to discrete events such as collisions.

Various numerical techniques exist to approximate mesoscale solutions, one of which is the direct numerical solution of the PBE. This can and has been done using well-established methods for the solution of partial differential equations (PDEs), e.g. finite difference methods [103, 104], finite volume methods [15, 41, 43] and finite element methods [52, 75, 95]. Techniques referred to as class methods or sectional methods [70, 92] are also based on a discretization of the PBE in internal-coordinate space (phase space). They are mostly equivalent to finite difference methods with additional considerations regarding the treatment of the source term $\mathcal{S}$. The recent review article by Singh et al. [151] gives a com-

prehensive summary of different methods for the solution of PBEs focusing on breakage-aggregation problems with size as the only internal coordinate. Most of those methods can be easily transferred to the multivariate case. However, as a consequence of the exponential complexity with respect to dimensionality, the solution quickly becomes computationally intractable with a growing number of internal coordinates.

In contrast to the mentioned deterministic methods of discretization, Monte-Carlo methods [56, 153] are an approach to approximate a solution to the PBE by simulating the physical behavior of a particulate system using random samples of the NDF. They are similar to Lagrangian microscale models like the DEM in that they solve the governing equations for individual particles, though only for representative samples of the distribution instead of actual physical particles. Most of the popular Eulerian-Lagrangian methods for dispersed multiphase flows can be regarded as Monte-Carlo methods. They are based on an Eulerian description of the continuous fluid and Lagrangian tracking of representative computational particles, so-called parcels, to describe the evolution of the dispersed phase. Eulerian-Lagrangian methods have been used in countless numerical studies related to dispersed multiphase flows, e.g. [65, 84, 163, 168]. Despite their widespread use, however, Eulerian-Lagrangian methods have major drawbacks: First, in polydisperse inhomogeneous systems, a large number of Lagrangian samples is needed to sufficiently resolve the NDF and obtain an accurate solution, which implies high computational costs. Second, coupling of the continuous and the dispersed phase is complicated by different reference frames and requires additional cell search and interpolation algorithms. Third, spatial inhomogeneities in the particle concentration cause a load imbalance in parallel simulations on distributed-memory systems where parallelization is usually based on spatial domain decomposition. Although there are algorithms to control the particle number density and mitigate that problem [45, 157], the difficulties implicated by the Lagrangian frame of reference make Eulerian methods generally preferable in terms of the numerical treatment.

Macroscale models only capture macroscopic quantities, e.g. the total local number concentration, mass, momentum or kinetic energy. As such quantities are often the desired primary results of numerical simulations and microscale and mesoscale models generally require a large amount of computational re-

sources, macroscale models are, in many cases, the preferred approach. Macroscopic quantities like those mentioned above correspond to integral properties of the particle distribution function and can be expressed in terms of its integer moments. The transport equations governing the evolution of moments can be derived from the PBE (1.1) by integration, e.g. for the kth-order moment with respect to a single internal coordinate $\xi \in \Omega$,

$$\frac{\partial m_k(\boldsymbol{x};t)}{\partial t} = \int_\Omega \xi^k \mathcal{D} f(\xi,\boldsymbol{x};t)\,\mathrm{d}\xi + \int_\Omega \xi^k \mathcal{S}(f,\xi,\boldsymbol{x})\,\mathrm{d}\xi, \quad k = 0,1,\ldots \tag{1.2}$$

Evidently, the NDF still appears in the resulting set of equations, and additional methods are needed to solve this closure problem.

A simple method to close the moment equations is the method of moments with interpolative closure (MOMIC) [51], which is suitable for cases where the RHS of (1.2) can be expressed in terms of the known integer moments as well as fractional moments, so that the latter can be approximated by interpolation from the former. Whenever this is possible MOMIC is a very efficient approach to close the moment equations. However, many, if not most PBEs corresponding to realistic physical problems are more complex and cannot be expressed by fractional moments, see e.g. [96, Sec. 7.3.1]. Among the numerous closure methods developed for such cases, two main classes can be distinguished: first, presumed-NDF methods, and second, quadrature-based moment methods (QBMMs).

Presumed-NDF methods are, as the name implies, based on a presumed functional form of the NDF. The simplest presumption would be that of uniform particle properties (monodisperse population), see e.g. [80] for an application involving coagulation and sintering. In that case, the NDF is merely a Dirac delta function located at the mean m_1/m_0, that is, only two moments are needed to construct a NDF of the presumed form. In general, however, this is not only a very crude approximation but also fails to capture the effects of physical phenomena that introduce statistical dispersion to the NDF, such as all diffusive processes. To account for non-negligible variance in the distribution, known families of probability distributions have been frequently used to construct a NDF from given moments. Popular choices are common two-parameter distributions such as the log-normal distribution for univariate NDFs with size as the only internal coordinate [8, 16] or the multivariate normal distribution for

velocity-based NDFs [142, 165]. Although such methods allow for the efficient reconstruction of a NDF from a few given moments, it is important to highlight that their applicability is limited to the rare cases where the shape of the NDF is known a priori [96, Sec. 4.4]. Various methods attempt to mitigate that problem using spline-based reconstruction [29, 74], linear combinations of basis functions [37] or a functional expansion for the NDF (see e.g. [62], [96, Sec. 4.4]). The latter is also the basic idea behind the finite-size domain complete set of trial functions method of moments (FCMOM) [154–156]. Another approach to overcome the limitations of presumed-NDF methods is to reconstruct the NDF that maximizes the differential entropy [106, 108], which is, according to the principle of maximum entropy [73], always the best representation of the given information. However, finding the maximum-entropy distribution is a constrained optimization problem [1, 3] whose solution quickly becomes prohibitively expensive when dealing with a larger number of (possibly multivariate) moments.

QBMMs are a family of methods to close the moment equations derived from PBEs using quadrature rules. The quadrature method of moments (QMOM) introduced by McGraw [107] was the first QBMM and the basis of many derived methods. It employs an n-point Gaussian quadrature to approximate the unclosed integral terms in the first $2n$ moment equations making use of the fact that the nodes and weights of the Gaussian quadrature rule can be calculated from the same set of $2n$ moments without knowledge of the NDF, so that the RHS of (1.2) is a function of the moments, or in other words, the system of moment equations is closed. Since the theory behind Gaussian quadrature rules is limited to univariate weight functions (the weight function corresponds to the NDF), the QMOM is inherently one-dimensional in internal-coordinate space. It has been applied to various physical processes, e.g. crystallization and precipitation [99, 100], mixing of fluidized powders [105], bubbly flows in stirred tank reactors [124], the sedimentation of raindrops [114] and kinetic problems in plasma physics [158].

Though not explicitly designed as such, the QMOM can be, and often is, interpreted as an approximation of the NDF by a weighted sum of Dirac delta functions located at the quadrature nodes [96, 98, 178], i.e. a discontinuous representation of the NDF. However, to model problems involving fluxes across phase space boundaries, such as the disappearance of droplets as a result of

complete evaporation, pointwise values and thus continuous reconstructions of the NDF are needed for an accurate solution. For this purpose, several methods have been developed to combine the idea of NDF-reconstruction with that of the QMOM, e.g. the combination of the QMOM with the maximum-entropy approach [14, 101]. Another method is the multi-Gaussian QMOM [20] that reconstructs the NDF as a weighted sum of (scaled) normal PDFs centered on the Gaussian quadrature nodes. The extended QMOM (EQMOM) [179] generalizes that approach to further kernel density functions (KDFs) incorporating the idea of the kernel density element method (KDEM) [5]. In the original work on EQMOM, beta- and gamma-PDFs were used as KDFs, of which the shape parameter was determined using an additional transported moment. The method was later extended to further types of KDFs and improved in terms of finding the KDF-parameter [126]. The EQMOM has been shown to yield accurate results for various types of problems [125, 130, 145, 158]. As an alternative to an explicit continuous reconstruction of the NDF, Fox et al. [49] recently proposed the so-called generalized QMOM, a QBMM that adopts the basic idea of the EQMOM but directly computes, based on assumptions regarding the shape of the NDF, an arbitrary number of quadrature nodes. The results of its application to breakup and aggregation problems were promising.

The above-mentioned QBMMs are all limited to one-dimensional phase space. However, most physical applications are only adequately described by a multivariate NDF. Several multivariate QBMMs making use of additional techniques and assumptions have been developed, e.g. the tensor-product QMOM (see [44, 177], [96, Sec. 3.3.4]), the conditional QMOM (CQMOM) [178] and several derived methods such as the hyperbolic version of the CQMOM [50, 122] and combinations with the EQMOM for continuous multivariate NDF-reconstructions (see [21, 130, 133], [96, Sec. 3.3.4]).

As demonstrated by the (incomplete) summary above, a good deal of research work on QBMMs has been done since the QMOM was first introduced in 1997. However, several challenges are yet to be addressed to establish QBMMs as a general practical alternative to conventional methods for the numerical simulation of particulate systems and dispersed multiphase flows. Some of those challenges are:

- *Moment realizability*: A challenge that is very specific to moment methods

is the difficult preservation of moment realizability, which is, in short, the property of a set of moments to represent at least one valid NDF. Several methods have been proposed to tackle that problem, mostly focusing on the transport in physical space $\boldsymbol{x}$ [23, 77, 85, 147, 166, 167], which is the most problematic process in terms of moment realizability. However, realizability issues related to other physical phenomena in the PBE have not received as much attention. Moreover, there is, to the author's best knowledge, no multivariate QBMM that guarantees the preservation of moment realizability in terms of the quadrature for higher-order moments.

- *Physical models*: Even though QBMMs have been applied to many different physical processes, the used models are often derived from mesoscopic models that have nice mathematical forms well-suited to QBMMs but are not consistent with common microscale descriptions, which are often more difficult, non-smooth or even discontinuous. Extending the physical models and finding ways of the appropriate numerical treatment is another major challenge to make QBMMs practically applicable to a wide range of physical problems.
- *Computational efficiency*: It is often highlighted as one of the key features of QBMMs that they are numerically efficient [32, 99, 179], yet published research concerning the computational performance of QBMMs is limited to reported CPU times without detailed information on the implementation of the algorithm [75, 99]. Detailed investigations into the performance of QBMMs and, if need be, performance optimizations are still open issues.

The purpose of the research conducted as part of this work is to help address some of these challenges, which is detailed in the following section.

1.3. Objectives and Thesis Structure

Based on the challenges formulated in the previous section, this work is intended to contribute to the further development of QBMMs for particulate systems and dispersed multiphase flows that can be statistically described by PBEs. This includes the formulation of physical models for QBMMs, the thorough in-

vestigation of existing methods from a numerical point of view, and the extension of the family of QBMMs by developing new methods. To this end, the thesis is structured as described below.

The theoretical basis of this work is described in the following two chapters, starting with the mesoscopic modeling of particulate and dispersed multiphase systems by population balances and the macroscopic description, i.e. moment equations, derived therefrom in Chapter 2. Following that, Chapter 3 deals with the theoretical foundation and important types of QBMMs for the closure of those moment equations and provides, in combination with Chapter 2, a justification for the reduction to univariate, spatially homogeneous systems for the development of new numerical methods.

The scientific novelties of this thesis are presented in Chapters 4–6. In Chapter 4, a widely used simple Lagrangian model for the breakup of liquid droplets is formulated for QBMMs, applied to a series of univariate and spatially homogeneous test configurations with increasing complexity, and compared to a reference solution obtained from a Monte-Carlo simulation using the original model.

Chapter 5 is concerned with the effect of fluid turbulence on particle velocities as well as the development and application of suitable numerical methods to solve the corresponding model equations. Based on common microscale models, fluid turbulence is taken into account by a phase-space diffusion term in the PBE that is non-smooth and thus numerically problematic for QBMMs. As an attempt to reduce the large errors associated to such problems, a novel QBMM referred to as the Gauss/anti-Gauss QMOM is developed. Moreover, a modified strong-stability preserving Runge-Kutta method for the unconditional preservation of moment realizability in the presence of phase-space diffusion is proposed. The new methods are evaluated in a series of numerical tests using simple one-dimensional configurations with analytical reference solutions.

Chapter 6 presents a detailed numerical investigation of the basic quadrature-based moment closure algorithm, which is the basis of all common QBMMs, with respect to performance and accuracy. The main objective is to compare different configurations and identify bottlenecks and potentials of optimization to help make QBMMs as efficient as possible.

Chapter 7 concludes this dissertation with a summary focusing on its scien-

tific contributions and, finally, suggestions for future research topics.

1.4. Summary of Contributions

The scientific contribution of this work can be summarized by the following novelties:

- Formulation and / or validation of physical models for QBMMs:
  - formulation of an established Lagrangian model for the breakup of liquid droplets in the QBMM-context and validation against Monte-Carlo simulations (Chapter 4),[2]
  - formulation of a model for the effect of fluid-phase turbulence on particle velocities for QBMMs and numerical investigation in one phase-space dimension in comparison to analytical reference solutions (Chapter 5, in particular Sections 5.1 and 5.4).[3]
- Development and application of new numerical methods:
  - development of the Gauss/anti-Gauss QMOM, a novel QBMM to mitigate the errors due to non-smooth integrands in the moment equations, as well as the application to turbulence-induced phase-space diffusion (Chapter 5, in particular Sections 5.2 and 5.4),[4]
  - development and numerical investigation of a new strong-stability preserving Runge-Kutta method for the realizability-preserving temporal integration of moment equations with phase-space diffusion (Chapter 5, in particular Sections 5.3 and 5.4).[5]

[2]Most of the theoretical work has been published as part of the pre-doctoral thesis (licentiate thesis) *"Numerical Modeling of Atomization in Spray Systems" (2019)* in the course of the author's research activities at Chalmers University of Technology, Gothenburg, Sweden.

[3]Parts of this work have been published in: *M. Pütz, M. Pollack, C. Hasse and M. Oevermann. "A Gauss/anti-Gauss quadrature method of moments applied to population balance equations with turbulence-induced nonlinear phase-space diffusion". Journal of Computational Physics 466 (2022), 111363. https://doi.org/10.1016/j.jcp.2022.111363*

[4]See footnote 3.

[5]See footnote 3.

- In-depth numerical investigation of the quadrature-based closure algorithm, which is an essential part of virtually every QBMM, with respect to performance, accuracy and sensitivity to input moment sequences (Chapter 6).[6]

[6]Parts of this work have been published in: *M. Pütz and M. Oevermann. "Performance and accuracy of the basic closure algorithm of quadrature-based moment methods". Journal of Computational Physics 494 (2023), 112514. https://doi.org/10.1016/j.jcp.2023.112514*

2. Statistical Description of Dispersed Systems

This chapter is intended to provide the foundation for the statistical description of particulate flows at the mesoscale and macroscale. For this purpose, the basis of the mesoscopic description, the number density function (NDF), will be presented first. Then the population balance equation (PBE), which is the differential equation governing the change of the NDF in time, physical space and phase space, will be introduced, before addressing general aspects of the macroscopic model derived therefrom in terms of moment transport equations. Finally, the mathematical representation of the carrier fluid in dispersed multiphase flows will be briefly discussed, with a focus on turbulence modeling.

2.1. Mesoscale Description of Particulate Systems

2.1.1. The Number Density Function

Let $\boldsymbol{x} \in \mathbb{R}^3$ be a position in physical space and let $\boldsymbol{\xi} \in \Omega$ be a point in N-dimensional internal-coordinate space, which may represent any set of quantifiable particle properties, e.g. some measure of particle size, velocity components, temperature, or the material composition in terms of volume or mass fractions. Then the NDF, denoted by $f(\boldsymbol{\xi}, \boldsymbol{x}; t)$, is defined such that

$$\mathrm{d}N_p = f(\boldsymbol{\xi}, \boldsymbol{x}; t)\, \mathrm{d}\boldsymbol{\xi}\, \mathrm{d}\boldsymbol{x} \tag{2.1}$$

is the expected number of particles in the physical volume $(\boldsymbol{x}, \boldsymbol{x}+\mathrm{d}\boldsymbol{x})$ and phase-space volume $(\boldsymbol{\xi}, \boldsymbol{\xi} + \mathrm{d}\boldsymbol{\xi})$ at time t. Although it is consistently described as an

average quantity (see e.g. [96, Sec 4.1], [136, Sec. 2.3, Sec. 7.1], [152]), slightly different interpretations in terms of the derivation can be found in the literature. The following considerations reflect the author's interpretation, which is mainly based on the derivations in Refs. [96, Sec. 4.1] and [136, Sec. 7.1] as well as ideas from statistical mechanics [137], in particular the kinetic theory of gases [19].

Consider a population of a large number of particles N_p, where the state of the ith particle at any time t is uniquely defined by its point in physical space and phase space[1] $\boldsymbol{X}_i(t) \in \mathbb{R}^3$ and $\boldsymbol{\Xi}_i(t) \in \Omega$, respectively. Then, if its microscopic behavior is probabilistic, i.e. governed by a stochastic differential equation (SDE), the state at time t is given by the one-particle PDF $p_i^{(1)}(\boldsymbol{\xi}_i, \boldsymbol{x}_i; t)$ defined such that

$$\Pr\left\{\boldsymbol{\Xi}_i \in \left(\boldsymbol{\xi}_i, \boldsymbol{\xi}_i + \mathrm{d}\boldsymbol{\xi}_i\right) \cap \boldsymbol{X}_i \in (\boldsymbol{x}_i, \boldsymbol{x}_i + \mathrm{d}\boldsymbol{x}_i)\right\} = p_i^{(1)}(\boldsymbol{\xi}_i, \boldsymbol{x}_i; t)\, \mathrm{d}\boldsymbol{\xi}_i\, \mathrm{d}\boldsymbol{x}_i. \quad (2.2)$$

In fact, even if its microscopic behavior is deterministic, virtually any particulate system that is not purely hypothetical can be considered probabilistic because the initial state is never known exactly. As the state of a single particle depends on the states of all other particles, the complete N_p-particle system is described by a joint PDF of $N_p(N+3)$ variables, say $p^{(N_p)}(\boldsymbol{\xi}_1, \boldsymbol{x}_1, \boldsymbol{\xi}_2, \boldsymbol{x}_2, \ldots, \boldsymbol{\xi}_{N_p}, \boldsymbol{x}_{N_p}; t)$, with the marginal PDFs

$$\begin{aligned}
p_1^{(1)}(\boldsymbol{\xi}_1, \boldsymbol{x}_1; t) &= \int_{\mathbb{R}^3} \cdots \int_{\Omega} p^{(N_p)}\, \mathrm{d}\boldsymbol{\xi}_2\, \mathrm{d}\boldsymbol{x}_2\, \mathrm{d}\boldsymbol{\xi}_3\, \mathrm{d}\boldsymbol{x}_3 \cdots \mathrm{d}\boldsymbol{\xi}_{N_p}\, \mathrm{d}\boldsymbol{x}_{N_p}, \\
p_2^{(1)}(\boldsymbol{\xi}_2, \boldsymbol{x}_2; t) &= \int_{\mathbb{R}^3} \cdots \int_{\Omega} p^{(N_p)}\, \mathrm{d}\boldsymbol{\xi}_1\, \mathrm{d}\boldsymbol{x}_1\, \mathrm{d}\boldsymbol{\xi}_3\, \mathrm{d}\boldsymbol{x}_3 \cdots \mathrm{d}\boldsymbol{\xi}_{N_p}\, \mathrm{d}\boldsymbol{x}_{N_p}, \\
&\vdots \\
p_{N_p}^{(1)}(\boldsymbol{\xi}_{N_p}, \boldsymbol{x}_{N_p}; t) &= \int_{\mathbb{R}^3} \cdots \int_{\Omega} p^{(N_p)}\, \mathrm{d}\boldsymbol{\xi}_1\, \mathrm{d}\boldsymbol{x}_1\, \mathrm{d}\boldsymbol{\xi}_2\, \mathrm{d}\boldsymbol{x}_2 \cdots \mathrm{d}\boldsymbol{\xi}_{N_p-1}\, \mathrm{d}\boldsymbol{x}_{N_p-1}.
\end{aligned} \quad (2.3)$$

Given the individual random states of all particles, i.e. $\boldsymbol{\Xi}_i(t), \boldsymbol{X}_i(t)$ for $i = 1, 2, \ldots, N_p$, the corresponding state of the N_p-particle system is described by

$$F(\boldsymbol{\xi}, \boldsymbol{x}; t) = \sum_{i=1}^{N_p} \delta\left(\boldsymbol{\xi} - \boldsymbol{\Xi}_i(t)\right) \delta\left(\boldsymbol{x} - \boldsymbol{X}_i(t)\right), \quad (2.4)$$

[1] It is worth noting that, at this point, there is no need to distinguish between physical space and phase space, and the state of a particle could be given by one $(N+3)$-dimensional vector. The different variables are only used for consistency with the following sections.

where δ denotes the Dirac delta function. Evidently, F satisfies the desired property of the NDF f in (2.1) for some realization of the system. It can be thought of as the *actual* NDF, which corresponds to a collection of random variables and is, accordingly, itself a random quantity. As such, the function F is not suitable as a NDF for the mesoscopic description of the observed particulate system. Instead, the NDF should represent the *average* particle number density from an infinite number of realizations. In other words, the NDF is the *expectation* of F, i.e.

$$\begin{aligned} f(\boldsymbol{\xi}, \boldsymbol{x}; t) &= \langle F(\boldsymbol{\xi}, \boldsymbol{x}; t) \rangle \\ &= \sum_{i=1}^{N_p} \int_{\mathbb{R}^3} \cdots \int_{\Omega} p^{(N_p)}(\boldsymbol{\xi}_1, \boldsymbol{x}_1, \boldsymbol{\xi}_2, \boldsymbol{x}_2, \ldots, \boldsymbol{\xi}_{N_p}, \boldsymbol{x}_{N_p}; t) \\ &\qquad \cdot \delta\left(\boldsymbol{\xi} - \boldsymbol{\xi}_i\right) \delta\left(\boldsymbol{x} - \boldsymbol{x}_i\right) \mathrm{d}\boldsymbol{\xi}_1 \, \mathrm{d}\boldsymbol{x}_1 \, \mathrm{d}\boldsymbol{\xi}_2 \, \mathrm{d}\boldsymbol{x}_2 \cdots \mathrm{d}\boldsymbol{\xi}_{N_p} \, \mathrm{d}\boldsymbol{x}_{N_p}. \end{aligned} \tag{2.5}$$

Taking into account the marginal densities in (2.3), the ith term of the sum in (2.5) reads

$$\int_{\mathbb{R}^3} \int_{\Omega} p_i^{(1)}(\boldsymbol{\xi}_i, \boldsymbol{x}_i; t) \delta\left(\boldsymbol{\xi} - \boldsymbol{\xi}_i\right) \delta\left(\boldsymbol{x} - \boldsymbol{x}_i\right) \mathrm{d}\boldsymbol{\xi}_i \, \mathrm{d}\boldsymbol{x}_i, \tag{2.6}$$

and thus, the NDF can finally be expressed as

$$f(\boldsymbol{\xi}, \boldsymbol{x}; t) = \sum_{i=1}^{N_p} p_i^{(1)}(\boldsymbol{\xi}, \boldsymbol{x}; t). \tag{2.7}$$

In the special case of identical one-particle distributions, this can be simplified to

$$f(\boldsymbol{\xi}, \boldsymbol{x}; t) = N_p p_1^{(1)}(\boldsymbol{\xi}, \boldsymbol{x}; t), \tag{2.8}$$

which highlights the fact that the only mathematical difference between a NDF and a PDF is the normalization, i.e.

$$\int_{\mathbb{R}^3} \int_{\Omega} f(\boldsymbol{\xi}, \boldsymbol{x}; t) \, \mathrm{d}\boldsymbol{\xi} \, \mathrm{d}\boldsymbol{x} = N_p(t). \tag{2.9}$$

The NDF provides a complete mesoscopic description of a particulate system. Its evolution is governed by a PDE, the so-called PBE, which is detailed in the next section.

2.1.2. The Population Balance Equation

The PBE is, in its most general form, a partial integro-differential equation that can be viewed as a continuity statement for the NDF. The contents of this section are limited to the final differential form of the PBE, which is the result of more rigorous derivations found elsewhere, e.g. [136, Ch. 2] and [96, Sec. 2.2].

General form

The PBE in general differential form, i.e. for arbitrary control volumes in three-dimensional physical and N-dimensional phase space, reads

$$\begin{aligned}\frac{\partial f(\boldsymbol{\xi},\boldsymbol{x};t)}{\partial t} = &\underbrace{-\frac{\partial}{\partial x_i}\left[v_i(\boldsymbol{\xi},\boldsymbol{x})f(\boldsymbol{\xi},\boldsymbol{x};t)\right]}_{\text{(i) physical advection}} + \underbrace{\frac{\partial^2}{\partial x_i \partial x_j}\left[c_{ij}(\boldsymbol{\xi},\boldsymbol{x})f(\boldsymbol{\xi},\boldsymbol{x};t)\right]}_{\text{(ii) physical diffusion}} \\ &\underbrace{-\frac{\partial}{\partial \xi_k}\left[a_k(\boldsymbol{\xi},\boldsymbol{x})f(\boldsymbol{\xi},\boldsymbol{x};t)\right]}_{\text{(iii) phase-space advection}} + \underbrace{\frac{\partial^2}{\partial \xi_k \partial \xi_l}\left[d_{kl}(\boldsymbol{\xi},\boldsymbol{x})f(\boldsymbol{\xi},\boldsymbol{x};t)\right]}_{\text{(iv) phase-space diffusion}} \\ &+ \underbrace{\mathcal{S}(f,\boldsymbol{\xi},\boldsymbol{x})}_{\text{(v) source term}},\end{aligned} \tag{2.10}$$

where $(v_i) = \boldsymbol{v} \in \mathbb{R}^3$ is the physical advection velocity, $(c_{ij}) = \mathbf{C} \in \mathbb{R}^{3\times3}$ the physical diffusivity, $(a_k) = \boldsymbol{a} \in \mathbb{R}^N$ the advection "velocity" in phase space, $(d_{kl}) = \mathbf{D} \in \mathbb{R}^{N\times N}$ the phase-space diffusion coefficient matrix, and $\mathcal{S}$ represents sources or sinks. Details on the physical meaning and specifics of each of the terms in the PBE are discussed below.

(i) *Physical advection*: The advective transport in physical space requires particular attention with respect to the advection velocity $\boldsymbol{v}$. In the context of multiphase flows, where the particulate phase is dispersed in a fluid, two cases are distinguished in the literature: In the first case, the particles instantaneously adapt to the fluid velocity field, and $\boldsymbol{v}$ equals the local fluid velocity at all times. In the second case, particles are transported in physical space with an individual velocity, which then appears as an internal coordinate in $\boldsymbol{\xi}$, and the transport equation of the NDF is commonly referred to as the generalized PBE (GPBE) [46, 96, 97]. Whether

$\boldsymbol{v}$ should be a phase space variable depends on how fast dispersed entities adapt to the fluid velocity field. This is indicated by the Stokes number St, which relates the characteristic time of a particle to the characteristic time of the fluid flow. If $\mathrm{St} \ll 1$, the particles follow the local fluid velocity, whereas higher Stokes numbers indicate larger particle inertia and consequently a velocity difference between fluid and particles [97]. In spatially inhomogeneous systems, the classification of the mesoscopic description as PBE or GPBE is essential for the appropriate selection of models.

(ii) *Physical diffusion*: A diffusive flux in physical space must be taken into account if the observed system involves very fine particles[2] that are significantly affected by Brownian motion, or if particles are assumed to follow the flow of a carrier fluid and turbulence is modeled by a turbulent diffusion term (see Section 2.3). If particle velocity is an internal coordinate, such effects are captured by the phase-space diffusion term (as detailed in Chapter 5), and the diffusion in physical space vanishes.

(iii) *Phase-space advection*: The advection in phase space represents all processes that imply continuous changes in internal coordinate values with the rate of change (advection velocity) $\boldsymbol{a}$. Physical examples of advection in phase space are the evaporation of liquid drops if $\boldsymbol{\xi}$ includes a measure of size, or acceleration if the particle velocity is an internal coordinate.

(iv) *Phase-space diffusion*: The diffusion in phase space represents changes in internal-coordinate space due to phenomena that are considered random at the microscale, e.g. turbulent effects as detailed in Chapter 5.

(v) *Source term*: The effects of all discrete events are represented by the source term $\mathcal{S}$. Such events are e.g. the breakup, collision and aggregation of particles. $\mathcal{S}$ is a functional that typically involves some integral expression with respect to $\boldsymbol{\xi}$. Thus, the PBE is, in general, a partial integro-differential equation. The source term shall remain abstract at this point. An expression of $\mathcal{S}$ for particle fragmentation will be given in Chapter 4, and hard-sphere collisions will be briefly addressed in Chapter 6.

[2] Marchisio and Fox [96] give an estimate of less than one micron in size.

Spatially homogeneous form

Generally, when solving (2.10) numerically, the terms can be treated separately with respect to discretizing the differential operators. The discretization in physical space is usually achieved by well-known methods for the numerical solution of convection-diffusion equations, such as the finite difference method [40, Ch. 3], the finite element method [88], or the finite volume method [87]. For the development of numerical methods that are not particularly concerned with the transport in physical space, it is thus sensible to reduce the PBE to the spatially homogeneous form. Then, dropping all physical-space dependencies, the PBE simplifies to

$$\begin{aligned}\frac{\partial f(\boldsymbol{\xi},t)}{\partial t} = &-\frac{\partial}{\partial \xi_i}\left[a_i(\boldsymbol{\xi})f(\boldsymbol{\xi},t)\right] + \frac{\partial^2}{\partial \xi_i \partial \xi_j}\left[d_{ij}(\boldsymbol{\xi})f(\boldsymbol{\xi},t)\right] \\ &+ \mathcal{S}(f,\boldsymbol{\xi}).\end{aligned} \tag{2.11}$$

Univariate form

To thoroughly investigate the behavior of new numerical methods with respect to analytical reference solutions, which only exist for simplified forms, it is often convenient or even necessary to reduce (2.11) further to the univariate form, i.e. a NDF of only a single variable in phase space. The PBE then reads

$$\frac{\partial f(\xi,t)}{\partial t} = -\frac{\partial}{\partial \xi}\left[a(\xi)f(\xi,t)\right] + \frac{\partial^2}{\partial \xi^2}\left[d(\xi)f(\xi,t)\right] + \mathcal{S}(f,\xi), \tag{2.12}$$

which is the form of PBE that most of the research reported in this thesis is based on.

2.2. Moment Transport Equations

In many cases, obtaining detailed information on the NDF is not the primary goal of numerical simulations. Instead, the desired results are local macroscopic quantities, such as the total number concentration, mass, momentum or kinetic energy. These can be expressed in terms of the raw[3] moments associated with

[3] Here, the term *raw moment* refers to a moment about the origin, as opposed to e.g. a central moment, which refers to a moment about the mean.

the NDF, which are, in the general case of N-dimensional phase space, defined as

$$m_{k_1,k_2,\ldots,k_N} = \langle \xi_1^{k_1} \xi_2^{k_2} \cdots \xi_N^{k_N} \rangle = \int_\Omega \xi_1^{k_1} \xi_2^{k_2} \cdots \xi_N^{k_N} f(\boldsymbol{\xi}) \, \mathrm{d}\boldsymbol{\xi}. \tag{2.13}$$

For example, consider $N = 4$ internal coordinates. Then, if ξ_1 represents the particle diameter, $(\xi_2, \xi_3, \xi_4)^{\mathrm{T}}$ the velocity components in three physical dimensions and the particle density (specific mass), say ρ_p, is constant, one can obtain various macroscopic quantities from the moments, e.g.

$$\text{total momentum in } x_1\text{-direction} = C \, m_{3,1,0,0}, \tag{2.14}$$

$$\text{total kinetic energy} = \tfrac{1}{2} C \left(m_{3,2,0,0} + m_{3,0,2,0} + m_{3,0,0,2} \right), \tag{2.15}$$

where $C = \pi \rho_p / 6$. More detailed examples of how moments are related to physical properties can be found in [46, 96].

It is evident from the moment definition (2.13) that transport equations for the moments are simply obtained by multiplication of the underlying PBE by $\xi_1^{k_1} \xi_2^{k_2} \cdots \xi_N^{k_N}$ and subsequent integration over Ω. Thus, assuming the advection velocity to equal that of the carrier fluid $\boldsymbol{u}$, and omitting time and physical-space dependencies for brevity, the $(k_1, k_2, \ldots, k_N)$th moment transport equation for an inhomogeneous system derived from (2.10) reads

$$\begin{aligned} \frac{\partial m_{k_1,k_2,\ldots,k_N}}{\partial t} = &- \frac{\partial}{\partial x_i} \left(u_i m_{k_1,k_2,\ldots,k_N} \right) + \frac{\partial^2}{\partial x_i \partial x_j} \left(c_{ij} m_{k_1,k_2,\ldots,k_N} \right) \\ &+ \dot{m}_{k_1,k_2,\ldots,k_N}, \end{aligned} \tag{2.16}$$

where the moment source term $\dot{m}_{k_1,k_2,\ldots,k_N}$ represents the moment transforms of all except for the physical transport terms, i.e. those of the terms (iii)–(v) in (2.10). For multivariate inhomogeneous systems, the moment source term is, due to lack of relevance, not detailed further at this point. However, it is important to note that $\dot{m}_{k_1,k_2,\ldots,k_N}$ is unclosed, as will be highlighted by the univariate form below. Moreover, a specific form considering phase-space advection and diffusion in the spatially homogeneous multivariate moment equation will be discussed in Section 5.1.3.

The moment transformation reduces the dimensionality, and hence the computational complexity, by transferring the problem from the mesoscale to the

macroscale. More precisely, considering a spatially inhomogeneous system, the problem of solving a PBE in $N + 4$ dimensions[4] is reduced to the problem of solving a system of moment equations in four dimensions.

Considering only a single internal coordinate and assuming the absence of fluxes across phase-space boundaries, the univariate moment definition

$$m_k = \langle \xi^k \rangle = \int_\Omega \xi^k f(\xi) \, \mathrm{d}\xi \tag{2.17}$$

can be used to transform the univariate PBE (2.12) and obtain, after repeated integration by parts, the kth moment transport equation

$$\begin{aligned} \frac{\mathrm{d}m_k(t)}{\mathrm{d}t} \;=\; & k \int_\Omega \xi^{k-1} a(\xi) f(\xi, t) \, \mathrm{d}\xi \\ & + \; k(k-1) \int_\Omega \xi^{k-2} d(\xi) f(\xi, t) \, \mathrm{d}\xi \;+\; \int_\Omega \xi^k \mathcal{S}(f, \xi) \, \mathrm{d}\xi. \end{aligned} \tag{2.18}$$

In the presence of fluxes across phase-space boundaries, e.g. as a result of the disappearance of droplets by complete evaporation, the integration by parts results in additional terms of the form $g(\xi) f(\xi, t)\big|_{\xi=\xi_{\min}}^{\xi_{\max}}$, where g is an arbitrary function continuous on $[\xi_{\min}, \xi_{\max}]$. However, problems of this kind will not be dealt with in this dissertation.

Evidently, the NDF still appears in both integral terms on the RHS of (2.18), i.e. the moment equations in this form are unclosed. Various methods to close moment equations derived from PBEs have been proposed in the past, including the method of moments with interpolative closure (MOMIC) [51], numerous methods for the reconstruction of a NDF with more or less restrictive assumptions regarding its shape [8, 16, 37, 80, 142, 165], entropy maximization [106, 108], the finite-size domain complete set of trial functions method of moments (FCMOM) [154–156], and the family of QBMMs, which will be detailed in Chapter 3.

[4] Considering time, three physical and N phase-space dimensions, yields a total of $N + 4$ dimensions.

2.3. Description of a Turbulent Carrier Fluid

Besides the above-described equations for the particulate system, a complete model for dispersed multiphase flows requires the description of the continuous fluid phase, which is almost always turbulent, and the interaction with dispersed particles in terms of the exchange of momentum and possibly mass and energy. The most common approach is the macroscopic description of the carrier fluid by the well-known Navier-Stokes equations that govern the evolution of the fluid velocity field $\boldsymbol{u} = (u_1, u_2, u_3)^T$ and the pressure field p. Assuming an incompressible Newtonian fluid for the sake of simplicity as well as the absence of mass transfer, they can be expressed in terms of the conservation of mass (continuity equation)

$$\frac{\partial u_i}{\partial x_i} = 0 \tag{2.19}$$

and the conservation of linear momentum

$$\frac{\partial u_i}{\partial t} + u_j \frac{\partial u_i}{\partial x_j} = -\frac{1}{\rho_f} \frac{\partial p}{\partial x_i} + \nu_f \frac{\partial}{\partial x_j} \left(\frac{\partial u_i}{\partial x_j} + \frac{\partial u_j}{\partial x_i} \right) + \dot{u}_i, \tag{2.20}$$

where ρ_f is the fluid density, ν_f the kinematic viscosity and $\dot{u}_i$ is the acceleration in x_i-direction by virtue of an external force, which may be due to the interaction with particles in dispersed multiphase flows. The features of the Navier-Stokes equations and suitable methods to solve them numerically have been extensively dealt with in many textbooks, e.g. [7, 164], and will not be detailed further. Instead, this section is intended to briefly review the most common types of turbulence models used in conjunction with the Navier-Stokes equations in order to identify the information available to model turbulent effects on the dispersed phase.

It is common knowledge among researchers in fluid mechanics that the evolution of a dynamic fluid flow system in terms of its macroscopic quantities is governed by the Navier-Stokes equations, regardless of whether the flow is laminar or turbulent. Nevertheless, in the field of computational fluid dynamics, turbulence is arguably one of the most important and also one of the most challenging aspects of numerical models. This is due to the fact that energy is transferred across a wide range of length scales from large eddies containing

most of the total energy to eddies of the smallest scale (Kolmogorov scale η), a mechanism commonly referred to as the turbulent energy cascade [134]. Thus, in order to solve the Navier-Stokes equations numerically, capturing the entire energy spectrum from the energy-containing range to the dissipation range is essential. In other words, all length scales from the integral scale, say l_0, down to the Kolmogorov scale η must be resolved on the discretized spatial domain.

It is well known from Kolmogorov theory that the range of relevant length scales depends on the level of turbulence indicated by the Reynolds number

$$\mathrm{Re} = \frac{|\boldsymbol{u}|\, l}{\nu_f}, \tag{2.21}$$

where l is a characteristic length scale of the fluid flow. Then the range of length scales that must be resolved to capture the entire energy spectrum grows as

$$\frac{l_0}{\eta} \propto \mathrm{Re}^{3/4}. \tag{2.22}$$

Despite what this sublinear growth may suggest, it corresponds to a rapid increase in computational complexity with $O(\mathrm{Re}^{9/4})$ in the general case of three spatial dimensions. Naturally, this required fine resolution in space entails the necessity to adjust the temporal discretization accordingly. For this reason, the direct numerical simulation (DNS) of the governing Navier-Stokes equations is limited to relatively low Reynolds numbers. The majority of flows occurring in nature and technology, though, do not belong in that category and require turbulence modeling. Two major classes of turbulence models are commonly used with the Navier-Stokes equations, namely Reynolds-averaged Navier-Stokes (RANS) models and large eddy simulation (LES). The difference between DNS, LES and RANS in terms of the computed velocity field is schematically illustrated in Figure 2.1.

The underlying idea of RANS models is the decomposition of the real instantaneous fluid velocity

$$\boldsymbol{u} = \bar{\boldsymbol{u}} + \boldsymbol{u'}, \tag{2.23}$$

where $\bar{\boldsymbol{u}}$ is the mean velocity obtained by a suitable averaging method and $\boldsymbol{u'}$ represents the velocity fluctuation due to turbulence. This decomposition yields

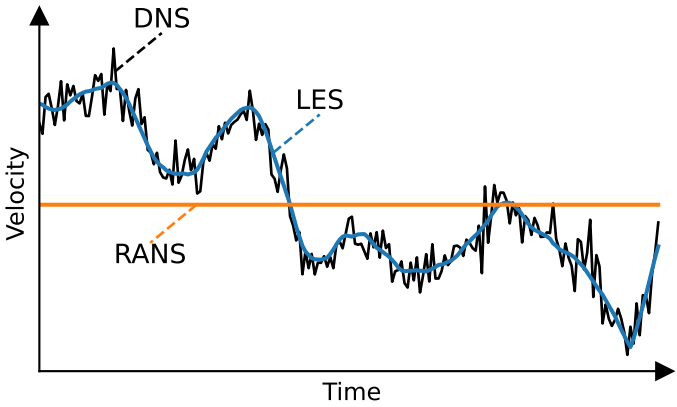

Figure 2.1.: Schematic illustration of the local velocity in a turbulent flow computed with DNS, LES and RANS. The DNS resolves all scales of turbulence and, as a result, captures all velocity fluctuations. LES captures only the fluctuations due to the large turbulent structures that contain the bulk of the kinetic energy, while the effect of the small-scale fluctuations is modeled. RANS does not capture any velocity fluctuations due to averaging.

the RANS equations. As a consequence, an unclosed term appears in the momentum equation, which is commonly referred to as Reynolds stress tensor. The various types of RANS models are concerned with modeling of the unclosed term. The most popular RANS model is the k-ϵ model that involves additional transport equations for the turbulent kinetic energy k_t and the turbulent energy dissipation rate ϵ_t. Then, with an eddy viscosity based on Boussinesq's hypothesis

$$\nu_t \propto \frac{k_t^2}{\epsilon_t}, \tag{2.24}$$

the RANS equations are closed using an effective viscosity

$$\nu_e = \nu_f + \nu_t \tag{2.25}$$

instead of ν_f. Moreover, with k_t and ϵ_t known, a characteristic turbulence

length scale can be estimated by [171]

$$l_t \propto \frac{k_t^{3/2}}{\epsilon_t}. \tag{2.26}$$

LES models are also based on a decomposition like (2.23), though the underlying approach is fundamentally different. Contrary to RANS models, the decomposition is obtained by filtering instead of averaging. In simplified terms (see e.g. [144] for detailed explanations), scales are separated by means of some spatial filtering operation that passes only lengths larger than a specified cutoff length, often denoted by Δ, which is typically chosen such that the length scales containing the bulk of the kinetic energy are passed by the filter. Using the same notation as in (2.23), $\overline{\boldsymbol{u}}$ then represents the filtered or resolved velocity and $\boldsymbol{u}'$ the subgrid-scale (SGS) velocity fluctuations. The resulting filtered Navier-Stokes equations are solved on a spatial grid that is sufficiently fine to resolve all scales larger than Δ. However, the governing equations contain unclosed terms for SGS turbulence, namely the SGS stress tensor, that must be modeled. For that purpose, a large variety of models exist, see [144] for an overview. The LES-counterparts of the quantities in (2.24) and (2.26) can then be deduced from the filtered quantities or from the modeled SGS stress tensor. For example, the characteristic turbulent length scale is given in terms of the cutoff length, i.e. $l_t = \Delta$, and the SGS kinetic energy and dissipation rate are related to the SGS stress tensor and strain rate, an indirect result of filtered quantities.

In summary, the numerical simulation of most flows, whether single-phase or multiphase flows, requires a turbulence model of some kind. The most common types of turbulence models used with the Navier-Stokes equations are based on the RANS equations or LES. While the physical interpretation is fundamentally different, both are similar in that they are based on the decomposition of the velocity field into a resolved and a modeled contribution resulting in an unclosed stress tensor in the momentum equation, and that characteristic quantities of the modeled scales of turbulence, i.e. a characteristic turbulence length scale l_t, the turbulent kinetic energy k_t, and the turbulent energy dissipation rate ϵ_t, are either obtained directly from the model equations or can be deduced from basic relationships known from Kolmogorov theory or Boussinesq's hypothesis. Thus, it is henceforward assumed that this information is available for modeling the dispersed phase.

3. Quadrature-Based Closure of Moment Equations

This chapter is concerned with the underlying theory and the different types of quadrature-based moment methods (QBMMs) for the closure of moment transport equations derived from PBEs. Like the contributions in Chapters 4–6, the contents of this chapter are limited to spatially homogeneous systems. While this may appear as a major limitation given the complexity of real physical systems, it is a reasonable simplification when transport in physical space is not the topic of research, since the discretization of the physical flux terms for the numerical solution can be chosen independently of the method to close the moment source terms. However, it should be noted that discretizing the physical advection and diffusion terms in moment equations is particularly challenging, due to the problem of moment realizability, and requires special techniques, which have been the subject of numerous studies, e.g. [23, 147, 166, 167].

The chapter is structured as follows: First, as the mathematical foundation of QBMMs, the most important aspects of orthogonal polynomials and Gaussian quadrature formulas will be briefly reviewed in Sections 3.1 and 3.2. Then, in Section 3.3, the problem of moment realizability will be explained, before describing important moment inversion algorithms, i.e. algorithms to compute Gaussian quadrature rules from moments, in Section 3.4. Finally, some specific QBMMs will be detailed in Section 3.5 with a focus on univariate QBMMs, as all numerical investigations in this thesis are limited to univariate problems. However, multivariate QBMMs are also briefly addressed in Section 3.5.3 due to their relevance for real physical problems. This includes the main difficulties associated with multivariate QBMMs as well as the importance of univariate QBMMs for multivariate problems, which serves as motivation for the reduction of the general PBE to the univariate form.

3.1. Orthogonal Polynomials

3.1.1. Definition

Let $\mathbb{B}$ be a subset of $\mathbb{R}$, and let $w : \mathbb{B} \to \mathbb{R}_{\geq 0}$ be an integrable non-negative function, referred to as weight function, with finite moments of all orders, i.e.

$$\left| \int_{\mathbb{B}} z^k w(z) \, \mathrm{d}z \right| < \infty, \quad k = 0, 1, 2, \ldots \tag{3.1}$$

Furthermore, let the weighted inner product of two functions continuous on $\mathbb{B}$, say g and h, with respect to w be denoted by

$$\big(g, h\big)_w \coloneqq \int_{\mathbb{B}} g(z) h(z) w(z) \, \mathrm{d}z. \tag{3.2}$$

Then the set $\{p_0, p_1, p_2, \ldots\}$, where p_k is a polynomial of true degree k, is said to be orthogonal with respect to w if and only if

$$\big(p_j, p_k\big)_w = 0 \quad \text{iff } j \neq k. \tag{3.3}$$

The kth-degree *monic* orthogonal polynomial will hereinafter be denoted by π_k. The corresponding *orthonormal* polynomial $\tilde{\pi}_k$ is normalized such that $\|\tilde{\pi}_k\|_w = 1$, where $\|\cdot\|_w$ is the norm defined by

$$\big\|g\big\|_w \coloneqq \sqrt{\big(g, g\big)_w}. \tag{3.4}$$

Accordingly, the two mentioned representations of an orthogonal polynomial system satisfy

$$\pi_k = \|\pi_k\|_w \, \tilde{\pi}_k. \tag{3.5}$$

3.1.2. Properties

This section constitutes a brief review of well-known properties of orthogonal polynomials, limited to those relevant for QBMMs. Proofs of the relationships presented below as well as further interesting properties can be found in most textbooks on orthogonal polynomials, e.g. [54, Sec. 1.2] or [22, Ch. I, Sec. 2 & 3].

Three-term recurrence relation

With the definition

$$\pi_{-1} \coloneqq 0, \tag{3.6}$$

any set of monic orthogonal polynomials $\{\pi_0, \pi_1, \pi_2, \dots\}$ satisfies the three-term recurrence relation

$$\pi_{k+1}(z) = (z - \alpha_k)\,\pi_k(z) - \beta_k \pi_{k-1}(z), \quad k = 0, 1, 2, \dots, \tag{3.7}$$

where the recurrence coefficients are

$$\alpha_k = \frac{(z\pi_k, \pi_k)_w}{(\pi_k, \pi_k)_w}, \qquad k = 0, 1, 2, \dots, \tag{3.8}$$

$$\beta_k = \frac{(\pi_k, \pi_k)_w}{(\pi_{k-1}, \pi_{k-1})_w}, \quad k = 1, 2, \dots \tag{3.9}$$

and, by convention (see e.g. [54, Sec. 1.3.1]),

$$\beta_0 \coloneqq (\pi_0, \pi_0)_w\,. \tag{3.10}$$

Often it is more convenient to use the orthonormal form. Then the three-term recurrence relation reads[1]

$$\sqrt{\beta_{k+1}}\tilde{\pi}_{k+1}(z) = (z - \alpha_k)\,\tilde{\pi}_k(z) - \sqrt{\beta_k}\tilde{\pi}_{k-1}(z), \quad k = 0, 1, 2, \dots \tag{3.11}$$

which can be written for $k = 0, 1, \dots, n-1$ in matrix form as

$$\sqrt{\beta_n}\begin{pmatrix} 0 \\ 0 \\ \vdots \\ 0 \\ \tilde{\pi}_n \end{pmatrix} = z\underbrace{\begin{pmatrix} \tilde{\pi}_0 \\ \tilde{\pi}_1 \\ \vdots \\ \tilde{\pi}_{n-2} \\ \tilde{\pi}_{n-1} \end{pmatrix}}_{\tilde{\boldsymbol{\pi}}_{n-1}} - \underbrace{\begin{pmatrix} \alpha_0 & \sqrt{\beta_1} & & & \\ \sqrt{\beta_1} & \alpha_1 & \sqrt{\beta_2} & & \\ & \sqrt{\beta_2} & \ddots & \ddots & \\ & & \ddots & \alpha_{n-2} & \sqrt{\beta_{n-1}} \\ & & & \sqrt{\beta_{n-1}} & \alpha_{n-1} \end{pmatrix}}_{\mathbf{J}_n} \underbrace{\begin{pmatrix} \tilde{\pi}_0 \\ \tilde{\pi}_1 \\ \vdots \\ \tilde{\pi}_{n-2} \\ \tilde{\pi}_{n-1} \end{pmatrix}}_{\tilde{\boldsymbol{\pi}}_{n-1}}, \tag{3.12}$$

where $\mathbf{J}_n$ is called the truncated Jacobi matrix of size n.

[1] Inserting (3.5) into (3.7), dividing by $\|\pi_{k+1}\|_w$ and substituting the norm expressions with $\sqrt{\beta_{k+1}} = \|\pi_{k+1}\|_w / \|\pi_k\|_w$ and $\sqrt{\beta_{k+1}\beta_k} = \|\pi_{k+1}\|_w / \|\pi_{k-1}\|_w$ (following from (3.9)) yields the given three-term recurrence relation.

Zeros

The zeros of orthogonal polynomials are all

- real,
- simple,
- located in the interior of the support interval of w.

Moreover, denoting the zeros of the nth degree orthogonal polynomial by $z_{i,n}$, using the convention that

$$z_{i,n} < z_{i+1,n}, \quad i = 1, 2, \ldots, n-1, \tag{3.13}$$

the LHS of (3.12) vanishes for $z = z_{i,n}\ \forall i = 1, \ldots, n$, and the three-term recurrence relation can be written as

$$\mathbf{J}_n\ \tilde{\boldsymbol{\pi}}_{n-1}(z_{i,n}) \ = \ z_{i,n}\ \tilde{\boldsymbol{\pi}}_{n-1}(z_{i,n}). \tag{3.14}$$

In other words, the zeros of the nth-degree orthogonal polynomial are the eigenvalues of the truncated Jacobi matrix $\mathbf{J}_n$.

3.2. Gaussian Quadrature Formulas

This section serves as a brief review of the fundamentals and most important properties of Gaussian quadrature formulas, an essential component of QBMMs. Proofs of the well-known relationships presented below as well as additional details and discussions of numerical aspects can be found in common textbooks on numerical integration and orthogonal polynomials, e.g. [22, 28, 54].

Consider the functional

$$I(g) \coloneqq \int_{\mathbb{B}} g(z) w(z)\, \mathrm{d}z, \tag{3.15}$$

where $g : \mathbb{B} \to \mathbb{R}$ is an arbitrary function and w a weight function as defined in Section 3.1.1. Then an n-point quadrature rule G_n satisfies

$$I(g) = \underbrace{\sum_{j=1}^{n} w_j g(z_j)}_{=:\, G_n(g)} + R_n(g), \tag{3.16}$$

where z_j denotes the jth quadrature node (abscissa), w_j the corresponding weight, and R_n the approximation error associated with G_n. An n-node quadrature is called Gaussian or Gauss quadrature if and only if its degree of accuracy is $2n-1$, i.e.

$$R_n(g) = 0 \quad \forall\, g \in \mathcal{P}_{2n-1}, \tag{3.17}$$

where $\mathcal{P}_{2n-1}$ is the set of all real polynomials with degree up to $2n-1$. This is known to be true if the quadrature nodes z_j are the zeros of π_n, the nth-degree orthogonal polynomial with respect to w. Moreover, it can be deduced from the Christoffel-Darboux theorem that the weights satisfy [172, Sec. 2.9]

$$\frac{1}{w_j} = \sum_{i=0}^{n-1} \left[\tilde{\pi}_i(z_j)\right]^2, \quad j = 1, 2, \ldots, n. \tag{3.18}$$

Taking into account that the normalization of $\tilde{\pi}_0$ requires[2] $\sqrt{\beta_0}\tilde{\pi}_0 = 1$, (3.18) is equivalent to

$$w_j = \beta_0 \underbrace{\left(\frac{\tilde{\pi}_0(z_j)}{\left\|\tilde{\boldsymbol{\pi}}_{n-1}(z_j)\right\|}\right)^2}_{\varphi_j^2}. \tag{3.19}$$

Finally, considering (3.14), it becomes obvious that φ_j is the first component of the normalized eigenvector belonging to the jth eigenvalue of $\mathbf{J}_n$, which is also the jth quadrature node. Thus, the abscissas and weights of the n-point Gaussian quadrature rule associated with the weight function w result from the eigenvalues and eigenvectors of the truncated Jacobi matrix $\mathbf{J}_n$. Furthermore, it follows from the definition of the recurrence coefficients in (3.8) and (3.9) that α_k and β_k are quotients of linear combinations of the ordinary moments up to $(2k+1)$th order. Accordingly, the first n recurrence coefficients, i.e. those with indices up to $k = n-1$, are determined by all moments up to order $2n-1$ (see also Section 3.4). In other words, an n-node Gaussian quadrature can be computed from the first $2n$ moments.

[2] Here, it should be noted that the definitions (3.2) and (3.10) as well as the moment definition in (2.17) imply the identity $\beta_0 = (\pi_0, \pi_0)_w = \|\pi_0\|_w^2 = m_0$.

3.3. The Problem of Moment Realizability

A critical aspect of moment methods that must be taken into account in the selection of numerical methods is the problem of moment realizability. Considering the moment definition in (2.17) and an unknown density (NDF) with support Ω, a set of moments is said to be realizable with respect to Ω if there exists at least one valid density function, i.e. a non-negative function with support Ω, that corresponds to the given moments. The question of whether a sequence of numbers is a valid moment sequence and whether the associated density function is uniquely determined by that moment sequence is commonly known as the moment problem. In the context of QBMMs, the latter is of secondary importance, whereas the former is essential since QBMMs usually fail with inconsistent moments. Based on the support Ω, the moment problem can be classified as [146]

- Hausdorff problem with bounded support $[0, 1]$,
- Stieltjes problem with semi-infinite support $[0, \infty)$,
- Hamburger problem with infinite support $(-\infty, +\infty)$.

The moment problem can also be formulated as follows: Let the vector of all moments[3] up to order p with respect to the support Ω be denoted by

$$\boldsymbol{m}_p = (m_0, m_1, \ldots, m_p)^{\mathrm{T}}. \tag{3.20}$$

Then $\boldsymbol{m}_p$ represents a valid (realizable) set of moments with respect to Ω if and only if $\boldsymbol{m}_p \in \mathcal{M}_p(\Omega)$, where $\mathcal{M}_p(\Omega)$ is the pth moment space, the convex p-dimensional space of all valid sequences of integer moments up to order p. In the special case $\boldsymbol{m}_p \in \partial\mathcal{M}_p(\Omega)$, where $\partial\mathcal{M}_p(\Omega)$ is the boundary of $\mathcal{M}_p(\Omega)$, the associated density function is unique [33]. In that case, the moment sequence can be characterized as "weakly realizable" [126]. An example of a function that

[3] It should be noted that, strictly speaking, the term "moments" to refer to a sequence of numbers that are not known to be realizable moments may be not entirely accurate since unrealizable moments are not moments at all.

generates moments on $\partial\mathcal{M}_{2n-1}(\Omega)$ is the N-point distribution density

$$f(\xi) = \sum_{i=1}^{N} c_i \delta(\xi - \xi_i), \quad N < n,\ c_i > 0,\ \xi_i \in \Omega. \tag{3.21}$$

Moment spaces and the problem of moment realizability are best illustrated by the example of the compact space of Hausdorff moments, as shown in Figure 3.1 for $\mathcal{M}_2([0,1])$.

In terms of realizability criteria, the Hamburger problem is the least restrictive. A necessary and sufficient condition for the moment sequence $\boldsymbol{m}_{2n-1}$ to be realizable is that the recurrence coefficients of the corresponding orthogonal

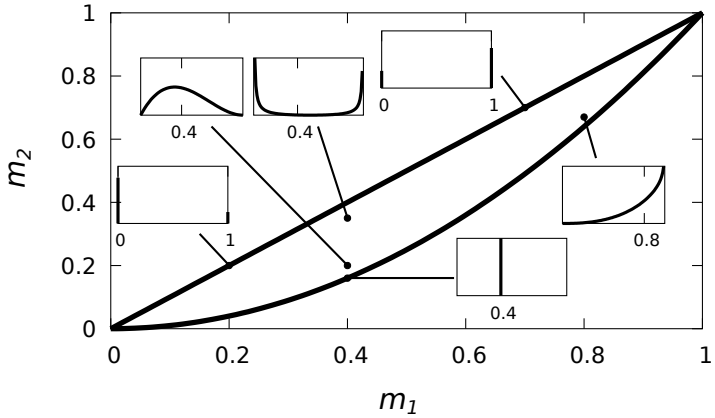

Figure 3.1.: Distributions on the moment space $\mathcal{M}_2$ related to the Hausdorff problem (slightly altered version of the illustration in [131], kindly provided by the author Martin Pollack). Assuming $m_0 = 1$, the space of valid moment sequences $\boldsymbol{m}_2$ is determined by the lower boundary $m_2 = m_1^2$ and the upper boundary $m_2 = m_1$. Point (discrete) distributions are located on $\partial\mathcal{M}_2$, whereas continuous distributions, here represented by beta distributions with different parameters, are in the interior of $\mathcal{M}_2$. The shown examples are only a few of an infinite number of possibilities.

polynomial system satisfy [22]

$$\alpha_k \in \mathbb{R} \quad \text{and} \quad \beta_k > 0 \quad \forall\, k = 0, 1, 2, \ldots, n-1. \tag{3.22}$$

An equivalent realizability condition is that the related Hankel moment matrix given by

$$\mathbf{M}_n = \begin{pmatrix} m_0 & m_1 & \ldots & m_{n-1} \\ m_1 & m_2 & \ldots & m_n \\ \vdots & \vdots & \ddots & \vdots \\ m_{n-1} & m_n & \ldots & m_{2n-2} \end{pmatrix} \tag{3.23}$$

is positive definite [54, Sec. 1.1]. On the other hand, $\boldsymbol{m}_{2n-1}$ is weakly realizable if $\beta_k = 0$ for any $k < n$. In that case, $\mathbf{M}_n$ is singular. In terms of realizability, the only moment sequences of interest for this work are Hamburger sequences. Therefore, the explicit specification of Ω will be omitted, hence

$$\mathcal{M}_p \coloneqq \mathcal{M}_p(\mathbb{R}). \tag{3.24}$$

Criteria for the remaining types of moment problems, which are not detailed here due to lack of relevance, can be found in the literature, e.g. [33] for Hausdorff problems and [54, 148] for Stieltjes problems.

The problem of moment realizability requires careful consideration with regard to the numerical methods used to solve moment transport equations in order to prevent corruption of the moment set. Even though there are correction algorithms for unrealizable moment sets, e.g. [173], it should be noted that they alter moments and additional measures must be taken to compensate the potential violation of physical conservation laws. Thus, it is preferable to employ techniques that are guaranteed to preserve moment realizability.

3.4. Moment Inversion Algorithms

As explained at the end of Section 3.2, the abscissas and weights of an n-node Gaussian quadrature result from the first $2n$ moments. The calculation of a quadrature rule from moments, a procedure commonly referred to as moment

inversion, is an essential component of QBMMs. While the resulting quadrature nodes and weights may differ from method to method, virtually every QBMM computes, at some point, a Gaussian quadrature from moments. Several algorithms are suitable for that purpose, such as the quotient-difference algorithm (QDA) [141] (see also [33, Sec. 1.5]), the product-difference algorithm (PDA) [59], the Golub-Welsch algorithm (GWA) [58], and different variants of the long quotient-modified difference algorithm (LQMDA) [54, 143, 170]. Both the QDA and the PDA are related to Stieltjes' work on continued fractions and their relationship to moments and orthogonal polynomials. They may be efficient in many practical cases but are generally considered to be less stable than the other mentioned algorithms [96, 170]. The PDA, for instance, is estimated to become unstable when $n \gtrsim 10$.[4] Moreover, both the QDA and PDA may fail for symmetric weight functions. For these reasons (especially the latter which would be an issue for the problems studied in Chapter 5), the PDA and QDA will hereinafter be disregarded, and only the LQMDA as well as the GWA are described below. As the method used to compute the quadrature nodes and weights from the Jacobi matrix can be chosen independently from available methods to solve the tridiagonal symmetric eigenvalue problem, the descriptions of the algorithms in this section are limited to the calculation of the elements of $\mathbf{J}_n$ from $\boldsymbol{m}_{2n-1}$.

3.4.1. The Long Quotient-Modified Difference Algorithm

The (LQMDA) [143] is, in general, suitable to compute the elements of $\mathbf{J}_n$ from a sequence of $2n$ modified moments

$$m'_k = \int_{\mathbb{B}} p_k(z) w(z) \, \mathrm{d}z, \quad k = 0, 1, \ldots, 2n-1, \tag{3.25}$$

where $\{p_0, p_1, \ldots, p_{2n-1}\}$ may be any set of polynomials satisfying a recurrence relation of the form

$$\gamma'_k p_{k+1}(z) = (z - \alpha'_k) p_k(z) - \beta'_k p_{k-1}(z) \tag{3.26}$$

[4] More precisely, Marchisio and Fox [96] state that the number of quadrature nodes resulting in numerical instabilities depends on the absolute values of the underlying moments and cannot be predicted a priori. However, they estimate a typical threshold at $n > 10$. This behavior is also indicated by the numerical study of John and Thein [76].

with known coefficients α'_k, β'_k and γ'_k. However, only the ordinary moments $\{m_k\}$ are of interest here. The following descriptions are thus limited to the special case of $p_k(z) = z^k$ with the coefficients

$$\alpha'_k = \beta'_k = 0, \quad \gamma'_k = 1, \quad k = 0, 1, 2, \ldots. \tag{3.27}$$

The variant of the LQMDA known as Wheeler algorithm [170] or modified Chebyshev algorithm [54, Sec. 2.1.7] is only slightly different from that proposed by Sack and Donovan [143] in terms of the choice of intermediate quantities. The algorithm presented below is in the form proposed by Wheeler [170] as described in Ref. [54, Sec. 2.1.7].

The calculation is based on the "mixed moments" s_{ij}. Given a set of ordinary moments as highlighted above, they are given by

$$s_{ij} = \int_{\mathbb{B}} \pi_i(z) z^j w(z) \, \mathrm{d}z. \tag{3.28}$$

First, the algorithm is initialized with[5]

$$\alpha_0 = \frac{m_1}{m_0}, \tag{3.29}$$

$$\beta_0 = m_0, \tag{3.30}$$

$$s_{-1,i} = 0, \quad i = 1, 2, \ldots, 2n-2, \tag{3.31}$$

$$s_{0,i} = m_i, \quad i = 0, 1, \ldots, 2n-1. \tag{3.32}$$

The recurrence coefficients with indices $i = 1, 2, \ldots, n-1$ can then be computed recursively:

$$s_{i,j} = s_{i-1,j+1} - \alpha_{i-1} s_{i-1,j} - \beta_{i-1} s_{i-2,j}, \quad j = i, \ldots, 2n-i-1 \tag{3.33}$$

$$\alpha_i = \frac{s_{i,i+1}}{s_{ii}} - \frac{s_{i-1,i}}{s_{i-1,i-1}} \tag{3.34}$$

$$\beta_i = \frac{s_{ii}}{s_{i-1,i-1}}. \tag{3.35}$$

[5] The initial values of α_0, β_0 and $s_{-1,i}$ follow directly from the relationships in (3.8), (3.10) and (3.6), respectively.

The LQMDA as proposed by Sack and Donovan [143] is obtained by replacing the intermediate quantities s_{ij} with $s'_{ij} = s_{ij}/s_{ii}$ and adjusting the calculation steps accordingly. As evident from (3.33), the computational complexity of the LQMDA is $O(n^2)$, cf. [54].

In the context of QBMMs, the LQMDA or Wheeler algorithm is a popular choice for the calculation of a quadrature rule from a sequence of moments, often in the form of an adaptive variant [178] that reduces the order of the approximation in case of almost-zero weights or strongly clustered abscissas for increased stability.

3.4.2. The Golub-Welsch Algorithm

The Golub-Welsch algorithm (GWA)[6] is based on the Cholesky decomposition of the Hankel moment matrix

$$\mathbf{M}_{n+1} = \mathbf{L}\mathbf{L}^T, \tag{3.36}$$

where $\mathbf{L} = \left(l_{ij}\right)$ is a lower triangular matrix[7]. The Cholesky decomposition exists for every symmetric positive-definite matrix [57], a condition that is known to be satisfied by $\mathbf{M}_{n+1}$ provided that the underlying moment sequence is realizable, as described in Section 3.3.

Letting $\mathbf{L}^{-1} = \left(l'_{ij}\right)$, the observation that the polynomials

$$p_j(z) = \sum_{k=0}^{n} l'_{j+1,k+1} z^k \quad j = 0, 1, \ldots, n \tag{3.37}$$

form an orthonormal system as well as the fact that $\mathbf{L}^{-1}$ can be expressed explicitly in terms of $\mathbf{L}$ result in the following algorithm for the calculation of the

[6] It should be noted that it is not entirely clear in the literature what parts of the algorithm proposed by Golub and Welsch [58] are referred to as GWA. Throughout this thesis, it will be used to refer only to the computation of the Jacobi matrix from a sequence of moments, which originates, according to Golub and Welsch [58], from personal communication with Walter Gautschi.

[7] Golub and Welsch [58] use the upper triangular matrix $\mathbf{R}$. Here, the more common representation of the Cholesky decomposition in terms of the lower triangular matrix $\mathbf{L} = \mathbf{R}^T$ is used with appropriately adjusted relationships.

recurrence coefficients:

$$\alpha_{k-1} = \frac{l_{k+1,k}}{l_{k,k}} - \frac{l_{k,k-1}}{l_{k-1,k-1}} \quad k = 1, \ldots, n, \tag{3.38}$$

$$\sqrt{\beta_k} = \frac{l_{k+1,k+1}}{l_{k,k}}, \quad k = 1, \ldots, n-1. \tag{3.39}$$

The described algorithm uses the moment matrix $\mathbf{M}_{n+1}$, which contains the first $2n+1$ moments, while only $2n$ moments are known. However, the only step in the Cholesky factorization involving m_{2n} is the calculation of $l_{n+1,n+1}$ (see e.g. [57]), which is not required to determine the recurrence coefficients with indices up to order $n-1$. Hence, the value m_{2n} does not affect the entries of $\mathbf{J}_n$ and the only limitation of the GWA for QBMMs is of a practical nature: Most of the implementations of QBMMs will make use of existing numerical linear algebra packages, where the Cholesky factorization may fail if the input matrix is not positive definite. If that is the case, one must choose m_{2n} appropriately for $\mathbf{M}_{n+1}$ to become positive definite. The most straightforward approach is to simply set m_{2n} to a very large value, as done for the study in Chapter 6. The computational complexity of the GWA is determined by that of the Cholesky decomposition, which is $O(n^3)$, see [57].

3.5. Quadrature-Based Moment Methods

3.5.1. The Quadrature Method of Moments

The first QBMM, the quadrature method of moments (QMOM), was introduced by McGraw [107] for the solution of moment transport equations corresponding to a PBE for an aerosol size distribution. The QMOM combines the methods described so far in this chapter to close moment equations like those presented in Section 2.2. For the sake of simplicity, consider a set of $2n$ moment equations derived from a univariate homogeneous PBE, such as (2.18). Moreover, it is assumed that source terms in the PBE can be expressed in an integral form that allows subsuming all terms on the RHS into a single integral term so that the moment equations can be written as

$$\frac{\mathrm{d}m_k(t)}{\mathrm{d}t} = \int_\Omega g_k(\xi) f(\xi, t) \, \mathrm{d}\xi, \quad k = 0, 1, \ldots, 2n-1, \tag{3.40}$$

where g_k is an arbitrary function defined on Ω. Given the relationships described in the previous section, the approach to close moment equations like (3.40) is relatively straightforward: Since the NDF f exhibits the mathematical properties of a weight function of a Gaussian quadrature in that it is an integrable non-negative function, it can be interpreted as such, and the integral can be approximated by an n-node Gaussian quadrature, i.e.

$$\frac{\mathrm{d}m_k(t)}{\mathrm{d}t} = \sum_{j=1}^{n} w_j g_k(\xi_j) \; + \; R_n(g_k), \tag{3.41}$$

where the quadrature nodes ξ_j and weights w_j are computed from the first $2n$ moments so that the RHS of the $2n$ moment equations depend only on the $2n$ moments and the system of moment equations is closed.

The procedure to close moment equations with the QMOM is illustrated in Figure 3.2. With a known set of $2n$ moments at time t_i, one of the algorithms described in Section 3.4 is used to compute the recurrence coefficients and assemble the Jacobi matrix $\mathbf{J}_n$ whose eigenvalues and eigenvectors then yield the abscissas and weights of the n-point quadrature. After evaluating the integral

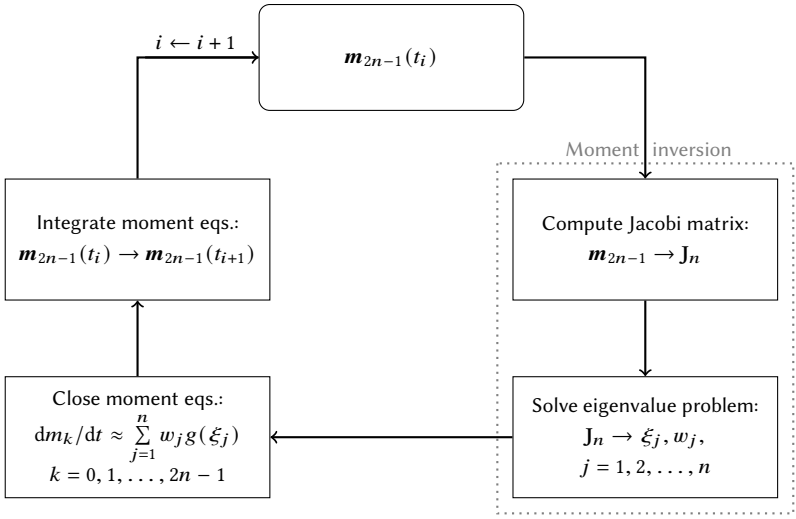

Figure 3.2.: The procedure of closing moment transport equations with the quadrature method of moments (QMOM).

terms using the computed quadrature rule, the moment equations can finally be solved with a suitable numerical method for the temporal discretization of differential equations to obtain a new set of moments at time t_{i+1}, and the entire sequence of steps is repeated as many times as desired.

As is evident in (3.16) and (3.17), the approximation error generally depends on the form of g_k. However, it is worth noting that, regardless of g_k, the quadrature is also exact ($R_n = 0$) if f represents an n-point distribution density, which can formally be expressed as a weighted sum of Dirac delta functions. Thus, it is frequently stated in the literature [96, 98, 167, 178] that the described approach is equivalent to an approximation of the NDF by

$$f(\xi) \approx \sum_{j=1}^{n} w_j \delta\left(\xi - \xi_j\right). \tag{3.42}$$

The QMOM is generally considered to be an efficient method [32, 96]. It has been successfully applied to many different problems [99, 100, 105, 114, 124, 158]. For some problems involving fluxes across phase space boundaries or strongly nonlinear, however, the QMOM is less suitable and several alternative QBMMs have been developed for such cases, one of which is described in the following section.

3.5.2. The Extended Quadrature Method of Moments

The standard QMOM described in the previous section may fail to give reasonably accurate results in certain cases, best illustrated by an example: Consider the PBE in (2.12) with $a(\xi) \neq 0$, $b(\xi) = \mathcal{S}(f, \xi) = 0$ and bounded internal-coordinate space $\Omega = [\xi_{\min}, \xi_{\max}]$. Then the kth moment equation reads, after integration by parts,

$$\frac{\mathrm{d}m_k}{\mathrm{d}t} = -\left.\xi^k a(\xi) f(\xi)\right|_{\xi=\xi_{\min}}^{\xi_{\max}} + k \int_{\Omega} \xi^{k-1} a(\xi) f(\xi)\, \mathrm{d}\xi. \tag{3.43}$$

The first term on the RHS requires pointwise values of the NDF, which are unavailable using the QMOM, considering the discontinuous representation in (3.42). Furthermore, if $a(\xi)$ is strongly nonlinear (the Gauss quadrature is exact for linear $a(\xi)$), the QMOM may require a large number of nodes n, which would result in a large number of moment transport equations. While that alone would

only affect the computational costs, a more severe problem is that the moment inversion problem can become ill-conditioned for large n [54, Sec. 2.1]. For such cases, Yuan et al. [179] used the ideas of the multi-Gaussian quadrature [20] and the kernel density element method (KDEM) [5] to extend the QMOM and allow a reconstruction of the NDF by the implementation of so-called kernel density functions (KDFs) with a presumed shape instead of Dirac delta functions. The NDF is then approximated by

$$f(\xi) \approx \sum_{j=1}^{n} w_j \delta_\sigma(\xi; \xi_j), \tag{3.44}$$

where δ_σ is a presumed KDF with the shape parameter σ, an additional variable needed for the quadrature approximation. Accordingly, the extended QMOM (EQMOM) requires a set of $2n+1$ moments. The choice of δ_σ depends primarily on the support of the NDF, Ω. Possible choices are

- Beta KDFs [179] defined on $[0, 1]$ for bounded support,
- Gamma [179], log-normal [94] or Weibull [126] KDFs defined on $[0, \infty)$ for semi-infinite support,
- Gaussian [20] and Laplace [126] KDFs defined on $(-\infty, \infty)$ for infinite support.

It should be noted that the KDFs with bounded and semi-infinite support are not limited to the standard KDF domain $[0, 1]$ and $[0, \infty)$, respectively, because moments can be transformed from the original domain to the KDF domain by a linear moment transformation. That is, if $\tilde{\Omega}$ denotes the KDF domain and the transformation $\xi \in \Omega \rightarrow \tilde{\xi} \in \tilde{\Omega}$ is given by the linear relationship

$$\tilde{\xi} = a\xi + b, \tag{3.45}$$

then the corresponding moments are calculated from the original moments by

$$\tilde{m}_k = \sum_{j=0}^{k} \binom{k}{j} a^{k-j} b^j m_{k-j}. \tag{3.46}$$

For the sake of simplicity, the rest of this section relies on the assumption that $\xi \in \tilde{\Omega}$, i.e. the given moments satisfy $m_k = \tilde{m}_k \ \forall k = 0, 1, \ldots, 2n$.

The EQMOM consists in performing an extended moment inversion to obtain a first quadrature (an n-node quadrature and the KDF-parameter σ), computing an arbitrary number, say n_{12}, of second quadrature nodes for each of the first quadrature nodes, and closing moment equations like (3.43) with the resulting nested quadrature. These steps are essentially based on the following properties of the used KDFs:

(i) The KDF $\delta_\sigma(\xi;\xi_j)$ is centered on the jth quadrature node, i.e. it has mean ξ_j, and the shape parameter σ is defined accordingly with respect to the standard parameters of the used distribution. For example, the Gaussian KDF $\delta_\sigma(\xi;\xi_j)$ corresponds to a scaled normal PDF with location parameter ξ_j and scale parameter σ.

(ii) The moments associated to the KDF $\delta_\sigma(\xi;\xi_j)$ can be calculated analytically in terms of an expression of the form

$$m_k^{(\mathrm{KDF})}(\sigma,\xi_j) = \sum_{i=0}^{k} \gamma_i(\sigma)\xi_k^i \tag{3.47}$$

where the polynomial coefficients γ_i depend on σ and the chosen KDF type.

(iii) There is a linear variable transformation $\xi \in \Omega \to \zeta \in \mathbb{B}$ such that $\delta_\sigma(\xi;\xi_j)$ can be expressed in terms of $w(\zeta)$, the weight function of a known family of orthogonal polynomials with support $\mathbb{B}$. For instance, apart from a constant factor, the Gaussian KDF centered at ξ_j

$$\delta_\sigma(\xi;\xi_j) = \frac{1}{\sqrt{2\pi}\sigma}\exp\left\{-\frac{1}{2}\left(\frac{\xi-\xi_j}{\sigma}\right)^2\right\} \tag{3.48}$$

can be expressed in terms of the weight function of the Hermite polynomials

$$w(\zeta) = \exp\left(-\zeta^2\right) \tag{3.49}$$

by the change of variable $\xi = \sqrt{2}\sigma\zeta + \xi_j$. It should be noted that this property is not necessarily satisfied by the more recently introduced KDF types, e.g. the Laplace-KDF. While this does not affect the algorithm to compute the first quadrature, the computation of the second quadrature may be significantly less efficient and possibly ill-conditioned.

From (3.44), it is obvious that

$$m_k = \sum_{j=1}^{n} w_j m_k^{(\mathrm{KDF})}(\sigma, \xi_j). \tag{3.50}$$

Thus, with the definition of the so-called degenerated moments [126], i.e. the moments corresponding to the ordinary n-point Gaussian quadrature with abscissas ξ_j and weights w_j,

$$m_k^* = \sum_{j=0}^{n} w_j \xi_j^k, \tag{3.51}$$

(3.47) and (3.50) can be expressed for $k = 0, 1, \ldots, p$ by the linear maps

$$\boldsymbol{m}_p = \mathbf{A}_p(\sigma)\boldsymbol{m}_p^*, \tag{3.52}$$

$$\boldsymbol{m}_p^* = \mathbf{A}_p^{-1}(\sigma)\boldsymbol{m}_p, \tag{3.53}$$

where $\mathbf{A}_p$ and $\mathbf{A}_p^{-1}$ are lower triangular matrices that can be computed explicitly from σ. The resulting KDF-dependent expressions as well as additional KDF-specific information needed for the inversion procedure can be found in [126, App. B].

The extended quadrature is then obtained by repeated moment inversions and conversions between the "normal" moments and degenerate moments until (3.50) is satisfied for $k = 2n$, which can be thought of as an iterative procedure to find the root of

$$\psi(\sigma) = m_{2n} - \boldsymbol{e}_{2n+1}^T \mathbf{A}_{2n}(\sigma)\boldsymbol{m}_{2n}^*, \tag{3.54}$$

where $\boldsymbol{e}_{2n+1} \in \mathbb{R}^{(2n+1)}$ is the $(2n+1)$th unit basis vector. The steps of the original extended moment inversion are shown in Figure 3.3. More recently, improved methods based on moment realizability have been proposed [126].

With an available extended quadrature, the next step is to compute an arbitrarily large number n_{12} of second quadrature nodes and weights. This can be done efficiently by exploiting the above-mentioned property (iii): For classical polynomials, the recurrence coefficients are known explicitly (see e.g. [54, Table 1.1]) so that the Jacobi matrix $\mathbf{J}_{n_{12}}$ can be assembled without an additional moment inversion, if $\delta_\sigma(\xi; \xi_j)$ can be expressed in terms of the associated weight function $w(\zeta)$. Thus, the second quadrature for each KDF can

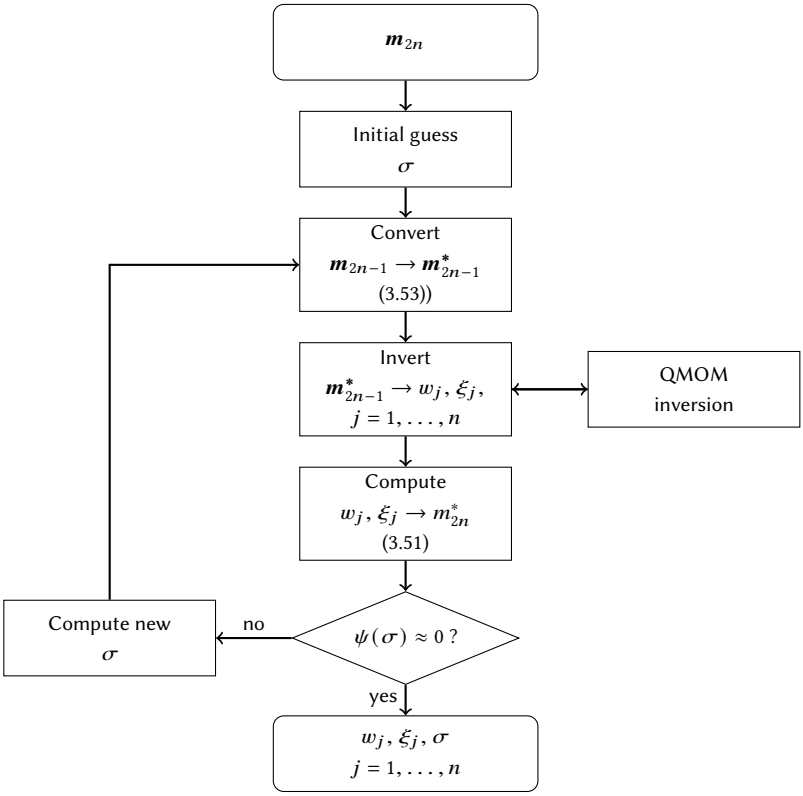

Figure 3.3.: The moment inversion algorithm of the extended quadrature method of moments (EQMOM), cf. [179]. The computation of a new σ can be done based on common iterative root finding algorithms.

be calculated by solving the eigenvalue problem related to $\mathbf{J}_{n_{12}}$ to obtain the n_{12}-node Gaussian quadrature associated with $w(\zeta)$ and then apply the linear transformation $\zeta \rightarrow \xi$ to the abscissas.

Finally, denoting the jth node and weight of the second quadrature belonging to the ith node of the first quadrature by $\xi_{i,j}$ and $w_{i,j}$, respectively, (3.43) can be closed using the reconstructed NDF and the nested quadrature:

$$m_k \approx -\sum_{j=1}^{n} \xi^k a(\xi) w_j \delta_\sigma(\xi;\xi_j)\Big|_{\xi=\xi_{\min}}^{\xi_{\max}} + k \sum_{i=1}^{n} w_i \sum_{j=1}^{n_{12}} w_{i,j} \xi_{i,j}^{k-1} a(\xi_{i,j}). \quad (3.55)$$

3.5.3. Multivariate Quadrature-Based Moment Methods

The majority of real physical problems are only adequately described by a multivariate NDF to capture relevant particle properties such as particle size and velocity components in multiple dimensions. However, the fundamental theory of Gaussian quadrature rules and orthogonal polynomials does not extend to integrals over a multidimensional domain Ω. Assuming that the moment source term in a multivariate moment transport equation of order $(k_1, k_2, \ldots, k_N)$, such as (2.16), can be written analogously to (3.40) as

$$\dot{m}_{k_1,k_2,\ldots,k_N} = \int_\Omega g_{k_1,k_2,\ldots,k_N}(\boldsymbol{\xi}) f(\boldsymbol{\xi}) \, \mathrm{d}\boldsymbol{\xi}, \tag{3.56}$$

the multivariate quadrature-based closure can formally be expressed as

$$\dot{m}_{k_1,k_2,\ldots,k_N} \approx \sum_{j=1}^{n} w_j g_{k_1,k_2,\ldots,k_N}(\boldsymbol{\xi}_j) + R_n(g_{k_1,k_2,\ldots,k_N}). \tag{3.57}$$

Detailed theoretical considerations on orthogonal polynomials of multiple variables and the associated multivariate Gaussian quadrature formulas, so-called cubature formulas, can be found in the literature, e.g. [38]. However, the existence of such cubature formulas is not guaranteed and there are no reliable methods of computation based on multivariate moment sets. Instead, alternative multivariate QBMMs have been developed that rely on additional techniques and assumptions. Examples are the direct QMOM (DQMOM)[8] [98], the tensor-product QMOM[9], the conditional QMOM (CQMOM) [178] and, particularly in the context of multivariate velocity-based NDFs, the hyperbolic version of the CQMOM (CHyQMOM) [50, 122]. However, to the author's best knowledge, there is little to no reported general theory concerning the error of such quadrature approximations. A brief summary of two of the mentioned methods, namely the tensor-product QMOM and the CQMOM, is given below, focusing

[8] In this context, it should be noted that the DQMOM differs fundamentally from the approaches underlying other QBMMs: Instead of solving a system of moment equations that are closed with a quadrature-based method, transport equations for the quadrature nodes and weights derived from the quadrature form of the moments are solved directly.

[9] The term *tensor-product QMOM* is used by Marchisio and Fox [96] to refer to a generalized form of the related methods proposed in [177] and [44].

on common problems as well as the importance of the univariate moment inversion for multivariate QBMMs.

The *tensor-product QMOM* [44, 96, 177] uses the pure moments, i.e. the moments associated with the marginal distribution of only one internal coordinate, to compute a univariate Gaussian quadrature in each dimension, resulting in a total of N univariate moment inversions. Then, denoting the number of nodes in ith dimension by n_i, all possible combinations yield $n = n_1 n_2 \cdots n_N$ N-dimensional quadrature nodes. The corresponding weights are computed by solving the linear system

$$m_{k_1,k_2,\ldots,k_N} = \sum_{j=1}^{n} w_j \xi_1^{k_1} \xi_2^{k_2} \cdots \xi_N^{k_N} \tag{3.58}$$

to force agreement of the multivariate quadrature with the pure moments as well as the required number of additional mixed moments for (3.58) to have a unique solution. However, the resulting weights may be negative, and the preservation of moment realizability is thus not guaranteed.

The *CQMOM* [178] is based on Bayes' theorem (here in two dimensions for the sake of simplicity)

$$f(\xi_1, \xi_2) = f(\xi_2|\xi_1) f(\xi_1), \tag{3.59}$$

where $f(\xi_2|\xi_1)$ denotes the conditional density of ξ_2 given ξ_1, and $f(\xi_1)$ the marginal distribution density of ξ_1. Then, letting $\Omega = \Omega_1 \times \Omega_2$, $\xi_1 \in \Omega_1$ and $\xi_2 \in \Omega_2$, the moment of order (k, l) can be written as

$$\begin{aligned} m_{k,l} &= \int_{\Omega_1} \int_{\Omega_2} \xi_1^k \xi_2^l f(\xi_2|\xi_1) f(\xi_1) \, \mathrm{d}\xi_2 \, \mathrm{d}\xi_1 \\ &= \int_{\Omega_1} \xi_1^k \underbrace{\left[\int_{\Omega_2} \xi_2^l f(\xi_2|\xi_1) \, \mathrm{d}\xi_2 \right]}_{=: \langle \xi_2^l \rangle (\xi_1)} f(\xi_1) \, \mathrm{d}\xi_1, \end{aligned} \tag{3.60}$$

where $\langle \xi_2^l \rangle (\xi_1)$ is referred to as conditional moment. Thus, using an n_1-node Gaussian quadrature in the first dimension yields

$$m_{k,l} = \sum_{j=1}^{n_1} w_{1,j} \xi_{1,j}^k \langle \xi_2^l \rangle (\xi_{1,j}). \tag{3.61}$$

Assuming that n_2 quadrature nodes in the second dimension are desired for each node in the first dimension, and that all the required moments on the LHS are available, the next step is to solve the linear system given by (3.61) with $k = 0, 1, \ldots, n_1 - 1$ and $l = 0, \ldots, 2n_2 - 1$ to obtain n_1 sets of $2n_2$ conditional moments and finally, applying a moment inversion algorithm, n_1 conditional n_2-node quadratures. However, realizability of the conditional moment sets is by no means guaranteed, which may cause the inversion algorithm to fail unless the order of the approximation is reduced, as proposed by Yuan and Fox [178]. The extension of the CQMOM to arbitrary dimensions is possible considering

$$f(\xi_1, \xi_2, \ldots, \xi_N) = f(\xi_N|\xi_1, \ldots, \xi_{N-1}) \cdots f(\xi_2|\xi_1) f(\xi_1), \tag{3.62}$$

In the N-dimensional case, the CQMOM involves $1 + n_1 n_2 \cdots n_{N-1}$ univariate moment inversions.

4. Modeling Droplet Breakup with Quadrature-Based Moment Methods

The PBEs and the derived moment equations in Chapter 2 contain a source term $\mathcal{S}$ that has not been further detailed up to this point. It represents all processes that can be considered discontinuous at the particle scale. One such process is particle breakup, which occurs in flow regimes where destabilizing inertial forces are dominant with respect to the stabilizing surface tension forces. Then particles, typically bubbles or droplets, break up into smaller particles and continue disintegrating until the fragments reach a stable size. This chapter is focused on the breakup of liquid droplets, which is often a dominant process in particulate systems comprising a dispersed liquid such as sprays.

Numerous breakup models for PBEs have been proposed in the past. A comprehensive overview is given in the review article by Liao and Lucas [90]. The majority of those models, however, are suited to bubbles, since they are based on the assumption that collisions with turbulent eddies in the carrier fluid are the primary mechanism of fragmentation, whereas the breakup of liquid droplets is usually caused by surface instabilities, such as Rayleigh-Taylor (RT) [83] and Kelvin-Helmholtz (KH) instabilities [111]. Depending on the flow regime and the dominant type of surface instabilities, different breakup modes have been observed. A considerable number of theoretical, numerical and experimental studies imply that the most important breakup modes present in liquid dispersions are those referred to as bag breakup and shear breakup. An established model for these breakup modes is the model of Reitz and Diwakar [138, 139], which was originally developed for the Eulerian-Lagrangian simulation of sprays under conditions typical in internal combustion engines.

The objective of the research reported in this chapter is to formulate the Reitz-Diwakar model, serving as a representative example for a simple Lagrangian model, for QBMMs and numerically investigate the behavior in a spatially homogeneous setup compared to a Monte-Carlo method. For this purpose, a brief review of the physical background in terms of breakup mechanisms is given first. Then, after a description of the general form of the breakage term, the Lagrangian model is formulated as a source term in the PBE and subsequently for QBMMs. Following that, important results of numerical investigations of droplet breakup with QBMMs are presented and discussed, before finalizing this chapter with a summary of major conclusions.

4.1. Mechanisms of Droplet Breakup

As opposed to bubbly flows where collisions with turbulent eddies in the surrounding fluid are commonly considered to be the primary cause of fragmentation, the breakup of liquid droplets is commonly attributed to growing surface waves due to RT or KH instabilities. RT instabilities [83] occur at the interface of two fluids with different densities where the lighter fluid is accelerating into the heavier one, which constitutes an inherently unstable system due to waves at the flat surface that grow exponentially with time. The KH instability [111] is a shear-induced surface instability that occurs in systems of two fluids with a velocity difference across the interface. As a consequence of the growth of surface waves induced by small disturbances in the (linear) tangential velocity, the interface becomes unstable exhibiting vortical structures.

Both mentioned types of surface instabilities are a consequence of inertial forces due to a relative velocity between droplet and carrier fluid and eventually lead to breakup when the destabilizing effect of growing surface waves exceeds the stabilizing effect of surface tension. Thus, the behavior of droplet breakup is primarily characterized by the dimensionless Weber number that quantifies the relative importance of inertial forces with respect to surface tension forces. It is defined by

$$\mathrm{We} = \frac{d\rho_f u_r}{\sigma_l}, \tag{4.1}$$

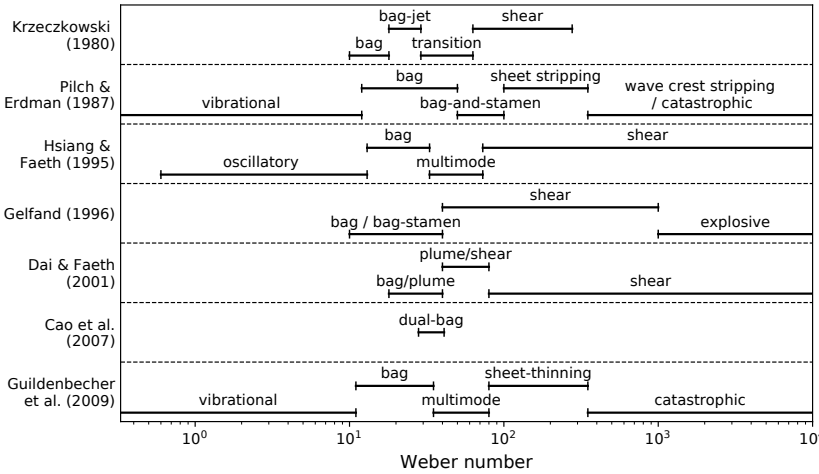

Figure 4.1.: Breakup modes at low Ohnesorge numbers identified in different studies of Krzeczkowski [81], Pilch and Erdman [127], Hsiang and Faeth [71], Gelfand [55], Dai and Faeth [27], Cao et al. [18], Guildenbecher et al. [64].

where d is the droplet diameter, ρ_f the density of the carrier fluid, u_r the relative velocity between fluid and droplet and σ_l the liquid surface tension.

The identification of breakup modes has been the subject of numerous studies. Figure 4.1 illustrates the breakup regimes reported by different authors for low Ohnesorge numbers[1], depending only on the droplet Weber number.

Considering the use of various terms for identical breakup morphologies, five distinct modes of droplet breakup have been observed:

(1) *Vibrational breakup* refers to the fragmentation of a drop in the absence of aerodynamic forces. This type of breakup is driven solely by oscillations of the drop at is natural frequency due to surface tension. Since this mechanism is very slow and the resulting fragment sizes are large, it is commonly ignored [64].

[1]The Ohnesorge number is defined in terms of the Weber and Reynolds number as $\mathrm{Oh} = \sqrt{\mathrm{We}}/\mathrm{Re}$ and quantifies the importance of viscous effects.

(2) *Bag breakup* occurs when the Weber number exceeds a critical value. Assuming that viscous effects are negligible, an approximate value consistently stated in the literature is $We \gtrsim 11$. Bag breakup is always initiated by a deformation, increasing the surface area perpendicular to the dominant flow direction, until a bag-like structure is formed. Subsequently, the first breakup of the bag results in the formation of a toroidal ring and small fragments of almost equal sizes. The ring then disintegrates into smaller droplets, which have been observed to be considerably larger than the fragments of the initial bag breakup [24]. The large surface area perpendicular to the flow suggests that RT-instabilities play a major role in the bag breakup regime, which is supported by several experimental, numerical and theoretical studies [72, 82, 159, 161, 180, 181]. As vibrational breakup is usually neglected, the onset of bag breakup is considered the first criticality.

(3) *Shear breakup* is a breakup mode associated with high Weber numbers. It is characterized by a sheet that is stripped from the periphery of the deformed droplet and breaks up into smaller droplets, while the coherent core drop remains until after disintegration. It is also referred to as sheet stripping and sheet thinning in Figure 4.1. Experimental and numerical studies as well as theoretical considerations suggest that KH instabilities are the primary cause of shear breakup [159, 161].

(4) *Multimode breakup* refers to the transition from bag to shear breakup. Different breakup morphologies in this regime have been identified as shown in Figure 4.1. It is assumed that the physical mechanisms as well as the morphologies are some combination of bag and shear breakup [64].

(5) *Catastrophic breakup* is attributed to large-amplitude surface waves that penetrate a drop and initiate a cascading process in which fragments can undergo multiple consecutive breakups [127]. However, it has also been suggested that catastrophic breakup does not exist [160].

It can be concluded from the brief review above that three breakup modes are dominant in particulate systems involving dispersed droplets: bag breakup, shear breakup and multimode breakup, which is assumed to be a combination of the former two.

4.2. The Breakup Term in Moment Equations

Up to this point, the source term due to discontinuous events $\mathcal{S}$ that appears in the PBE (2.10) and the derived moment equations (2.16) has not been further specified. Considering a measure of particle size $\xi \in (0, \infty)$ as the only internal coordinate and assuming the absence of all discontinuous processes other than breakup, the source term can be written as [96, 136]

$$\mathcal{S}(\xi) = \int_{\xi}^{\infty} \nu(\xi')\beta(\xi|\xi')f(\xi')\,\mathrm{d}\xi' - \nu(\xi)f(\xi), \tag{4.2}$$

where $\nu(\xi)$ is the breakup rate and the function $\beta(\xi|\xi')$ is the conditional fragment size distribution of ξ given the pre-breakup size ξ'. The first term on the RHS is the birth term accounting for the generation of new particles as a result of fragmentation. The second term on the RHS represents the disappearance of particles.

Let the moment transform of the breakup source term be defined as

$$\mathcal{B}_k \coloneqq \int_0^{\infty} \xi^k \mathcal{S}(\xi)\,\mathrm{d}\xi. \tag{4.3}$$

Then the source term in the kth moment equation reads

$$\mathcal{B}_k = \int_0^{\infty} \xi^k \int_{\xi}^{\infty} \nu(\xi')\beta(\xi|\xi')f(\xi')\,\mathrm{d}\xi'\,\mathrm{d}\xi - \int_0^{\infty} \xi^k \nu(\xi)f(\xi)\,\mathrm{d}\xi. \tag{4.4}$$

This can can also be written as [136, Sec. 3.2.2]

$$\mathcal{B}_k = \int_0^{\infty} \nu(\xi')f(\xi') \int_0^{\xi'} \xi^k \beta(\xi|\xi')\,\mathrm{d}\xi\,\mathrm{d}\xi' - \int_0^{\infty} \xi^k \nu(\xi)f(\xi)\,\mathrm{d}\xi. \tag{4.5}$$

Finally, using an n-point quadrature rule, the source term in the kth moment equation can be approximated by

$$\mathcal{B}_k \approx \sum_{j=1}^{n} w_j \nu(\xi_j) \left[\int_0^{\xi_j} \xi^k \beta(\xi|\xi_j)\,\mathrm{d}\xi - \xi_j^k \right], \tag{4.6}$$

which can be computed efficiently if an analytical expression exists for the inner integral.

4.3. Formulation of the Reitz-Diwakar Breakup Model for Quadrature-Based Moment Methods

The Reitz-Diwakar model [138, 139] is an established Lagrangian model for the bag and shear breakup[2] mode, originally developed for fuel sprays in engines. In this section, the model is formulated in terms of a population balance model and finally as a model for QBMMs.

According to the Reitz-Diwakar model, breakup occurs if

$$\mathrm{We} \geq C_{\mathrm{bag}}, \tag{4.7}$$

where C_{bag} is a model constant defining the critical Weber number for bag breakup.[3] If (4.7) is satisfied, the breakup mode is determined by a second condition: Shear breakup occurs if

$$\frac{\mathrm{We}}{\sqrt{\mathrm{Re}_{\mathrm{p}}}} \geq C_{\mathrm{shear}}, \tag{4.8}$$

where the particle Reynolds number is defined as

$$\mathrm{Re}_{\mathrm{p}} = \frac{u_r d}{\nu_f}, \tag{4.9}$$

and C_{shear} is a model constant of order unity. Otherwise, the breakup mode is assumed to be bag breakup. Once the type of breakup is known, the breakup rate and the fragment sizes need to be determined. As regards the latter, the Reitz-Diwakar model is based on a very simple idea, namely that the size of droplets produced by breakup is exactly the critical droplet size. In other words, a constant fragment size is chosen such that the inequalities in (4.7) or (4.8) (depending on the breakup regime) become equalities.

[2] In the original publication the breakup mode is referred to as "stripping breakup". Here, the term "shear breakup" is used for the sake of consistency with earlier sections.

[3] Here the original limits for the two considered breakup modes, based on an earlier experimental study [116], are replaced by general model constants.

As to the breakup frequency, the lifetimes of unstable droplets are given by[4]

$$\tau_{\text{bag}} = D_{\text{bag}} \sqrt{\frac{\rho_p d^3}{\sigma_l}}, \tag{4.10}$$

$$\tau_{\text{shear}} = D_{\text{shear}} \frac{d}{u_r} \sqrt{\frac{\rho_p}{\rho_f}}. \tag{4.11}$$

where ρ_p is the droplet (particle) density and D_{bag} and D_{shear} are model constants of order unity.

For the mesoscopic formulation, let the only internal coordinate be the droplet diameter, i.e. $\xi = d$. Then, taking into account the definitions of the Weber and Reynolds number, the breakup limits in (4.7) and (4.8) can be expressed in terms of the critical droplet sizes

$$\hat{\xi}_{\text{bag}} = C_{\text{bag}} \frac{\sigma_l}{\rho_f u_r^2}, \tag{4.12}$$

$$\hat{\xi}_{\text{shear}} = C_{\text{shear}}^2 \frac{\sigma_l^2}{\rho_f^2 \nu_f u_r^3}, \tag{4.13}$$

As mentioned above, the Reitz-Diwakar model assumes a constant fragment size equal to the critical size of the respective breakup mode. Thus, the fragment size distributions can be expressed as Dirac delta functions centered at the critical size, i.e.[5]

$$\beta_{\text{mode}}(\xi|\xi') = \left(\frac{\xi'}{\xi}\right)^3 \delta\left(\xi - \hat{\xi}_{\text{mode}}\right), \tag{4.14}$$

where "mode" represents either "bag" or "shear". The factor $(\xi'/\xi)^3$ ensures the conservation of mass.

The breakup frequencies are simply the reciprocals of the droplet lifetimes in (4.10) and (4.11). To mathematically express the above-described conditions for

[4]The original model was formulated in terms of the droplet radius instead of the droplet diameter. However, the difference can be taken into account by choosing the model constants appropriately.

[5]It should be noted that, in the original Lagrangian model, the fragment size is determined by a rate equation corresponding to a continuously shrinking droplet rather than discontinuous fragmentation.

breakup, one can use the Heaviside step function

$$\Theta(\xi) = \begin{cases} 1 & \text{if } \xi > 0, \\ 0 & \text{otherwise.} \end{cases} \tag{4.15}$$

Then the breakup rates corresponding to the two considered breakup modes can be written as

$$\nu_{\text{bag}}(\xi) = \Theta(\xi - \hat{\xi}_{\text{bag}}) \left[1 - \Theta(\xi - \hat{\xi}_{\text{shear}})\right] D_{\text{bag}}^{-1} \sqrt{\frac{\sigma_l}{\rho_f}} \xi^{-3/2}, \tag{4.16}$$

$$\nu_{\text{shear}}(\xi) = \Theta(\xi - \hat{\xi}_{\text{bag}}) \Theta(\xi - \hat{\xi}_{\text{shear}}) D_{\text{shear}}^{-1} \sqrt{\frac{\rho_f}{\rho_p}} u_r \xi^{-1}. \tag{4.17}$$

The factor $1 - \Theta(\xi - \hat{\xi}_{\text{shear}})$ in (4.16) accounts for the model assumption that bag breakup only takes place if the condition for shear breakup in (4.8) is not satisfied. The breakup term in the PBE then results from the sum of bag and shear breakup:

$$\begin{aligned} \mathcal{S}(\xi) = &\int_{\xi}^{\infty} \left[\nu_{\text{bag}}(\xi')\beta_{\text{bag}}(\xi|\xi') + \nu_{\text{shear}}(\xi')\beta_{\text{shear}}(\xi|\xi')\right] f(\xi') \, \mathrm{d}\xi' \\ &- \left[\nu_{\text{bag}}(\xi) + \nu_{\text{shear}}(\xi)\right] f(\xi). \end{aligned} \tag{4.18}$$

Finally, substitution into (4.6) and integration yields the source term in the kth moment equation in quadrature form:

$$\begin{aligned} \mathcal{B}_k \approx \sum_{j=1}^{n} \Bigg[&[1 - \Theta(\xi_j - \hat{\xi}_{\text{shear}})] D_{\text{bag}}^{-1} \sqrt{\frac{\sigma_l}{\rho_f}} \left(\hat{\xi}_{\text{bag}}^{k-3} \xi_j^{3/2} - \xi_j^{k-3/2}\right) \\ &+ \Theta(\xi_j - \hat{\xi}_{\text{shear}}) D_{\text{shear}}^{-1} \sqrt{\frac{\rho_f}{\rho_p}} \left(\hat{\xi}_{\text{shear}}^{k-3} \xi_j^2 - \xi_j^{k-1}\right) \Bigg] w_j \Theta(\xi_j - \hat{\xi}_{\text{bag}}). \end{aligned} \tag{4.19}$$

It is easy to verify that $\mathcal{B}_3 = 0$, i.e. mass is conserved. In the following section, the expression above is investigated in comparison to the original form of the Reitz-Diwakar model using a spatially homogeneous univariate configuration.

4.4. Numerical Tests

In this section, major results of numerical investigations of the Reitz-Diwakar model for droplet breakup using QBMMs are presented and discussed. The

study consists of three test cases. The general approach and the main features of the different test cases are described in Section 4.4.1 below. Following that, results of the tests are discussed one by one in Sections 4.4.2–4.4.4.

4.4.1. Summary of Test Cases

The numerical investigations in this section include three different test cases that are all based on the assumption of constant fluid properties. These fluid properties as well as other parameters that are uniformly used in all test cases are summarized in Table 4.1.

Table 4.1.: Uniform parameters used in all test cases for the numerical investigation of droplet breakup with QBMMs.

Quantity	Value	Unit
Droplet density ρ_p	1000	kg/m^3
Fluid density ρ_f	1.3	kg/m^3
Liquid surface tension σ_l	0.05	N/m
Relative velocity u_r	60	m/s
Model constant C_{bag}	12	-
Model constant C_{shear}	0.5	-
Model constant D_{bag}	0.785 ($\approx \pi/4$, cf. [139])	-
Model constant D_{shear}	10	-

In all three test cases, QBMMs are employed to solve the system of moment equations

$$\frac{\mathrm{d}m_k}{\mathrm{d}t} = \mathcal{B}_k, \quad k = 0, 1, \ldots, \tag{4.20}$$

where the RHS results from the breakup term derived in Section 4.3. For all test cases, the temporal derivative was discretized using a simple explicit Euler method. Thus, denoting the numerical solution at time t_i by m_k^i, the solution at time t_{i+1} is given by

$$m_k^{i+1} = m_k^i + \Delta t \mathcal{B}_k. \tag{4.21}$$

As the Euler method is only first-order accurate, a sufficiently small step size $\Delta t = 10^{-7}$ s was determined experimentally. The explicit Euler method was chosen due to its simplicity and relative robustness with regard to moment realizability in cases where the moment sequence is on or close to the moment space boundary, which is a common situation in the configurations investigated in this section. For more detailed considerations on the problem of moment realizability with respect to the temporal discretization of moment equations, see Section 5.3.

Differences between the test cases in terms of properties of the droplet population and breakup modes were created by varying only the fluid viscosity and the initial distribution of droplet sizes. These parameters and the resulting dimensionless numbers and breakup modes are given in Table 4.2. It is important to note that, in this context, the breakup mode referred to as multimode breakup describes the simultaneous presence of bag and shear breakup.

Table 4.2.: Varied parameters in different test cases for the numerical investigation of droplet breakup with QBMMs.

	Case 1	Case 2	Case 3
Dynamic viscosity $\rho_f \nu_f$	$4 \cdot 10^{-5}$ Pa s	$1 \cdot 10^{-5}$ Pa s	$4 \cdot 10^{-5}$ Pa s
Initial distribution	Delta	Delta	Log-normal
Weber number We	93.6	93.6	17…491
Particle Reynolds number $\mathrm{Re_p}$	1950	7800	361…10239
Breakup mode	Shear	Multimode	Multimode

The first two test cases are based on initially monodisperse populations, i.e. droplets with equal sizes. They serve as simple tests to validate the quadrature-based moment model and implementation, as both configurations correspond to discrete distributions where the QMOM with a sufficient number of nodes is an exact representation. As the EQMOM is, in such cases, equivalent to the QMOM, only the QMOM is used for the first two cases. The third test involves more realistic initial droplet sizes sampled from a log-normal distribution. For Case 3, the Gamma-EQMOM was also employed in addition to the QMOM. In

all cases, the "Lagrangian" model[6] described by the expressions (4.7)–(4.11) is used as a reference solution. More precisely, the relationships in (4.7)–(4.11) are applied to each sample, and the reference moments are computed from the resulting discrete distribution. With respect to Case 3, the method to compute the reference solution can be thought of as a Monte-Carlo method.

In the following sections, the used QBMMs are indicated first by the general type of method and second by the number of moments. For example, the six-moment (three-node) QMOM is referred to as QMOM-6 and the seven-moment (three-node) EQMOM by EQMOM-7. As only Gamma-KDFs were used with the EQMOM, the explicit labeling as Gamma-EQMOM is omitted for brevity.

4.4.2. Case 1: Shear Breakup of Monodisperse Droplets

This first test case is characterized by an initially monodisperse population in the shear breakup regime. Because of the constant fragment size produced by breakup according to the Reitz-Diwakar model, the NDF is, at all times, represented by the two-point distribution density

$$f(\xi) = \sum_{j=1}^{2} w_j \delta(\xi - \xi_j), \quad \xi_1 = \xi^{(0)},\ \xi_2 = \hat{\xi}_{\text{shear}},\ w_1, w_2 \geq 0, \tag{4.22}$$

where $\xi^{(0)}$ is the initial constant droplet size. Therefore, the QMOM using two Gaussian quadrature nodes is exact, and solving four moment equations is sufficient to obtain the exact solution (except for round-off errors). This is shown in Figure 4.2 for the zeroth moment, which is equal to the total number of droplets. Not surprisingly, the QMOM-2, considering only a mean droplet size, produces very large errors and underestimates breakup significantly after initially rapid breakup. The QMOM-4, on the other hand, yields accurate results as expected. As the two-node representation is exact, i.e. $\boldsymbol{m}_5 \in \partial\mathcal{M}_5$ and thus $\beta_2 = 0$, the solution of the eigenvalue problem associated with the Jacobi matrix $\mathbf{J}_3$ results in at least one zero-weight, and the QMOM-6 yields results that are practically identical to those of the QMOM-4.

[6] It should be noted that, while the Reitz-Diwakar model was originally developed for Eulerian-Lagrangian simulations, the term "Lagrangian" is (strictly speaking) not meaningful in a spatially zero-dimensional context.

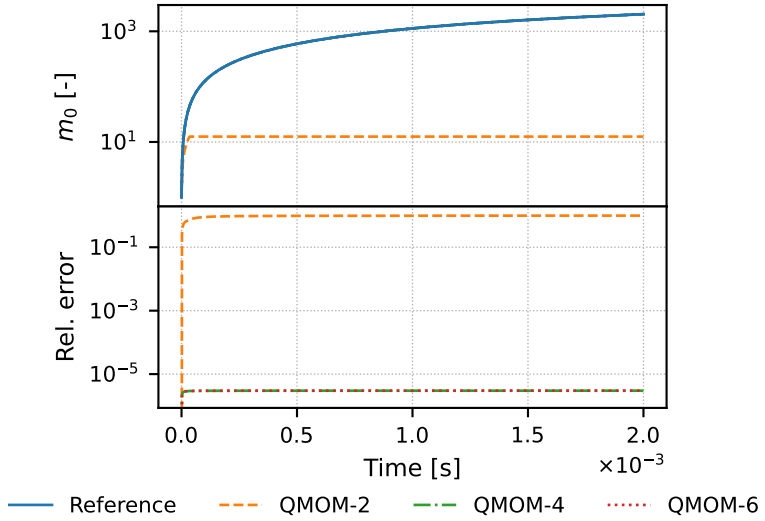

Figure 4.2.: Temporal evolution of the total number of droplets (top) and relative error (bottom) for Case 1.

Figure 4.3 shows the temporal evolution of the mean diameter m_1/m_0. Since all transported moments are theoretically exact using the QMOM with two or more nodes, the QMOM-4 and QMOM-6 produce accurate results, while, as a consequence of the underestimated breakup, the mean diameter is drastically overpredicted using the QMOM-2. A similar trend can be observed in Figure 4.4, which shows the Sauter mean diameter (SMD) m_3/m_2, a physically important measure of the volume-to-surface ratio. As neither m_2 nor m_3 are considered when using the QMOM-2, they were reconstructed from the one-node quadrature, and the shown SMD is thus equal to the mean diameter in Figure 4.3. In addition to the demonstrated lack of accuracy, the fact that m_3 is not a transported moment makes the QMOM-2 non-conservative in terms of mass and thus unsuitable for this type of problem when using diameter as the internal coordinate. An alternative approach is to use volume as the internal coordinate instead. In that case, however, the surface is not computed accurately, which is important for several processes involving e.g. mass and heat transfer in more complex configurations. Due to the lack of mass conservation, methods that do

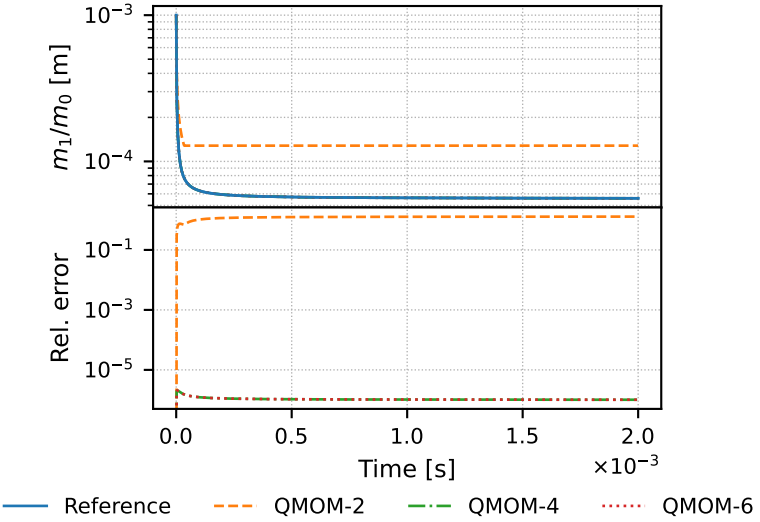

Figure 4.3.: Temporal evolution of the mean diameter (top) and relative error (bottom) for Case 1.

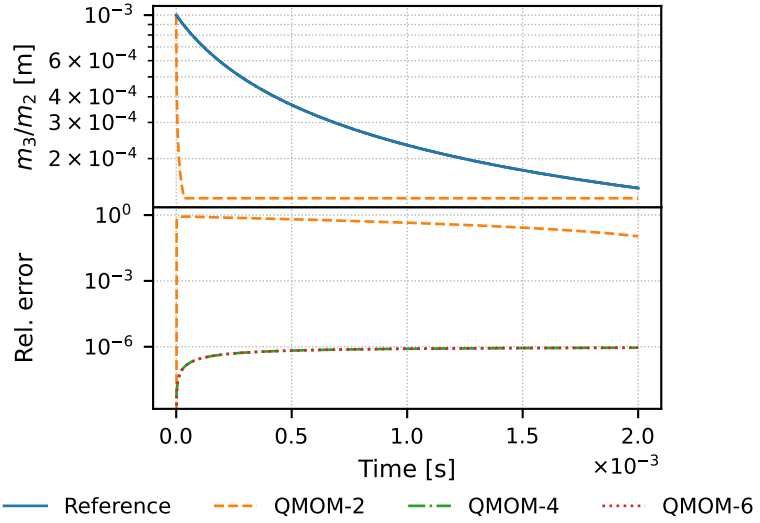

Figure 4.4.: Temporal evolution of the Sauter mean diameter (top) and relative error (bottom) for Case 1.

not involve an equation for m_3 are hereinafter disregarded. As for the higher-order methods, it is worth mentioning that, by virtue of the preservation of m_3, the SMD depends only on m_2.

In summary, the results of the first test case demonstrate that the formulation of the quadrature-based moment model in Section 4.3 corresponds to the original Lagrangian model in the shear breakup regime. Moreover, the QMOM-2 was clearly shown to be unsuitable for the investigated kind of problem, not only due to the previously known lack of mass conservation, but also generally poor accuracy.

4.4.3. Case 2: Multimode Breakup of Monodisperse Droplets

The second case serves as a test to validate the quadrature-based formulation of the Reitz-Diwakar model in the bag breakup regime. As the model has already been validated for shear breakup, this is done using parameters corresponding to the multimode breakup regime (see Table 4.2), which is used here to describe the presence of both bag and shear breakup. Starting with the same monodisperse population as in the previous section, the fluid viscosity is chosen such that the fragments of the initial shear breakup are in the bag breakup regime. As a result, the NDF is a three-point distribution density, similar to that in (4.22), only with one additional node $\xi_3 = \hat{\xi}_{\mathrm{bag}}$. Thus, the considerations in the previous section can be transferred to the case of a three-node distribution density in that the QMOM must be exact with six or more transported moments. This is confirmed by the results in terms of the total number of droplets in Figure 4.5 and the SMD in Figure 4.6. As expected, the QMOM-6 and QMOM-8 are accurate, whereas the results of the QMOM-4 display relative errors in the ten-percent range.

It can be concluded from the second test case that the formulation of the quadrature-based moment model in Section 4.3 is consistent with respect to the original Lagrangian model for both considered breakup modes. Furthermore, the QMOM-4 produces relatively large errors. However, this setup involving a three-node distribution is very specific, and the latter result should not be generalized to configurations involving continuous distributions.

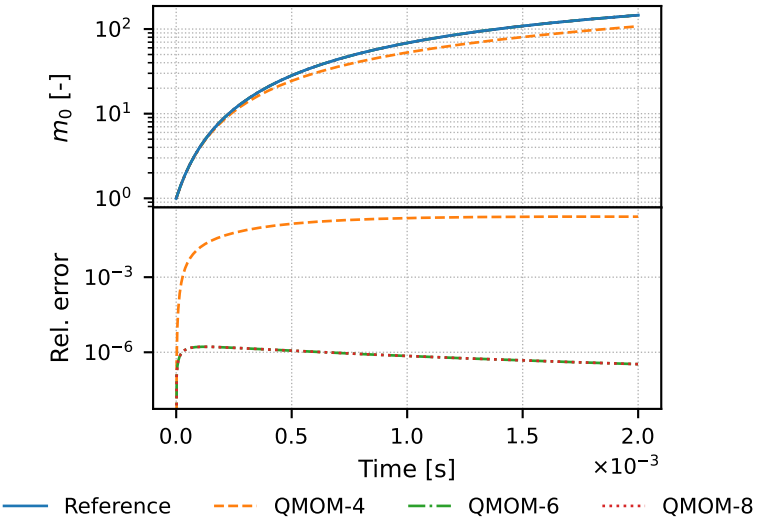

Figure 4.5.: Temporal evolution of the total number of droplets (top) and relative error (bottom) for Case 2.

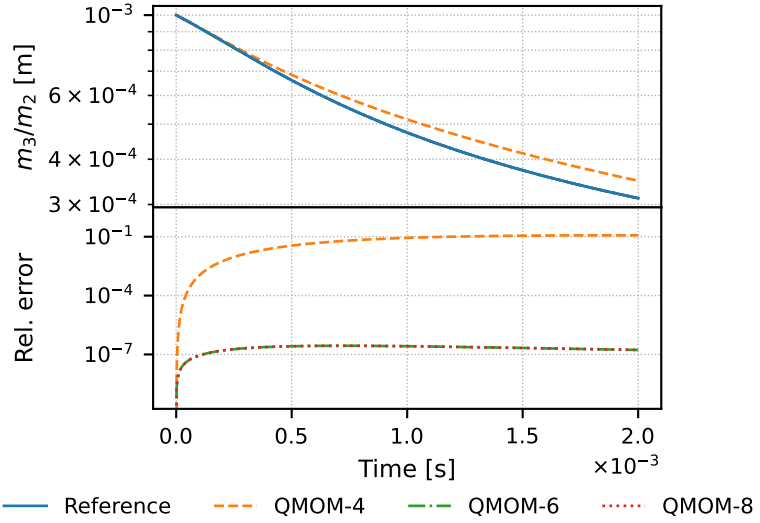

Figure 4.6.: Temporal evolution of the Sauter mean diameter (top) and relative error (bottom) for Case 2.

4.4.4. Case 3: Multimode Breakup of Polydisperse Droplets

The third test case is characterized by a more realistic polydisperse initial population of droplets with 1000 different sizes that were sampled from a log-normal distribution. These samples were then used as the initial condition to compute the reference solution, and the moments resulting from the discrete distribution as the initial condition for QBMMs. The distribution of Weber numbers resulting from the sampled droplet sizes and the chosen parameters in Tables 4.1 and 4.2 is shown in Figure 4.7. In addition to the QMOM, the EQMOM was also employed in this case, using Gamma-KDFs and ten second quadrature nodes for each point of the first quadrature. This number was determined in a pre-test that showed no further improvement when using up to 100 second quadrature nodes, see Appendix A.2 for additional information.

The temporal evolution of the total number of droplets resulting from the solution of up to ten moment equations with the QMOM and the EQMOM is shown in Figure 4.8. It can be seen that the QMOM using six or more moments produces relative errors of about 1 % or less over the entire observed time interval, even less than 0.1 % in case of the QMOM-10. This can be deemed reasonably accurate considering the discontinuous integrand in the moment equations as well as the considerable deviation of the actual distribution in Figure 4.7 from a three-point or five-point distribution, which are the equivalent approximations corresponding to the QMOM-6 and QMOM-10, respectively. The continuous

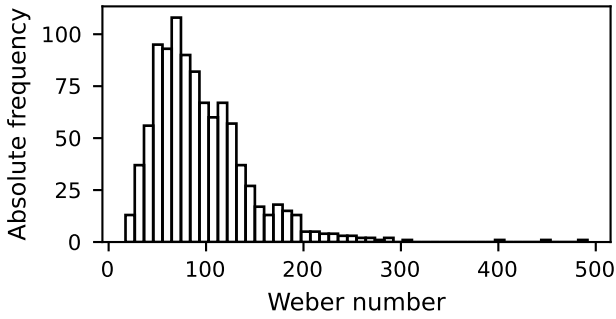

Figure 4.7.: Distribution of Weber numbers in the initial droplet population for Case 3.

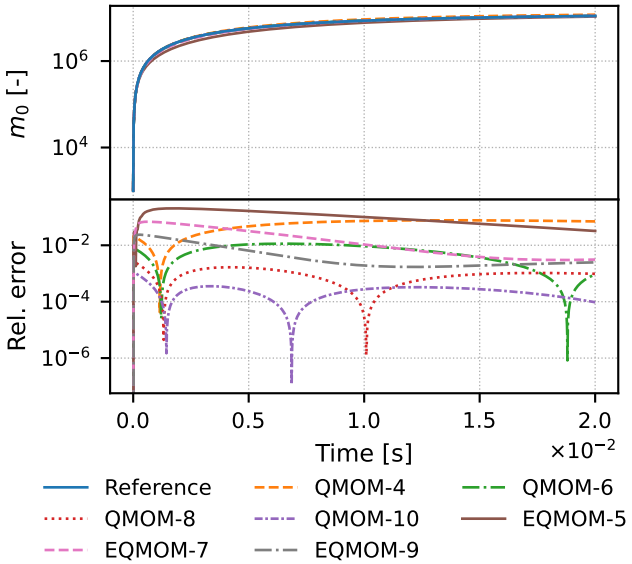

Figure 4.8.: Temporal evolution of the total number of droplets (top) and relative error (bottom) for Case 3.

NDF reconstruction by the EQMOM does not lead to any improvement. On the contrary, the results of the QMOM are consistently more accurate compared to an EQMOM approximation of similar order. Especially in the beginning, the results of the EQMOM display a significant difference with respect to the reference solution. A possible explanation is given by the continuous NDF reconstructions by the EQMOM shown Figure 4.9, where substantial differences from the actual distribution can be observed in certain regions. This may lead to significant deviations in the predicted fragmentation, particularly in combination with the discontinuous breakup term due to critical limits in the model formulation. However, this effect fades over time. Apart from the absolute deviation from the reference solution, the used QBMMs display the generally expected trend that the accuracy increases with the number of moment equations in all cases. This is also true for higher-order methods (see Appendix A.2). Similar trends as for the zeroth moment, which is of secondary importance with regard to most physical applications, can be observed for the SMD shown in Figure 4.10.

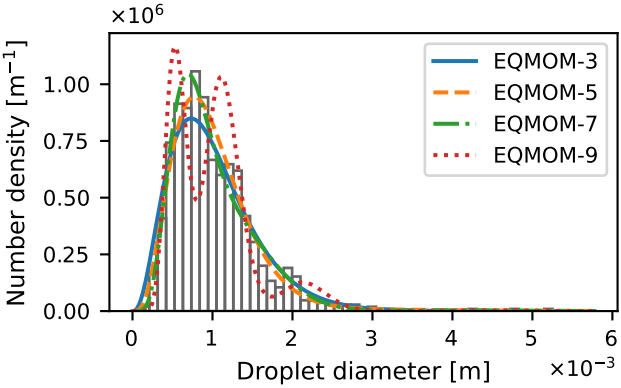

Figure 4.9.: Comparison of the continuous NDF reconstructions by the Gamma-EQMOM and the actual initial size distribution at $t = 0$.

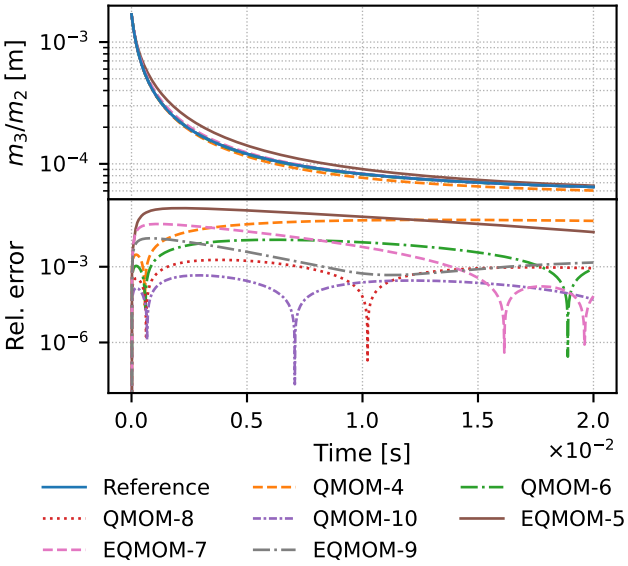

Figure 4.10.: Temporal evolution of the Sauter mean diameter (top) and relative error (bottom) for Case 3.

Moreover, it is evident that the differences between QBMMs with six or more transported moments vanish as time progresses and the system approaches a three-point distribution similar to that in Section 4.4.3.

In conclusion, the third test case showed that QBMMs can be used to efficiently and accurately approximate the moment source terms due to the Reitz-Diwakar breakup model. However, no improvements could be achieved by using the EQMOM instead of the QMOM in this specific case where the modeled population tends to a three-point distribution.

4.5. Summary and Conclusion

In this chapter, the Reitz-Diwakar model for droplet breakup, originally developed as a Lagrangian model, was formulated as a population balance model in terms of a breakage term in the univariate spatially homogeneous PBE. The derived system of moment equations was solved using different QBMMs, namely the QMOM and the EQMOM with Gamma-KDFs. The major conclusions from the numerical results can be summarized as follows:

- In general, QBMMs are suitable methods to approximate solutions to the moment source terms derived from the Reitz-Diwakar breakup model with adequate accuracy.
- For the specific configurations investigated in this chapter, the Gamma-EQMOM with its continuous reconstruction of the NDF does not provide any benefits compared to the QMOM. The numerical results suggest two possible reasons for that. First, the studied system tends to a discrete distribution with only a few different sizes where a continuous NDF is not an appropriate representation. Second, the differences between the actual initial size distribution and the reconstruction may be significant in regions that are particularly relevant for the modeled process. While the former is very specific to the problems investigated in this chapter, the latter is a rather general problem of methods that assume a functional form of the NDF.
- Using the Reitz-Diwakar model that allows two possible fragment sizes given a specific state of the carrier fluid, at least six moments should be

considered to obtain a reasonably accurate solution. While the presented results are limited to spatially homogeneous systems, this statement also applies to the numerical simulation of inhomogeneous systems where the computation of the moment source terms for some interval $[t, t + \Delta t]$ is typically based on constant fluid properties in each cell of the discretized spatial domain.

As a concluding remark, it is worth noting that, contrary to Lagrangian models, QBMMs are well-suited for breakup terms involving more complex fragment size distributions than the assumed constant fragment size, which could be a possible extension to more accurately model the physics of droplet breakup with QBMMs.

5. Modeling Turbulence-Induced Phase-Space Diffusion with Quadrature-Based Moment Methods

The vast majority of dispersed multiphase flows occurring in nature and technology are turbulent, which presents a particular challenge in terms of numerical modeling with QBMMs. Although the extent to which turbulence in the carrier fluid affects the exchange of momentum depends on specific flow characteristics, such as turbulence intensity and fluid-particle density ratio, it can be assumed that, in many cases, turbulent effects are not negligible. However, while the effects of turbulence on the breakup and coalescence of particles, i.e. phenomena that indirectly affect particle momentum, are a frequently addressed topic in the literature, e.g. [89–91] and [96, Sec. 5.8.4], reported research on the direct effects of turbulent fluctuations in the carrier phase on dispersed-phase momentum in the specific context of QBMMs is relatively scarce.

The choice of a suitable model for the effects of fluid-phase turbulence on dispersed particles depends primarily on whether particle velocity is an internal coordinate. As previously addressed in the discussion on the difference between the PBE and the GPBE in Section 2.1.2, the dispersed-phase velocity can be assumed to equal the fluid velocity at all times in low Stokes-number flows, i.e. $\mathrm{St} \ll 1$, where particle inertia can be neglected, whereas a higher Stokes number requires the particle velocity to be an internal coordinate. In case of the former, modeling turbulence effects on particles is straightforward as they follow directly from the fluid turbulence model and, provided that the turbulence model is based on an eddy viscosity, appear in the form of a physical diffusion

term in the PBE as in (2.10). This chapter focuses on the more difficult case where particle velocity is an internal coordinate and turbulent velocity fluctuations need to be considered in the momentum exchange between the fluid and particles, a problem that has not received much attention in the context of QBMMs. To the author's best knowledge, the only published approach explicitly suited to QBMMs is that proposed by Fox [48], involving a particle-phase turbulent kinetic energy and the solution of additional transport equations. There is, however, abundant literature on the mesoscopic description of turbulent dispersed multiphase flows where turbulent effects are represented by a diffusion term in velocity phase space [112, 113, 123, 135].

In this chapter, a macroscopic model for the effect of turbulent fluctuations is formulated starting from the microscopic behavior of a particle in a turbulent flow field. The equivalent mesoscale description takes the form of a Fokker-Planck equation with nonlinear and non-smooth terms. The corresponding integral terms in the derived moment equations pose a particular problem in terms of the numerical solution with QBMMs, which is the main focus of this chapter (instead of physically accurate turbulence modeling). Based on the mathematical properties of the investigated turbulence-induced terms, a variation of the QMOM using anti-Gaussian quadrature rules [86], the so-called Gauss/anti-Gauss QMOM, will be introduced and be revealed to significantly reduce the initially large errors in a series of one-dimensional test cases with analytical reference solutions. Moreover, a modified strong-stability preserving Runge-Kutta scheme for the temporal discretization of moment equations is provided that guarantees the unconditional preservation of moment realizability in the presence of phase-space diffusion.

5.1. Model Formulation

In what follows, the model equations governing the evolution of a spatially homogeneous particulate system dispersed in a turbulent fluid will be formulated, starting with the microscale description, i.e. the trajectory of a single particle denoted by $\boldsymbol{X}(t)$. Further, let the corresponding Lagrangian velocity be denoted by $\boldsymbol{V}(t)$ and, assuming that the fluid velocity is given in terms of the Eulerian

field $\boldsymbol{u}(\boldsymbol{x}, t)$, the Lagrangian fluid velocity by

$$\boldsymbol{U}(t) \coloneqq \boldsymbol{u}(\boldsymbol{X}(t), t). \tag{5.1}$$

The temporal dependencies of the Lagrangian variables will henceforth be omitted for brevity.

First, it is important to clarify the fundamental assumptions that form the basis of the model formulation below:

(i) Particles are considered to be non-deformable point particles with spherical shape.

(ii) The fluid properties are known from a numerical solution of some form of the Navier-Stokes equations (see Section 2.3) in conjunction with a turbulence model based on the velocity decomposition in (2.23) so that the Lagrangian fluid velocity can be written as

$$\boldsymbol{U} = \overline{\boldsymbol{U}} + \boldsymbol{U}', \tag{5.2}$$

where $\overline{\boldsymbol{U}}$ is the velocity resolved on the numerical grid and $\boldsymbol{U}'$ is the modeled turbulent contribution to the total fluid velocity. Moreover, the fluid properties are assumed to be constant during some observed time interval $[t, t + \Delta t]$. This includes thermophysical properties and the resolved fluid velocity $\overline{\boldsymbol{U}}$ as well as turbulence quantities resulting from the turbulence model such as the turbulent kinetic energy k_t, the characteristic turbulence length scale l_t and time scale τ_t.

(iii) The characteristic time scale corresponding to the unresolved turbulence structures is much smaller than the numerical step size and the characteristic particle time scale, i.e. $\tau_t \ll \Delta t$ and $\tau_t \ll \tau_p$, where τ_p is the characteristic particle time scale.

(iv) Fluid turbulence is isotropic.

Although the mentioned quantities are presumed to be known without further specification of the turbulence model, it is worth noting that LES (see Section 2.3) is consistent with the assumptions (ii)-(iv). In that case, $\overline{\boldsymbol{U}}$, $\boldsymbol{U}'$ and l_t denote the spatially filtered velocity, the modeled SGS velocity fluctuation and the filter width, respectively.

5.1.1. Microscale Model

The trajectory of a single particle obeys the equations of motion. Provided that momentum exchange is solely driven by drag forces due to a velocity difference between fluid and particle, they read

$$\mathrm{d}\boldsymbol{X} = \boldsymbol{V}\,\mathrm{d}t, \tag{5.3}$$

$$\mathrm{d}\boldsymbol{V} = \frac{(\boldsymbol{U}-\boldsymbol{V})}{\tau_p}\,\mathrm{d}t, \tag{5.4}$$

where the fraction on the RHS represents the particle acceleration. The response time τ_p is a characteristic time that elapses for the particle to adapt to the local fluid velocity. It results from Newton's second law of motion with a modeled drag force. In the case of spherical particles it is commonly expressed as

$$\tau_p = \frac{4}{3}\frac{\rho_p}{\rho_f}\frac{d}{C_d}|\boldsymbol{U}-\boldsymbol{V}|^{-1}, \tag{5.5}$$

where ρ_p, ρ_f and d denote the particle density, fluid density and particle diameter, respectively. C_d is the drag coefficient depending on the flow regime, which can be quantified in terms of the particle Reynolds number $\mathrm{Re_p}$ as defined in (4.9). At high $\mathrm{Re_p}$, C_d is commonly taken to be a constant, which is also presumed here. The decomposition in (5.2) then yields

$$\mathrm{d}\boldsymbol{V} = \frac{3}{4}\frac{\rho_f}{\rho_p}\frac{C_d}{d}|\bar{\boldsymbol{U}}+\boldsymbol{U}'-\boldsymbol{V}|(\bar{\boldsymbol{U}}+\boldsymbol{U}'-\boldsymbol{V})\,\mathrm{d}t. \tag{5.6}$$

Stochastic Lagrangian models, e.g. the eddy interaction model [61], make use of this equation to compute individual sample paths on the common supposition that in isotropic turbulence the components of $\boldsymbol{U}'$ are independent normally distributed random variables with zero mean and variance $2k_t/3$. Additionally, the time of interaction between particles and turbulent eddies is tracked to take into account the rate at which particles undergo fluctuations in the fluid velocity field, making the model non-Markovian and thus less suitable to derive mesoscale models, which typically rely only on the current state. Moreover, the eddy interaction model was designed for turbulence models based on the RANS equations, where the modeled velocity fluctuation $\boldsymbol{U}'$ would correspond to all scales of turbulence from the integral scale to the dissipation scale. Thus, the

particle-eddy interaction time might be considerably larger than the numerical step size, which contradicts assumption (iii).

A detailed general description in the mesoscopic sense would instead require $\boldsymbol{U}$ to be an internal coordinate. Minier and Peirano [113] refer to that velocity sampled along the particle trajectory as the fluid velocity "seen" and describe its temporal evolution with a stochastic differential equation (SDE) to account for the randomness of turbulent fluctuations. In simplified terms, it takes the form

$$\mathrm{d}\boldsymbol{U} = -\frac{\boldsymbol{U}}{\tau_f}\,\mathrm{d}t + \boldsymbol{\Phi}\,\mathrm{d}\boldsymbol{W}, \tag{5.7}$$

where τ_f denotes some time scale of the fluid velocity "seen", $\boldsymbol{\Phi} \in \mathbb{R}^3$ the noise coefficient matrix that may depend on internal coordinates and $\mathrm{d}\boldsymbol{W}$ an increment of a three-dimensional Wiener process. Minier and colleagues provide expressions for the coefficients in (5.7), considering even more detailed and complex physics, e.g. in [113, 135] and recently in [112].

Because of the problem of multivariate quadrature-based closures (see Section 3.5.3) that becomes more severe with increasing phase-space dimensionality, it is essential to reduce the number of internal coordinates to a minimum when using QBMMs. Thus, treating the fluid velocity $\boldsymbol{U}$ as an internal coordinate is rather undesired in this context. Instead, the particle velocity can be described in terms of a simplified model that takes the form of the (generally) nonlinear Langevin equation

$$\mathrm{d}\boldsymbol{V} = \boldsymbol{a}(\boldsymbol{V})\,\mathrm{d}t + \boldsymbol{\Sigma}(\boldsymbol{V}) * \mathrm{d}\boldsymbol{W}, \tag{5.8}$$

where $\boldsymbol{a} : \mathbb{R}^3 \to \mathbb{R}^3$ and $\boldsymbol{\Sigma} : \mathbb{R}^3 \to \mathbb{R}^{3\times3}$ denote the velocity-dependent drift and noise function, respectively. The operator $*$ specifies the interpretation of the SDE in terms of the stochastic integral, where the Itô integral is indicated by $* \,\mathrm{d}W \equiv \mathrm{d}W$ and the Stratonovich integral by $* \,\mathrm{d}W \equiv \circ\,\mathrm{d}W$. The first term on the RHS of (5.8) is deterministic and represents the particle acceleration by virtue of a mean drag force while the second term takes into account the randomness of $\boldsymbol{U}'$. Separating the resolved from the modeled part, the drift function becomes

$$\boldsymbol{a}(\boldsymbol{V}) = \frac{\overline{\boldsymbol{U}} - \boldsymbol{V}}{\tau_p}. \tag{5.9}$$

The noise term can be simplified, due to the assumption of isotropic turbulence, to $\boldsymbol{\Sigma}(\boldsymbol{V}) = \boldsymbol{I}\sigma(\boldsymbol{V})$, where $\boldsymbol{I}$ denotes the 3×3 identity matrix. Hence, the primary issue of the Langevin approach is to model the noise function $\sigma(\boldsymbol{V})$.

There are numerous studies proposing various more or less complex forms of the noise function. An example of a Langevin model based on detailed physical considerations is the LES-related model by Gorokhovski and Zamansky [60] that distinguishes between particles larger and smaller than the Kolmogorov length and introduces additional SDEs to describe the effects of turbulence fluctuations on particle trajectories. However, such models are almost always accompanied by stochastic particle methods, which practically allow for arbitrarily complex forms of the noise function. For the derivation of a macroscopic model combined with QBMMs, simplified models must be employed.

Minier and Peirano [113] describe ways to eliminate the fluid velocity "seen" in (5.7) from the internal coordinate vector in one spatial dimension. Considering the limits $\tau_f \to 0$ and $\langle U^2\rangle \to \infty$ such that $\tau_f\langle U^2\rangle = D$, they obtain $\sigma(V) = \tau_p^{-1}\sqrt{2D}$, though this result is based on constant τ_p. The considered limiting case $\tau_f \to 0$ requires the time scale of the fluid velocity τ_f to be very small compared to the particle time scale, which implies small-scale turbulence.

Bini and Jones [10] deduced from dimensional analysis that the noise coefficient should take the form

$$\sigma(\boldsymbol{V}) = C_t\sqrt{k_t\tau_{p,t}^{-1}(\boldsymbol{V})}, \tag{5.10}$$

where C_t is a model constant and $\tau_{p,t}$ is a characteristic turbulent particle time scale which was taken to be τ_p in (5.5) evaluated in terms of the resolved velocity $\overline{\boldsymbol{U}}$, say τ_p^*. This is consistent with the statement of Minier and Peirano [113] if $\tau_p = \tau_p^*$ and $2D = C_t^2 k_t \tau_p^*$. Bini and Jones extended the model by a nonlinearity parameter to fit experimental results. In a later LES-based study [9], they proposed the alternative form $\tau_{p,t} = \tau_{p,l}$ with

$$\tau_{p,l} = \frac{l_t}{|\boldsymbol{V}|}, \tag{5.11}$$

where l_t is the turbulence length scale resulting from the turbulence model (in LES the filter width). The time $\tau_{p,l}$ can be interpreted as the time of a particle with velocity $|\boldsymbol{V}|$ traversing a notional eddy. It is worth noting that this is in

agreement with the underlying ideas of the eddy-interaction model mentioned above.

One can argue that the model should account for both time scales, τ_p^* and $\tau_{p,l}$ in order to capture the effects of particle inertia as well as the interaction time with fluid turbulence. Then dimensional analysis yields

$$\sigma(\boldsymbol{V}) = C_t \sqrt{k_t (\tau_p^* \tau_{p,l})^{-1/2}}. \tag{5.12}$$

Here, the relationship in (5.10) with $\tau_{p,t} = \tau_p^*$ is deemed sufficient. It should be noted though, that, while it is certainly important in terms of physical accuracy, the choice of $\tau_{p,t}$ as τ_p^* or as in (5.12) is secondary for the numerical investigations in this chapter since in any case the particle acceleration depends on $\sqrt{|\boldsymbol{V}|}$.

Having determined expressions for the drift and noise function, the remaining question is whether to interpret the governing SDE (5.8) in the Itô sense or in the Stratonovich sense. While different interpretations can be found in the literature and the interpretation can be regarded merely as part of the model, here the common conception is adopted that the Itô integral is suitable for problems described by actual jump processes (e.g. financial markets) whereas the Stratonovich integral is appropriate for continuous physical problems in the macroscopic sense [53, 78]. As a further simplification, $\overline{\boldsymbol{U}} = 0$ will be presumed without loss of generality[1]. Additionally subsuming all constants in the drift and noise function into dimensional constants, the resulting microscale model can finally be expressed as

$$\mathrm{d}\boldsymbol{V} = \underbrace{-\gamma |\boldsymbol{V}| \boldsymbol{V}}_{\boldsymbol{a}(\boldsymbol{V})} \mathrm{d}t \; + \; \underbrace{\phi \sqrt{|\boldsymbol{V}|}}_{\sigma(\boldsymbol{V})} \circ \mathrm{d}\boldsymbol{W}, \tag{5.13}$$

where the dimensions are $[\gamma] = [\text{length}]^{-1}$ and $[\phi] = [\text{time}]^{-1}[\text{length}]^{1/2}$. Reduced to one dimension, the governing SDE can be written as

$$\mathrm{d}V = -\gamma \, \mathrm{sgn}(V) V^2 \, \mathrm{d}t \; + \; \phi \sqrt{|V|} \circ \mathrm{d}W. \tag{5.14}$$

[1] The moments associated with the particle velocity $\boldsymbol{V}$ can be converted into the moments associated with the mean relative velocity $\overline{\boldsymbol{U}} - \boldsymbol{V}$ (and vice versa) by the linear moment transformation in (3.46).

It should be noted that the one-dimensional model is nonphysical since turbulence is inherently three-dimensional. However, this reduction simplifies the development and evaluation of numerical methods, which is the focus of this work.

As a concluding remark it must be stressed once more that the considerations above resulting in (5.13) and (5.14) are limited to the case of small-scale turbulence. In other words, modeling the particle velocity as a Markov process is justified because many fluctuations act upon a particle during one integral time step, as stated by Bini and Jones [10].

5.1.2. Mesoscale Model

For the sake of simplicity, the mesoscopic description is limited to the three particle velocity components as internal coordinates, denoted by $\boldsymbol{v} = (v_1, v_2, v_3)^T$. It is well known that the evolution of the PDF describing the stochastic process in (5.13) is governed by a Fokker-Planck equation. As all particles of the population are identically distributed, it can simply be written for the NDF instead of the PDF due to (2.8) and the fact that the total number of particles remains constant. The Fokker-Planck equation results from a Kramers-Moyal expansion and reads for the given Stratonovich SDE [140]

$$\begin{aligned}\frac{\partial f(\boldsymbol{v};t)}{\partial t} &= -\frac{\partial}{\partial v_i}\left[a_i(\boldsymbol{v})f(\boldsymbol{v};t)\right] - \frac{\partial}{\partial v_i}\left[a_i^*(\boldsymbol{v})f(\boldsymbol{v};t)\right] \\ &\quad + \frac{1}{2}\frac{\partial^2}{\partial v_i^2}\left[\sigma^2(\boldsymbol{v})f(\boldsymbol{v};t)\right],\end{aligned} \tag{5.15}$$

where the function $a_i^*(\boldsymbol{v})$ represents an additional noise-induced drift that results from the Stratonovich integral and is given by

$$a_i^*(\boldsymbol{v}) = \frac{1}{2}\frac{\partial \sigma(\boldsymbol{v})}{\partial v_i}\sigma(\boldsymbol{v}). \tag{5.16}$$

Reduced to one dimension, the PBE can be written as

$$\begin{aligned}\frac{\partial f(v;t)}{\partial t} &= -\frac{\partial}{\partial v}\left[a(v)f(v;t)\right] - \frac{\partial}{\partial v}\left[a^*(v)f(v;t)\right] \\ &\quad + \frac{1}{2}\frac{\partial^2}{\partial v^2}\left[\sigma^2(v)f(v;t)\right].\end{aligned} \tag{5.17}$$

A Fokker-Planck equation of this form does not have a general analytical solution. However, there is an analytical expression for the steady-state NDF where the advective and diffusive fluxes are at an equilibrium. Setting the LHS in (5.17) to zero and substituting the explicit expressions for the drift and noise coefficients, see (5.13) and (5.14), yields the stationary NDF

$$f_{st}(v) = \frac{C}{\phi^2\sqrt{|v|}} \exp\left(-2\frac{\gamma}{\phi^2}|v|\right), \tag{5.18}$$

where C is a normalization constant such that $\int_{\mathbb{R}} f_{st}(v)\,\mathrm{d}v = m_0$. The derivation of the steady-state solution can be found in Appendix A.4.

5.1.3. Macroscale Model

It was demonstrated in Section 2.2 how a macroscopic model in terms of moment transport equations is derived from a PBE. For the multivariate moment $m_{ijk} = \langle v_1^i v_2^j v_3^k \rangle$, the moment transformation is applied to (5.15) and yields, after repeated integration by parts,

$$\begin{aligned}\frac{\mathrm{d}m_{ijk}(t)}{\mathrm{d}t} &= \iiint_{\mathbb{R}^3} \Big[i v_1^{i-1} v_2^j v_3^k a_1^{\Sigma}(\boldsymbol{v}) + j v_1^i v_2^{j-1} v_3^k a_2^{\Sigma}(\boldsymbol{v}) \\ &\qquad + k v_1^i v_2^j v_3^{k-1} a_3^{\Sigma}(\boldsymbol{v}) \Big] f(\boldsymbol{v};t)\,\mathrm{d}v_1\,\mathrm{d}v_2\,\mathrm{d}v_3 \\ &\quad + \frac{1}{2} \iiint_{\mathbb{R}^3} \Big[i(i-1) v_1^{i-2} v_2^j v_3^k + j(j-1) v_1^i v_2^{j-2} v_3^k \\ &\qquad + k(k-1) v_1^i v_2^j v_3^{k-2} \Big] \sigma^2(\boldsymbol{v}) f(\boldsymbol{v};t)\,\mathrm{d}v_1\,\mathrm{d}v_2\,\mathrm{d}v_3,\end{aligned} \tag{5.19}$$

where

$$a_i^{\Sigma}(\boldsymbol{v}) = a_i(\boldsymbol{v}) + a_i^*(\boldsymbol{v}), \quad i = 1, 2, 3. \tag{5.20}$$

The considerations in the following sections are primarily focused on the univariate form. For the moment of order k, it can be written as

$$\begin{aligned}\frac{\mathrm{d}m_k(t)}{\mathrm{d}t} &= k \int_{\mathbb{R}} v^{k-1} a(v) f(v;t)\,\mathrm{d}v + k \int_{\mathbb{R}} v^{k-1} a^*(v) f(v;t)\,\mathrm{d}v \\ &\quad + \frac{k(k-1)}{2} \int_{\mathbb{R}} v^{k-2} \sigma^2(v) f(v;t)\,\mathrm{d}v,\end{aligned} \tag{5.21}$$

and finally, substituting the general drift and noise functions with the explicit expressions derived in Section 5.1.1, as

$$\begin{aligned}\frac{\mathrm{d}m_k(t)}{\mathrm{d}t} &= -k\gamma \int_{\mathbb{R}} \operatorname{sgn}(v) v^{k+1} f(v;t)\,\mathrm{d}v + k\frac{\phi^2}{4}\int_{\mathbb{R}} \operatorname{sgn}(v) v^{k-1} f(v;t)\,\mathrm{d}v \\ &\quad + k(k-1)\frac{\phi^2}{2}\int_{\mathbb{R}} \operatorname{sgn}(v) v^{k-1} f(v;t)\,\mathrm{d}v.\end{aligned} \tag{5.22}$$

The problem of numerically solving the moment equations can be divided into two aspects: closure of the unclosed integral terms and discretization of the time derivative. Methods to approach both are presented in the next sections.

5.2. The Gauss/Anti-Gauss Quadrature Method of Moments

As pointed out above, the moment equations (5.22) derived from the PBE require a suitable method for closure, such as a QBMM. The application of QBMMs to Fokker-Planck equations and general PBEs with a diffusive flux in phase space can be found in several publications, e.g. [93, 119, 132], though with diffusivities that are constant or smooth functions. In such cases, Gaussian quadrature rules are known to yield accurate results. More precisely, the diffusion term is calculated exactly if $\sigma^2 \in \mathcal{P}_2$, as can be inferred from the generalized univariate moment equation (3.40) and the corresponding quadrature form (3.41). Moreover, high accuracy of the quadrature approximation can be expected if the diffusivity is a smooth function that is well approximated by a polynomial on the relevant interval. This condition is not satisfied by the governing equations derived above, which will be revealed to cause potentially large approximation errors.

As stated in Section 3.2, the error of an n-node Gaussian quadrature for the integral $\int_\Omega g(v) f(v)\,\mathrm{d}v$ vanishes, i.e. $R_n(g) = 0$, if $g \in \mathcal{P}_{2n-1}$. It is evident that this condition is not satisfied by any of the integrals in (5.22) since all integral terms can be expressed in the form $\int_{\mathbb{R}} \operatorname{sgn}(v) v^j f(v)\,\mathrm{d}v$ and $\operatorname{sgn}(v) v^j$ is not a

polynomial for any j. In quadrature form, (5.22) can be written as

$$\begin{aligned}\frac{\mathrm{d}m_k(t)}{\mathrm{d}t} &= -k\left[\gamma\sum_{j=1}^{n} w_j \operatorname{sgn}(v_j) v_j^{k+1} + R_n(v^{k-1}a)\right] \\ &+ k\left[\frac{\phi^2}{4}\sum_{j=1}^{n} w_j \operatorname{sgn}(v_j) v_j^{k-1} + R_n(v^{k-1}a^*)\right] \\ &+ \frac{k(k-1)}{2}\left[\phi^2\sum_{j=1}^{n} w_j \operatorname{sgn}(v_j) v_j^{k-1} + R_n(v^{k-2}\sigma^2)\right].\end{aligned} \tag{5.23}$$

Although none of the terms on the RHS satisfies the condition for exactness of the n-node Gaussian quadrature or can be considered smooth, there is a fundamental difference between the first term representing drift and the noise-induced terms. First, the advection term tends to an equilibrium at the origin, which prevents the error from growing indefinitely.[2] Second, the quadratic dependence corresponds to a fast error correction over time in that a positive error at time t leads to a negative error at time $t+\Delta t$ and vice versa. The noise-induced terms exhibit neither of these properties, allowing the error to grow over time. Thus, the quadrature errors $R_n(v^{k-1}a^*)$ and $R_n(v^{k-2}\sigma^2)$ can be deemed most critical with regard to the quality of the quadrature-based closure.

In order to estimate how the quadrature error behaves, it is sensible to approximate the sign function by a continuously differentiable function, e.g. the error function or the hyperbolic tangent. Because of the convenient properties of the error function in terms of its derivatives, the approximate sign function is defined as

$$\widetilde{\operatorname{sgn}}(v) := \operatorname{erf}(\lambda v), \tag{5.24}$$

where λ is a sufficiently large positive constant.[3] Using this approximation and omitting constants, both the noise-induced advection and the diffusion term in

[2] It is worth noting that the fragmentation of droplets discussed in Chapter 4 can be interpreted similarly in that the process under consideration shifts the distribution towards a regime where it no longer occurs.

[3] It follows directly from the definition of the error function $\operatorname{erf}(z) = 2/\sqrt{\pi}\int_0^z \exp(-x^2)\,\mathrm{d}x$ that $\lim_{\lambda\to\infty} \operatorname{erf}(\lambda v) = \operatorname{sgn}(v)$.

the kth moment equation can be written in the form

$$I(g_k) = \int_{\mathbb{R}} \underbrace{\tilde{\mathrm{sgn}}(v) v^{k-1}}_{g_k(v)} f(v)\,\mathrm{d}v. \tag{5.25}$$

Based on the polynomial series expansion of the error function [2, Eq. 7.1.5]

$$\tilde{\mathrm{sgn}}(v) = \mathrm{erf}(\lambda v) = \frac{2}{\pi}\sum_{i=0}^{\infty}(-1)^i \frac{\lambda^{2i+1}}{i!(2i+1)} v^{2i+1}, \tag{5.26}$$

g_k in (5.25) can be expressed as

$$g_k(v) = \frac{2}{\pi}\sum_{i=0}^{\infty}(-1)^i \frac{\lambda^{2i+1}}{i!(2i+1)} v^{2i+k}. \tag{5.27}$$

Then it follows from the degree of accuracy $2n-1$ that the Gaussian quadrature corresponding to (5.25) is exact for all terms with $i < n - k/2$. Thus, making use of the definition

$$C_i := \frac{2}{\pi}\frac{\lambda^{2i+1}}{i!(2i+1)}, \tag{5.28}$$

(5.27) can be rewritten for even k as

$$\begin{aligned} g_k(v) = \sum_{i=0}^{n-\frac{k}{2}} (-1)^i C_i\, v^{2(i-1)+k} \;+\; (-1)^n C_{n-k/2+1}(-1)^{1-k/2}\, v^{2n} \\ +\; O(v^{2n+2}), \end{aligned} \tag{5.29}$$

where the first term on the RHS represents the part that is integrated exactly by an n-node Gaussian quadrature. Evidently, the second term, i.e. the leading error term, changes its sign depending on whether the number of quadrature nodes n is even or odd. This is also true for moments of odd order.[4] This perspective, though not considered mathematical proof, suggests that the sign of the quadrature error in the moment equations is largely determined by the parity of n, which is supported by the numerical results in Section 5.4.

[4] For odd k, the upper limit of the sum and the expressions in the exponents change, but the factor $(-1)^n$ remains, regardless of the parity of k.

The considerations above give rise to the question whether some average of an n-node and an $(n-1)$-node quadrature is advantageous to achieve a more accurate approximation of (5.22). An obvious method to compute such a quadrature rule given the first $2n$ moments is to form the average of the $(n-1)$- and n-node Gaussian quadratures resulting from the first $2n-2$ and the first $2n$ moments, respectively. This approach is, however, not optimal since it decreases the formal order of accuracy to the lower-order representation, i.e. $2n-3$. In other words, such a type of quadrature would fail to exactly reproduce the underlying moment sequence. Instead, the so-called anti-Gaussian quadrature rules [86] are used to obtain an averaged $(2n-1)$-node quadrature preserving the original degree of accuracy.

It was shown by Laurie [86] that it is possible to compute an n-node quadrature, referred to as anti-Gaussian quadrature formula, with the same degree of accuracy as the corresponding $(n-1)$-node Gaussian quadrature, i.e. $2n-3$, and errors equal in magnitude but with opposite sign up to degree $2n-1$. Then the average of the Gaussian and the anti-Gaussian quadrature can be regarded as a $(2n-1)$-node quadrature rule with degree of accuracy $2n-1$, which is easily demonstrated considering an arbitrary $(2n-1)$th-degree polynomial with real coefficients, say p_{2n-1}. Then, indicating the abscissas, weights and errors of the Gaussian quadrature and the anti-Gaussian quadrature by the superscripts G and A, respectively, the integral I as defined in (3.15) can be written as

$$\begin{aligned} I(p_{2n-1}) = \frac{1}{2}\Bigg[& \sum_{j=1}^{n-1} w_j^G p_{2n-1}(v_j^G) \;+\; R_{n-1}^G(p_{2n-1}) \\ & + \sum_{j=1}^{n} w_j^A p_{2n-1}(v_j^A) \;+\; R_n^A(p_{2n-1}) \Bigg]. \end{aligned} \tag{5.30}$$

Both quadrature formulae are exact for polynomials up to degree $2n-3$. Moreover, by the definition of anti-Gaussian quadratures given above, the errors satisfy $R_{n-1}^G = -R_n^A$ for polynomials up to degree $2n-1$. Hence, the expression is exact and the combined $(2n-1)$-node quadrature has degree of accuracy $2n-1$.

A characteristic property of the anti-Gaussian quadrature nodes is that they are interlaced by those of the corresponding Gaussian quadrature nodes, i.e.

$$v_1^A < v_1^G < v_2^A < \cdots < v_{n-1}^G < v_n^A. \tag{5.31}$$

The calculation is straightforward: As demonstrated by Laurie [86], the n anti-Gaussian quadrature nodes are simply the roots of the polynomial

$$\pi_n^*(v) = (v - \alpha_{n-1})\pi_{n-1}(v) - 2\beta_{n-1}\pi_{n-2}(v), \tag{5.32}$$

cf. (3.7). Thus, the computation of the anti-Gaussian quadrature requires only knowledge of the recurrence coefficients of the polynomials orthogonal with respect to $f(v)$ with doubled coefficient β_{n-1}.

These relationships can be used to extend the standard QMOM to a $(2n-1)$-node approximation in order to mitigate the above-described dependence of the quadrature error on the choice of n. The procedure is as follows: With $2n$ known moments, the recurrence coefficients of the first n orthogonal polynomials are computed with an adequate algorithm (see Section 3.4). With available recurrence coefficients, a modified Jacobi matrix can be expressed as

$$\mathbf{J}_n^* = \begin{pmatrix} & \mathbf{J}_{n-1} & \begin{matrix} 0 \\ \sqrt{2\beta_{n-1}} \end{matrix} \\ 0 & \sqrt{2\beta_{n-1}} & \alpha_{n-1} \end{pmatrix}, \tag{5.33}$$

where $\mathbf{J}_{n-1}$ represents the ordinary truncated Jacobi matrix (see Section 3.1.2). Then the $n-1$ Gaussian quadrature nodes and weights result from the eigenvalues and eigenvectors of $\mathbf{J}_{n-1}$, respectively. Likewise, the n anti-Gaussian quadrature nodes and weights are computed from $\mathbf{J}_n^*$. Averaging both quadrature formulas as in (5.30), the resulting nodes and weights of the combined quadrature rule are

$$\begin{pmatrix} v_1 \\ v_2 \\ v_3 \\ \vdots \\ v_{2n-2} \\ v_{2n-1} \end{pmatrix} = \begin{pmatrix} v_1^A \\ v_1^G \\ v_2^A \\ \vdots \\ v_{n-1}^G \\ v_n^A \end{pmatrix} \quad \text{and} \quad \begin{pmatrix} w_1 \\ w_2 \\ w_3 \\ \vdots \\ w_{2n-2} \\ w_{2n-1} \end{pmatrix} = \frac{1}{2} \begin{pmatrix} w_1^A \\ w_1^G \\ w_2^A \\ \vdots \\ w_{n-1}^G \\ w_n^A \end{pmatrix}. \tag{5.34}$$

It should be noted that this method is specifically suited to Hamburger moment problems as the outer nodes $v_1 = v_1^A$ and $v_{2n-1} = v_n^A$ may be located

outside the interval of integration if it is bounded. This type of quadrature is here referred to as Gauss/anti-Gauss (GaG) quadrature and the modified QMOM accordingly as GaG-QMOM. Since the recurrence coefficients required for an n-node Gaussian quadrature and a $(2n-1)$-node GaG-quadrature are equal, the algorithm employed to compute them from a given set of moments, e.g. the Wheeler algorithm, is identical for the QMOM and the GaG-QMOM. The only computational overhead introduced by the proposed inversion algorithm involves the solution of the symmetric tridiagonal $(n-1)\times(n-1)$ eigenvalue problem for $\mathbf{J}_{n-1}$. Thus, the GaG-QMOM is expected to cause moderate computational costs in comparison with the standard QMOM, see also Appendix A.6.

Finally, the $(2n-1)$-point GaG-quadrature rule is applied to (5.22) to obtain

$$\begin{aligned}\frac{\mathrm{d}m_k(t)}{\mathrm{d}t} \approx & -k\gamma\sum_{j=1}^{2n-1} w_j \mathrm{sgn}(v_j) v_j^{k+1} + k\frac{\phi^2}{4}\sum_{j=1}^{2n-1} w_j \mathrm{sgn}(v_j) v_j^{k-1} \\ & + k(k-1)\frac{\phi^2}{2}\sum_{j=1}^{2n-1} w_j \mathrm{sgn}(v_j) v_j^{k-1}.\end{aligned} \tag{5.35}$$

It should be highlighted that the method described here is not limited to phase-space diffusion. Instead, it can be applied to problems involving nonlinear or even discontinuous integral terms with respect to an unbounded internal coordinate, serving as an alternative inversion algorithm that

- requires no additional assumptions,
- maintains the maximal formal degree of accuracy,
- potentially reduces the approximation error for strongly nonlinear or discontinuous problems,
- has moderate computational overhead (see Appendix A.6).

5.3. A Method of Realizability-Preserving Temporal Discretization

With a closed form of the moment equations, the remaining question is how to discretize the temporal derivative in (5.35). It was highlighted in Section 3.3

that moment realizability is a critical issue that must be taken into account in the choice of numerical methods when solving moment equations. A common restriction on the numerical scheme in conjunction with QBMMs is that the discretization should be explicit. There are, however, further limitations entailed by the realizability problem, which will be discussed in the course of this section.

The most straightforward explicit method of numerical integration is the explicit Euler method. Given a valid sequence of $2n$ moments at time t_i, denoted by $\boldsymbol{m}^i_{2n-1}$, a single integration step from t_i to $t_{i+1} = t_i + \Delta t$ with the explicit Euler scheme is given by

$$m_k^{i+1} = m_k^i + \Delta t \; \dot{m}_k(\boldsymbol{m}^i_{2n-1}), \tag{5.36}$$

where the function $\dot{m}_k$ represents the complete algorithm to calculate $\mathrm{d}m_k/\mathrm{d}t$, including the moment inversion and the evaluation of the RHS of (5.35). The Euler scheme is only first-order accurate in time and thus requires a very small step size Δt to achieve adequate accuracy. A suitable family of higher-order schemes to approximate a solution to the closed moment equations (5.35) are the strong stability preserving Runge-Kutta (RKSSP) methods due to Shu and Osher [149]. RKSSP schemes, particularly the second-order accurate two-stage scheme RK2SSP, were shown to preserve moment realizability when applying QBMMs to inhomogeneous systems where physical space advection may become a severe problem in terms of realizability [167]. One step of the RK2SSP scheme can be written as

$$m_k^* = m_k^i + \Delta t \; \dot{m}_k(\boldsymbol{m}^i_{2n-1}), \tag{5.37}$$

$$m_k^{**} = m_k^* + \Delta t \; \dot{m}_k(\boldsymbol{m}^*_{2n-1}), \tag{5.38}$$

$$m_k^{i+1} = \frac{1}{2}\left(m_k^i + m_k^{**}\right), \tag{5.39}$$

where $k = 0, 1, \ldots, 2n-1$. The RK2SSP scheme comprises two consecutive Euler steps yielding the intermediate moments $\boldsymbol{m}^{**}_{2n-1}$ and finally a weighted average to compute the moment sequence at time t_{i+1}. It is guaranteed to yield valid moments $\boldsymbol{m}^{i+1}_{2n-1}$ if $\boldsymbol{m}^{**}_{2n-1}$ is realizable, for the sum of realizable moment sequences yields, again, a realizable moment sequence. In other words, a numerical method that is guaranteed to preserve moment realizability in a single

step of the explicit Euler scheme is easily transferable to higher-order RKSSP methods.

In spatially homogeneous systems, realizability issues may occur in two situations. First, the step size Δt is too large. The resulting realizability problem is illustrated well by the example of the moment equation (5.22) in discretized general quadrature form with zero diffusivity, i.e.

$$m_k^{i+1} \approx m_k^i - \Delta t \; k\gamma \sum_j w_j \mathrm{sgn}(v) v^{k+1}. \tag{5.40}$$

Evidently, even if the quadrature approximation is exact, a large Δt may result in negative moments of even order, which corresponds to an unrealizable moment set. One way to ensure moment realizability in the presence of advection in physical space is to limit the step size based on a realizability criterion as suggested in [115, 167]. This is necessary in spatially inhomogeneous systems where numerical schemes are typically constrained by a fixed step size in physical space. In homogeneous systems this limitation is avoidable, as will be demonstrated further below.

The second situation that is critical in terms of moment realizability is that the initial moment sequence is weakly realizable, i.e. $\boldsymbol{m}_{2n-1}^i \in \partial \mathcal{M}_{2n-1}$. As a result, even a very small error induced by the temporal discretization with nonlinear $\dot{m}_k$ may lead to a sequence $\boldsymbol{m}_{2n-1}^{i+1} \notin \mathcal{M}_{2n-1}$. In that case, correction algorithms are needed to generate a realizable moment set close to the original one.

Although both of the described situations should be rare and could be handled with a restriction on Δt and methods for moment correction, the application of a numerical scheme that prevents moment corruption regardless of the step size and given moment sequence is generally preferable. In order to achieve that, the governing moment equations are not solved directly. Instead, the solution of the governing microscale equation, in this case the Itô SDE corresponding to the Fokker-Planck equation, is approximated at each quadrature node on the interval $[t_i, t_{i+1}]$, and the moment sequence $\boldsymbol{m}_{2n-1}^{i+1}$ is subsequently reconstructed with the modified quadrature. The Itô SDE corresponding to (5.17) reads

$$\mathrm{d}V = \left[a(V) + a^*(V)\right] \mathrm{d}t + \sigma(V) \, \mathrm{d}W. \tag{5.41}$$

An approximate solution to this SDE on the interval $[t_i, t_{i+1}]$ is obtained by first considering the deterministic contribution to compute a modified set of

quadrature nodes and subsequently approximating a solution to the stochastic part. That is, without further specification of the moment inversion method and the according number of nodes, advection on the interval $[t_i, t_{i+1}]$ yields the modified jth quadrature node

$$\hat{v}_j^i = v_j^i + \left[a(v_j^i) + a^*(v_j^i)\right] \Delta t. \tag{5.42}$$

The weights remain unchanged, i.e. $\hat{w}_j^i = w_j^i$. As for the diffusion term, it is well known that the solution to

$$\mathrm{d}V = \sigma \, \mathrm{d}W \tag{5.43}$$

with constant σ and zero variance at time $t = 0$ is a Gaussian with variance $\sigma^2 t$ [53]. Thus, denoting a normal distribution with mean μ and variance s^2 by $\mathcal{N}(\mu, s)$ and the associated kth moment by

$$\tilde{m}_k(\mu, s) = \langle Y^k \rangle, \quad Y \sim \mathcal{N}(\mu, s), \tag{5.44}$$

the application to each modified quadrature node yields, presuming constant $\sigma = \sigma(v_j^i)$ on the interval $[t_i, t_{i+1}]$, the approximate moments at time t_{i+1}:

$$m_k^{i+1} = \sum_j \hat{w}_j^i \tilde{m}_k \left(\hat{v}_j^i, \ \sigma(v_j^i)\sqrt{\Delta t}\right). \tag{5.45}$$

Since the RHS is a positively weighted sum of realizable moments (the moments of a normal distribution) realizability is ensured regardless of Δt. It is important to note that the assumption of constant σ is consistent with the Itô interpretation of the governing SDE instead of the Stratonovich interpretation.

The approach described above is, albeit less complex, inspired by the phase-space advection scheme for evaporating droplets by Massot et al. [101] in that the governing microscale equations are used to approximate the macroscale solution. The equations (5.42), (5.44) and (5.45) can be thought of as a modification of the explicit Euler method to ensure preservation of moment realizability. The method is hence first-order accurate in time. However, the extension to a second-order RKSSP method is straightforward: Instead of computing the moments $\boldsymbol{m}_{2n-1}^{i+1}$ directly, (5.45) is used to calculate the intermediate moments $\boldsymbol{m}_{2n-1}^{*}$. Following another moment inversion, the same procedure can then be

applied to obtain $\boldsymbol{m}^{**}_{2n-1}$. Denoting the number of quadrature nodes by n', where $n' = n$ for the standard QMOM or $n' = 2n-1$ for the GaG-QMOM, the realizable RK2SSP algorithm can be summarized as follows:

1. Invert moments at time t_i

$$\boldsymbol{m}^{i}_{2n-1} \rightarrow w^i_j, v^i_j, \quad j = 1, 2, \ldots, n'$$

2. Compute modified quadrature due to advection

$$\hat{v}^i_j = v^i_j + \left[a(v^i_j) + a^*(v^i_j)\right]\Delta t, \quad \hat{w}^i_j = w^i_j$$

3. Compute first-stage intermediate moments considering diffusion

$$m^*_k = \sum_{j=1}^{n'} \hat{w}^i_j \tilde{m}_k\left(\hat{v}^i_j,\ \sigma(v^i_j)\sqrt{\Delta t}\right), \quad k = 0, 1, \ldots, 2n-1$$

4. Invert intermediate moments

$$\boldsymbol{m}^{*}_{2n-1} \rightarrow w^*_j, v^*_j, \quad j = 1, 2, \ldots, n'$$

5. Compute modified quadrature due to advection

$$\hat{v}^*_j = v^*_j + \left[a(v^*_j) + a^*(v^*_j)\right]\Delta t, \quad \hat{w}^*_j = w^*_j$$

6. Compute second-stage intermediate moments considering diffusion

$$m^{**}_k = \sum_{j=1}^{n'} \hat{w}^*_j \tilde{m}_k\left(\hat{v}^*_j,\ \sigma(v^*_j)\sqrt{\Delta t}\right), \quad k = 0, 1, \ldots, 2n-1$$

7. Form average to obtain moments at time t_{i+1}

$$\boldsymbol{m}^{i+1}_{2n-1} = \frac{1}{2}\left(\boldsymbol{m}^{i}_{2n-1} + \boldsymbol{m}^{**}_{2n-1}\right).$$

During the entire procedure moments are computed only as a result of positive weights and valid quadrature nodes, that is $v_j \in \mathbb{R}\ \forall\ j = 1, 2, \ldots, n'$. Corruption of the initial moment set is thus impossible, regardless of Δt. Therefore,

the presented numerical scheme will be referred to as the absolutely realizable RK2SSP scheme (RK2SSP-AR) in the following sections. The extension to the three-stage third-order RKSSP scheme [149] is straightforward. Further, it can be easily transferred to multivariate problems, provided that a suitable multivariate quadrature is available. Additionally, the step size Δt can be controlled if needed, using either a higher-order approximation as an error estimate, e.g. by means of an efficient embedded scheme as proposed in [115] or step size doubling based on Richardson extrapolation, see e.g. [67, Ch. 2, Sec. 4]. The latter is employed for some of the numerical investigations in the following section.

5.4. Numerical Tests

In this section, the numerical methods introduced above are applied to three different one-dimensional test cases with analytical reference solutions. After a brief summary of the considered general configuration in Section 5.4.1, each test case will be detailed in terms of the governing equations and initial conditions, analytical reference solutions and finally the numerical results in Sections 5.4.2–5.4.4. All numerical tests were performed using a Python implementation developed as part of this work, see Appendix A.1 for additional details.

5.4.1. Summary of Test Cases

Three test cases were considered with different combinations of physical phenomena and initial conditions. More precisely, the numerical investigations include pure Itô diffusion (Case 1), Stratonovich diffusion (Case 2) and the steady-state Fokker-Planck equation (Case 3). The mesoscopic description of all cases can be expressed in the form of the one-dimensional Fokker-Planck equation (5.17) with different advection coefficients $a(v)$ (drift-induced), $a^*(v)$ (noise-induced) and diffusivities $\sigma^2(v)$, which are summarized in Table 5.1. Further details are provided in the respective subsections.

Considering that the choice of constants does not matter with regard to the relative errors, all investigations were carried out with fixed constants γ and ϕ. With the commonly used drag coefficient $C_d = 0.44$, the model constant $C_t = 1$ and estimated values of $d \sim 10^{-5}$ m (particle diameter), $\rho_p/\rho_f \sim 10^2$ (density

Table 5.1.: Summary of test cases with the advection and diffusion coefficients corresponding to the Fokker-Planck equation (5.17).

Case	$a(v)$	$a^*(v)$	$\sigma^2(v)$
1	0	0	$\phi^2\|v\|$
2	0	$\frac{\phi^2}{4}\mathrm{sgn}(v)$	$\phi^2\|v\|$
3	$-\gamma\|v\|\,v$	$\frac{\phi^2}{4}\mathrm{sgn}(v)$	$\phi^2\|v\|$

ratio) and $k_t \sim 1\ \mathrm{m^2 s^{-2}}$ (turbulent kinetic energy), the chosen constants are

$$\gamma = 330\ \mathrm{m^{-1}}, \quad \phi = 16\ \frac{\sqrt{\mathrm{m}}}{\mathrm{s}}.$$

The fluid state is assumed to be constant over the entire observed time interval. Thus, the zeroth moment, which corresponds to the total number of particles[5], is mathematically merely a scaling factor without any particular importance. For simplicity, it is set to $m_0 = 1$.

In all test cases, both the standard QMOM and the GaG-QMOM were applied to close the governing moment equations. Additionally, the EQMOM with Gaussian KDFs (using the algorithm proposed by Pigou et al. [126] for the extended moment inversion) was tested in some cases. Since the number of quadrature nodes differs depending on the used closure, the specific methods are primarily characterized by the number of transported moments, which should serve as a basis for comparison. Thus, the respective QBMMs are indicated first by the general type of moment inversion, second by the number of transported moments and finally by the number of nodes in parentheses, which is merely a result of the former two. For example, in the case of eight transported moments, the four-node QMOM will be referred to as QMOM8(4) and the seven-node GaG-QMOM as GaG-QMOM8(7). Configurations using the EQMOM are additionally characterized by the number of second quadrature nodes, e.g. EQMOM7(3/20) to refer to the EQMOM using seven moments, i.e. three first quadrature nodes,

[5]Normally, the zeroth moment represents the number of particles per unit volume. In spatially homogenous systems, however, it may as well be defined as the total number of particles, since the physical control volume is arbitrary.

and 20 second quadrature nodes.

As for the temporal discretization, the RK2SSP as well as the RK2SSP-AR scheme were used to approximate solutions to the moment equations in all cases where moment realizability is not an issue, which excludes Case 2 as will be explained in Section 5.4.3. In Case 3 these numerical schemes were also combined with an adaptive step size control based on Richardson extrapolation and step doubling [67].

5.4.2. Case 1: Itô Diffusion

The first studied test case is one-dimensional Itô diffusion. The numerical solution of pure diffusion problems on an unbounded domain is inherently unstable for the error can grow indefinitely with the solution. Hence, this problem can serve only as a basis for comparison of numerical methods among one another rather than a quantitative error analysis. Moreover, a fixed step size must be used for numerical integration in time as the use of an adaptive step size that is controlled by an allowed error would inevitably result in $\Delta t \to 0$. The step size is therefore set to $\Delta t = 10^{-6}$ s.

Governing equations and initial conditions

The microscopic description of Itô diffusion is given by the SDE

$$\mathrm{d}V = \sigma(V)\,\mathrm{d}W. \tag{5.46}$$

With the diffusivity given in Table 5.1, this corresponds to the mesoscopic description

$$\frac{\partial f(v;t)}{\partial t} = \frac{\phi^2}{2}\frac{\partial^2}{\partial v^2}\left[|v|\, f(v;t)\right], \tag{5.47}$$

and the derived moment equation for order k reads

$$\frac{\mathrm{d}m_k(t)}{\mathrm{d}t} = k(k-1)\frac{\phi^2}{2}\int_{\mathbb{R}} v^{k-2}|v|\, f(v;t)\,\mathrm{d}v. \tag{5.48}$$

Initially, particle velocities are normally distributed with mean $\mu = 0$ and standard deviation $s = 1$ m/s. Using the notation for normal moments in Sec-

tion 5.3, the initial moments can thus be expressed as [42]

$$m_k(0) = \tilde{m}_k(0,1) = \begin{cases} \dfrac{k!}{2^{k/2}(k/2)!} & \text{if } k \text{ is even,} \\ 0 & \text{otherwise.} \end{cases} \tag{5.49}$$

Analytical reference solution

The symmetry about the origin allows for an analytical expression for the temporal evolution of moments, making use of the absolute moments

$$M_k = \int_{\mathbb{R}} |v|^k \, f(v) \, \mathrm{d}v. \tag{5.50}$$

Application of this definition to the PBE (5.47) and repeated integration by parts yields the ODE for the kth absolute moment

$$\frac{\mathrm{d}M_k(t)}{\mathrm{d}t} = k(k-1)\frac{\phi^2}{2} \underbrace{\int_{\mathbb{R}} |v|^{k-1} \, f(v;t) \, \mathrm{d}v}_{M_{k-1}(t)}. \tag{5.51}$$

Since only absolute moments of lower order appear on the RHS, the system of ODEs for $k = 1, 2, \ldots$ can be solved recursively for $M_1, M_2, \ldots$ with given initial conditions $M_k(0)$. Then the solution for the absolute moments can be expressed as

$$M_k(t) = \sum_{j=1}^{k} \binom{k}{j} \frac{(k-1)!}{(j-1)!} M_j(0) \left(\frac{\phi^2}{2} t\right)^{(k-j)}. \tag{5.52}$$

In the general case, the ordinary moments cannot be expressed directly in terms of the absolute moments. However, for a NDF that is initially symmetric, i.e. $m_{2k+1}(0) = 0$, it follows from the symmetric properties of the integral terms that $\mathrm{d}m_{2k+1}/\mathrm{d}t = 0$. Moreover, the ordinary moments of even order equal the absolute moments ($m_{2k} = M_{2k}$) for $v \in \mathbb{R}$. That is, the moments for Itô diffusion with symmetric $f(v;0)$ are

$$m_k^{\text{analyt}}(t) = \begin{cases} \displaystyle\sum_{j=1}^{k} \binom{k}{j} \frac{(k-1)!}{(j-1)!} M_j(0) \left(\frac{\phi^2}{2} t\right)^{(k-j)} & \text{if } k \text{ is even,} \\ 0 & \text{otherwise.} \end{cases} \tag{5.53}$$

Thus, in order to calculate the analytical solution one must provide the initial absolute moments, that is, in the case of zero mean, the central absolute moments of the normal distribution, which can be found in Appendix A.3. It is worth noting that the expression (5.53) corresponds to a linear growth in the second moment, which represents the variance and is proportional to kinetic energy.

Results

The results of the standard QMOM with up to seven quadrature nodes in terms of the second and fourth moment are illustrated in Figure 5.1. As problems related to moment realizability did not occur with the selected step size and initial distribution, the RK2SSP was used first in order to rule out any possible undesired effects that may result from the indirect approximation of moments by the RK2SSP-AR scheme. It is immediately apparent that the deviation of the second moment from the exact solution is significantly larger than that of the fourth moment. As discussed in Section 5.2 and indicated by (5.29), the sign of the errors is determined by the parity of the number of Gauss quadrature nodes n. For the second moment, an odd n results in negative errors corresponding to an underestimation, whereas the second moment is overestimated when choosing an even n. The fourth moment displays a similar behavior, albeit reversed. That is, errors in the fourth moment are positive if n is odd and negative if n is even. This behavior is also suggested by the factor $(-1)^{1-k/2}$ in the leading error term in (5.29).

Figure 5.2 shows the second moment and its relative error using the QMOM and GaG-QMOM with up to ten moments. The system of ODEs was again solved with the RK2SSP scheme to enable a comparison of the used QBMMs unaffected by the alterations made to preserve realizability. The averaging procedure of the GaG-QMOM appears to have the desired effect that the dependence of the error on the parity of n is eliminated to a large extent. Generally, the results in terms of the second moment reveal a considerable increase in accuracy of the GaG-QMOM compared to the QMOM, even with a lower-order quadrature. This is also true for the fourth moment, which is shown in Figure 5.3. While all applied methods display a smaller approximation error in the fourth moment than in the

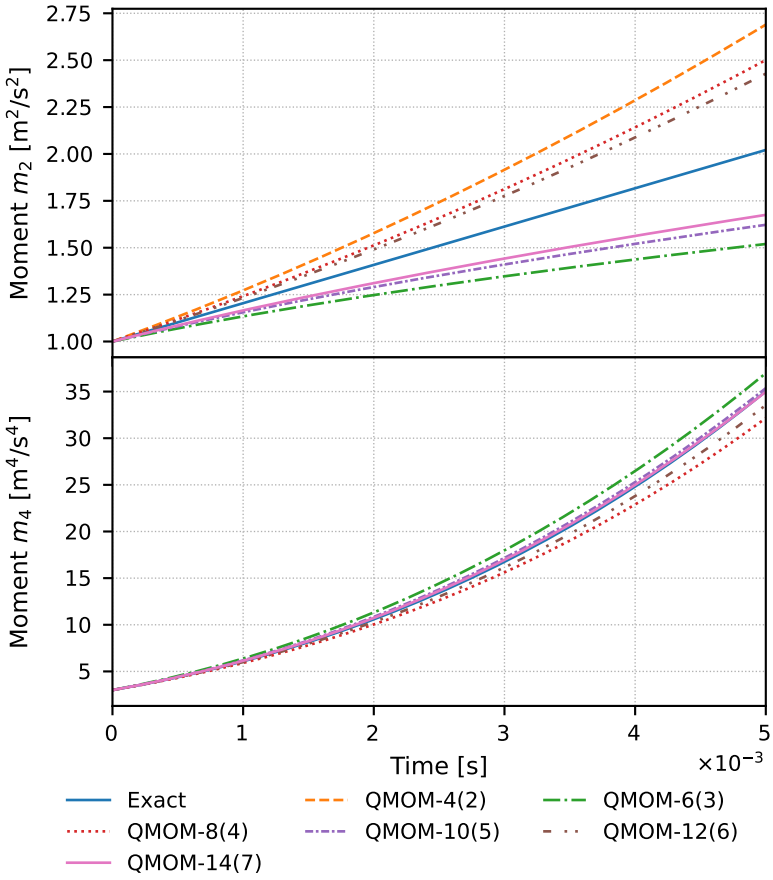

Figure 5.1.: Temporal evolution of the second (top) and fourth moment (bottom) for Case 1 (Itô diffusion) using the standard QMOM and the RK2SSP scheme.

second moment, the GaG-QMOM is significantly more accurate over a relatively long period of time.

Given the form of the integrals, it is natural to assume that significant improvement might be achieved by the application of the EQMOM with its possibility to generate an arbitrary number of moment-preserving samples in the

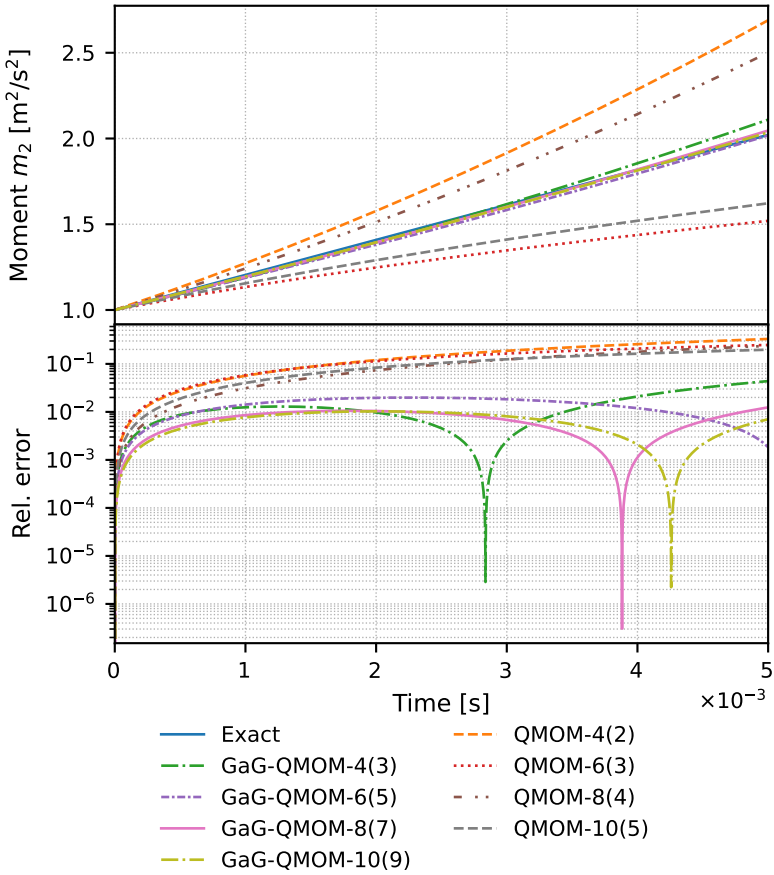

Figure 5.2.: Temporal evolution of the second moment (top) and the relative error (bottom) for Case 1 (Itô diffusion), using both the QMOM and the GaG-QMOM with the RK2SSP scheme.

form of second quadrature nodes (see Section 3.5.2). To this end, the EQMOM was also tested in addition to the QMOM and the GaG-QMOM, though limited to Gaussian KDFs since the second type suited to unbounded internal coordinates, the Laplace-EQMOM, suffers from the lack of a transformation to a weight function of orthogonal polynomials with known recurrence coefficients. As a

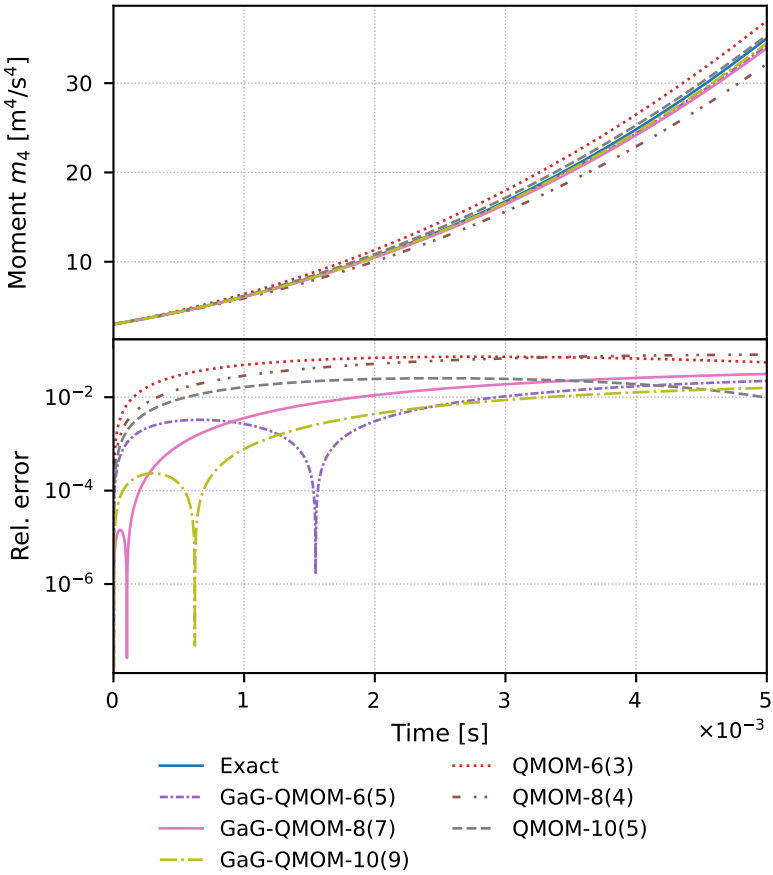

Figure 5.3.: Temporal evolution of the fourth moment (top) and the relative error (bottom) for Case 1 (Itô diffusion), using both the QMOM and the GaG-QMOM with the RK2SSP scheme.

result, the calculation of the second quadrature requires additional moment inversions that are, in case of a larger number of nodes, ill-conditioned. First, an appropriate number of second quadrature nodes n_{12} was estimated by varying n_{12} within a relatively wide range of values and observing the error at a fixed point in time, here $t = 5 \cdot 10^{-3}$ s. The result shown in Figure 5.4 sug-

gests that for $n_{12} \geq 100$ no stronger dependence on n_{12} can be expected, hence $n_{12} = 100$ was chosen for tests involving the EQMOM. Furthermore, Figure 5.4 reveals that configurations corresponding to an even number of first quadrature nodes yield results that are virtually identical to those of the respective lower-order approximation with an odd number of nodes. The reason is that the root finding algorithm for the KDF-parameter failed to find an extended quadrature for this specific setup and reduced the number of KDFs. Figure 5.5 compares the Gaussian-EQMOM to the GaG-QMOM with respect to the second moment. The initially high accuracy of the EQMOM decreases with time so that the approximation errors quickly exceed those of the GaG-QMOM. The explanation for the accurate results in the beginning is obvious, considering the chosen normal KDFs in combination with the normal distribution as initial condition. In other words, the Gaussian-EQMOM is exact at $t = 0$. However, as the solution deviates from the assumption of the Gaussian shape, large errors can be observed. Thus, it can be concluded that the EQMOM is not a suitable alternative to the GaG-QMOM in this case.

Figure 5.6 shows the relative errors in terms of the second moment at time $t = 5 \cdot 10^{-3}$ s using the QMOM and GaG-QMOM with up to 20 moments and both

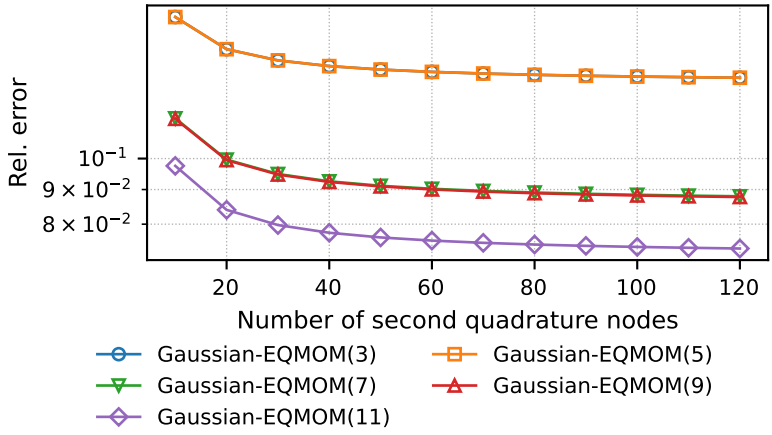

Figure 5.4.: Dependence of the error at $t = 5 \cdot 10^{-3}$ s on the number of second quadrature nodes using the EQMOM for Case 1 (Itô diffusion).

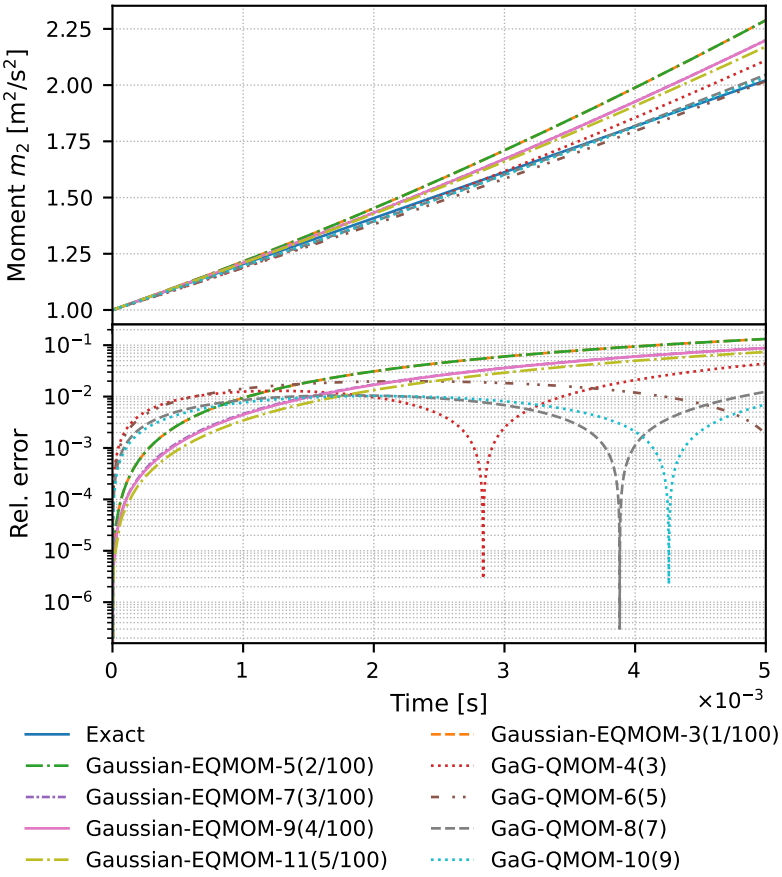

Figure 5.5.: Comparison of the GaG-QMOM and EQMOM in terms of the second moment (top) and the relative error (bottom) for Case 1 (Itô diffusion) using the RK2SSP scheme.

the RK2SSP and the RK2SSP-AR scheme. Besides the observation that the results do not display the expected correlation between the error and the number of quadrature nodes, it is evident that the GaG-QMOM gives significantly better approximations in all cases (it was already mentioned above that this case can only serve for a comparison of methods instead of a quantitative error analysis).

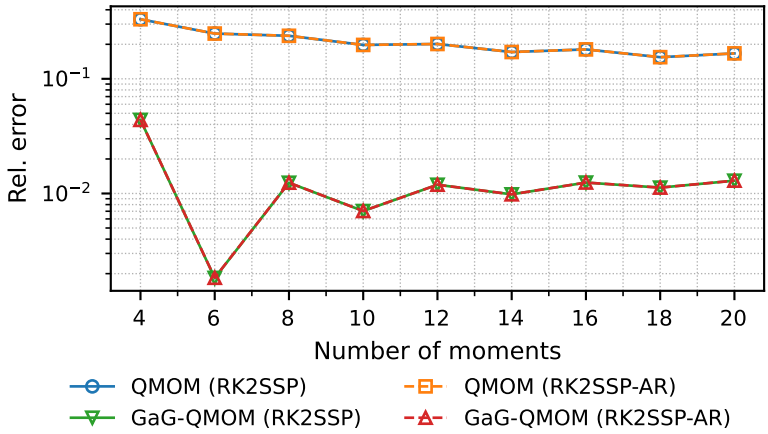

Figure 5.6.: Relative errors in the second-order moment at time $t = 5 \cdot 10^{-3}$ s using QBMMs with up to 20 moments and the RK2SSP and RK2SSP-AR scheme for Case 1 (Itô diffusion).

Moreover, the results using the RK2SSP-AR scheme are almost identical to those of the standard RK2SSP scheme, which indicates that the RK2SSP-AR scheme is a suitable realizability-preserving alternative to the standard method.

In conclusion, the first test case proved that the error due to the quadrature-based approximation of the turbulence-induced diffusion term in the absence of advection behaves as suggested by the theoretical considerations in Section 5.2. It can be reduced significantly by the application of a GaG-quadrature instead of the ordinary Gaussian quadrature, while the extended quadrature from the EQ-MOM did not prove to be an appropriate alternative for the investigated problem. Furthermore, both numerical schemes, the RK2SSP and the RK2SSP-AR, yield almost identical results in this particular case, where moment realizability is not critical.

5.4.3. Case 2: Stratonovich Diffusion

The second test case is concerned with one-dimensional Stratonovich diffusion and weakly realizable initial moments. As outlined in Section 5.3, moment realizability is then critical. In fact, several computations involving the standard

RK2SSP scheme failed due to realizability issues, more precisely, negative recurrence coefficients β_k were encountered for $k > 2$, resulting in failure of the moment inversion procedure. Thus, only the RK2SSP-AR scheme, which preserved realizability as expected, was used for the results shown below. The step size was again fixed at $\Delta t = 10^{-6}$ s for the same reasons discussed in the previous section.

Governing equations and initial conditions

The SDE describing Stratonovich diffusion is

$$\mathrm{d}V = \sigma(V) \circ \mathrm{d}W. \tag{5.54}$$

The Fokker-Planck equation is characterized by an additional noise-induced advection term as a result of the interpretation of the stochastic integral in the Stratonovich sense. With the coefficients in Table 5.1, it reads

$$\frac{\partial f(v;t)}{\partial t} = -\frac{\phi^2}{4}\frac{\partial}{\partial v}\left[\mathrm{sgn}(v) f(v;t)\right] + \frac{\phi^2}{2}\frac{\partial^2}{\partial v^2}\left[|v| f(v;t)\right], \tag{5.55}$$

finally resulting in the moment equations

$$\begin{aligned}\frac{\mathrm{d}m_k(t)}{\mathrm{d}t} &= k\frac{\phi^2}{4}\int_{\mathbb{R}} v^{k-1}\mathrm{sgn}(v) f(v;t)\,\mathrm{d}v \\ &\quad + k(k-1)\frac{\phi^2}{2}\int_{\mathbb{R}} v^{k-2}|v| f(v;t)\,\mathrm{d}v.\end{aligned} \tag{5.56}$$

The initial condition in this case is the two-point distribution with $v = \pm 1$ m/s and equal weights

$$f(v;0) = \frac{1}{2}\left[\delta(v - v_1) + \delta(v - v_2)\right], \quad v_1 = -v_2 = -1 \tag{5.57}$$

with the moments

$$m_k(0) = \begin{cases} 1 & \text{if } k \text{ is even,} \\ 0 & \text{otherwise.} \end{cases} \tag{5.58}$$

The peculiarity of this configuration is that the initial NDF is uniquely determined by the first four moments. In other words, the moments are on the moment space boundary, $\boldsymbol{m}_{2n-1} \in \partial\mathcal{M}_{2n-1}\ \forall\ n > 2$.

Analytical reference solution

Analogously to (5.51), a system of ODEs can be written for the absolute moments as

$$\frac{\mathrm{d}M_k(t)}{\mathrm{d}t} = \left[k\frac{\phi^2}{4} + k(k-1)\frac{\phi^2}{2}\right] M_{k-1}(t) \tag{5.59}$$

with the exact solution

$$m_k^{\text{analyt}}(t) = \begin{cases} \displaystyle\sum_{j=1}^{k}\left(\prod_{i=j+1}^{k}\frac{i}{2}\frac{2i-1}{i-j}\right) M_j(0)\left(\frac{\phi^2}{2}t\right)^{(k-j)} & \text{if } k \text{ is even,} \\ 0 & \text{otherwise,} \end{cases} \tag{5.60}$$

where the initial condition follows from (5.57):

$$M_k(0) = 1, \quad k = 0, 1, \ldots. \tag{5.61}$$

In contrast to Itô diffusion, the noise-induced advection term, which does not vanish for the first absolute moment, causes a quadratic increase in the second moment.

Results

Figure 5.7 shows the second moment and its relative error with up to ten transported moments. Initially, the approximation by means of the standard QMOM is more accurate than that by the GaG-QMOM. This behavior is expected due to the different properties of the underlying quadrature forms: It was emphasized in Section 3.5.1 that the n-node Gaussian quadrature is exact if the weight function represents an n-point distribution, which is the case here. The GaG-quadrature, however, does not have this property. While the $(n-1)$-node Gaussian quadrature used for averaging is clearly exact for $(n-1)$-point distributions, the n-node anti-Gaussian quadrature is not. This implies that the standard QMOM may be the preferable choice in cases where the moments are located on or close to the boundary of the moment space. However, this case is uncommon and in the presence of a diffusive flux term the discussed effect fades over time as the moments diverge from this specific initial state and display the same

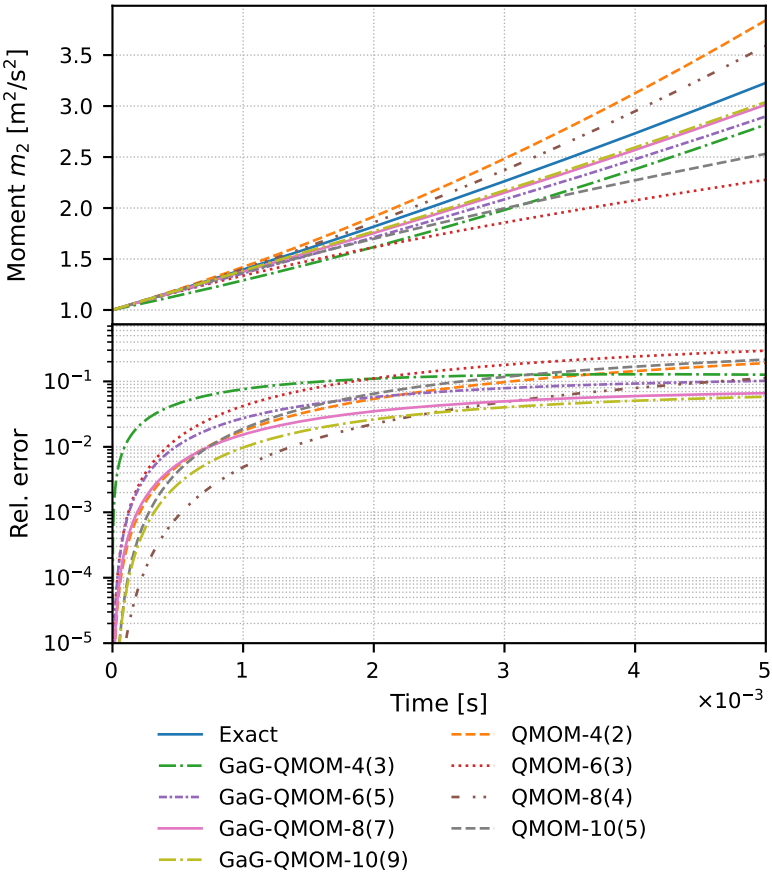

Figure 5.7.: Temporal evolution of the second moment (top) and the relative error (bottom) for Case 2 (Stratonovich diffusion), using both the QMOM and the GaG-QMOM with the RK2SSP-AR scheme.

general trend as observed in the previous section, that is, a considerably larger error of the standard QMOM approximation with a strong dependence on the parity of n.

The errors in higher-order moments are significantly smaller, as illustrated in Figures 5.8 and 5.9 for the fourth and sixth moment, respectively. Although

the higher-order moments resulting from the GaG-QMOM calculations appear to fluctuate around the analytical solution, in contrast to those of the QMOM, the shown results do not allow for a clear conclusion as to whether higher-order moments are computed more accurately by the GaG-QMOM in this particular case.

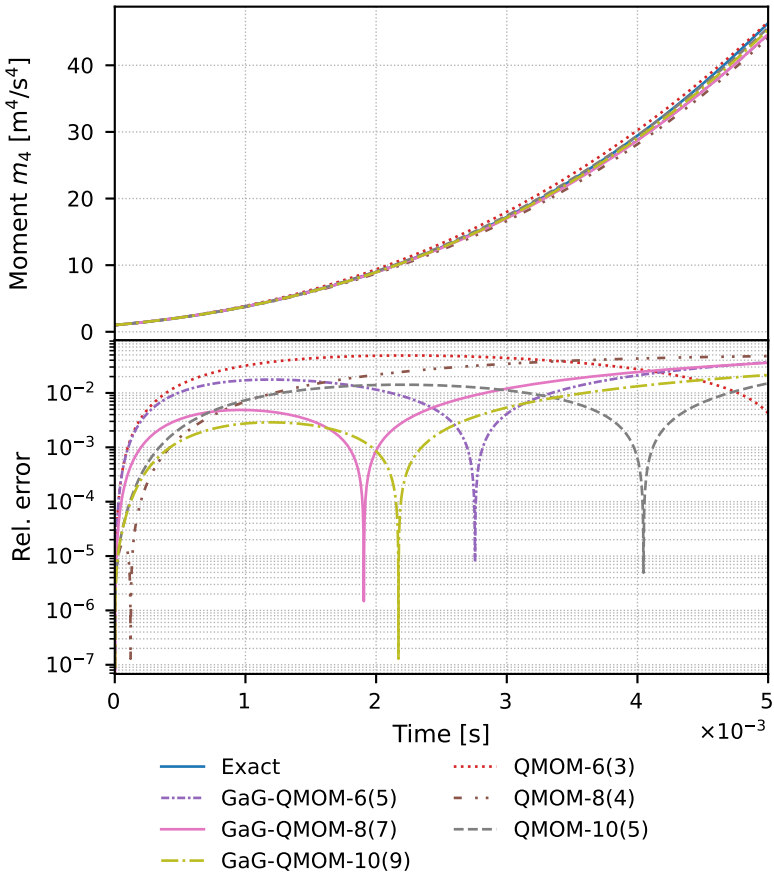

Figure 5.8.: Temporal evolution of the fourth moment (top) and the relative error (bottom) for Case 2 (Stratonovich diffusion), using both the QMOM and the GaG-QMOM with the RK2SSP-AR scheme.

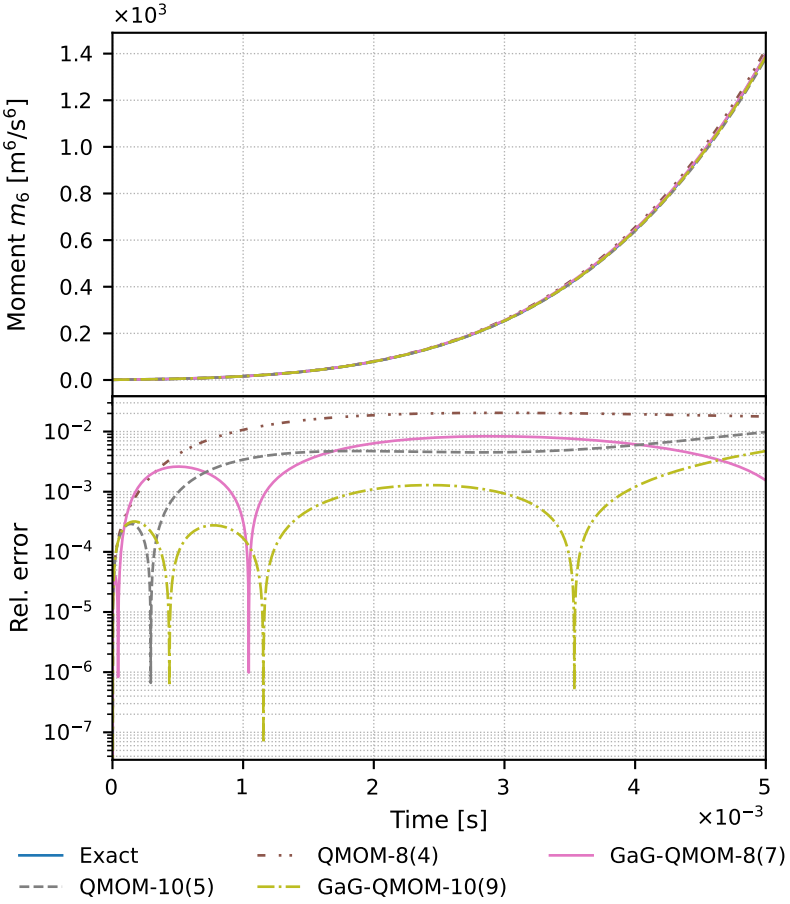

Figure 5.9.: Temporal evolution of the sixth moment (top) and the relative error (bottom) for Case 2 (Stratonovich diffusion), using both the QMOM and the GaG-QMOM with the RK2SSP-AR scheme.

To summarize this section, the case of Stratonovich diffusion with an initial two-point distribution of particle velocities revealed that the QMOM is more accurate than the GaG-QMOM in the very particular cases where the moment set is on the boundary of the moment space due to the different quadrature forms. However, with increasing distance to the moment space boundary as a result of

turbulence-induced dispersion, the behavior discussed in Case 1 can be observed again. While the errors in higher-order moments are not entirely conclusive here, the second moment, the only moment that represents a relevant physical quantity (kinetic energy), becomes more accurate using the GaG-QMOM after some time.

5.4.4. Case 3: Steady-State Fokker-Planck Equation

This final test case aims at the numerical investigation of the complete model formulated in Section 5.1 with QBMMs. As a general analytical solution of the Fokker-Planck equation exists only for the steady state, this configuration is limited to the case where advective and diffusive fluxes are at an equilibrium. That is, exact moments are provided as the initial condition, and their evolution over time is observed until no further change is detected.

In contrast to the previously discussed cases, an adaptive step size control can be employed. Here a simple step doubling method is used: At each time step from t_i to t_{i+1}, the solution is first approximated in a single step with step size Δt and then in two steps with step size $\Delta t/2$. The difference can then be used to estimate the error and, based on Richardson extrapolation and an allowed absolute and relative error, a new optimal step size is computed. A more detailed description of the procedure can be found in several textbooks on the numerical solution of ODEs, e.g. [67, Sec. II.4]. Here the allowed absolute error was set to 10^{-7} and the relative error to 10^{-5}. The initial step size was set to $\Delta t = 10^{-6}$ s.

Governing equations and initial conditions

The governing moment equations corresponding to the complete Fokker-Planck model with advection and diffusion terms is given by (5.17). The analytical steady-state solution serves as initial condition, i.e.

$$m_k(0) = m_k^{\text{analyt}}, \quad k = 0, 1, \ldots, 2n-1, \tag{5.62}$$

where m_k^{analyt} is given in (5.63) below.

Analytical reference solution

The analytical solution in terms of moments is obtained by simply applying the moment definition (2.17) to the stationary solution of the Fokker-Planck equation (5.18), which yields

$$m_k^{\text{analyt}} = \begin{cases} C\,\Gamma\left(\dfrac{1+2k}{4}\right)\dfrac{\phi^4}{\gamma}\left(\dfrac{\gamma}{\phi^2}\right)^{(3-2k)/4} & \text{if } k \text{ is even,} \\ 0 & \text{otherwise,} \end{cases} \tag{5.63}$$

where Γ is the gamma function, and the normalization constant can be written as

$$C = m_0 \left[\Gamma\left(\frac{1}{4}\right)\phi^{5/2}\gamma^{-1/4}\right]^{-1}, \tag{5.64}$$

see also Appendix A.4.

Results

Figure 5.10 provides a first overview of how well the different QBMMs approximate the exact steady-state solution in terms of the second and the fourth moment. The RK2SSP-AR scheme was employed in all cases. The difference between the QMOM and the GaG-QMOM is remarkable. The standard QMOM exhibits very large errors in both the second and fourth moment with the previously discussed strong dependence on the parity of n. The GaG-QMOM on the other hand, yields significantly more accurate results, though the error is still large for low numbers of transported moments, in particular that of the four-moment GaG-QMOM. This observation suggests that the consideration of only four moments is just not sufficient for an approximation with acceptable accuracy for the examined kind of problem. Based on the shown results, this is certainly true for the standard QMOM, irrespective of the number of moments.

Figure 5.11 shows a comparison of the GaG-QMOM with the EQMOM (with 100 second quadrature nodes) in terms of the second moment and its relative error, using the standard RK2SSP scheme for temporal integration.[6] Interestingly,

[6]The used implementation of the RK2SSP-AR scheme was not optimized, resulting in excessive

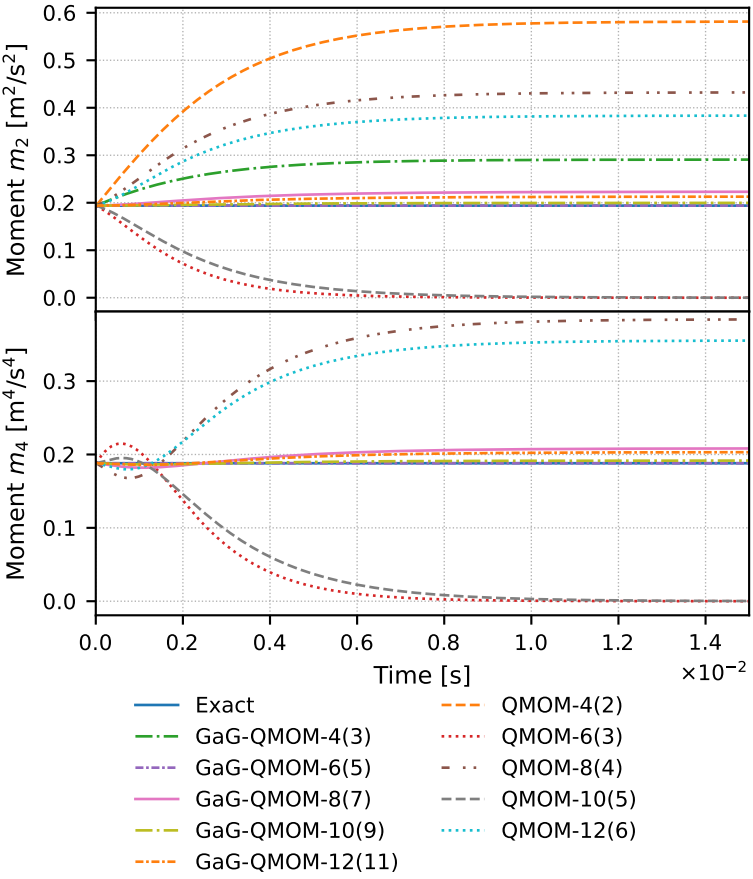

Figure 5.10.: The second (top) and fourth moment (bottom) for Case 3 (stationary Fokker-Planck equation) using QBMMs with up to 12 moments and the RK2SSP-AR scheme.

the two-KDF EQMOM gives considerably better results than the higher-order EQMOM approximations, though still with overall poor accuracy. The GaG-

computation times when using the relatively large number of second quadrature nodes. Thus, the EQMOM was combined with the ordinary RK2SSP method for convenience.

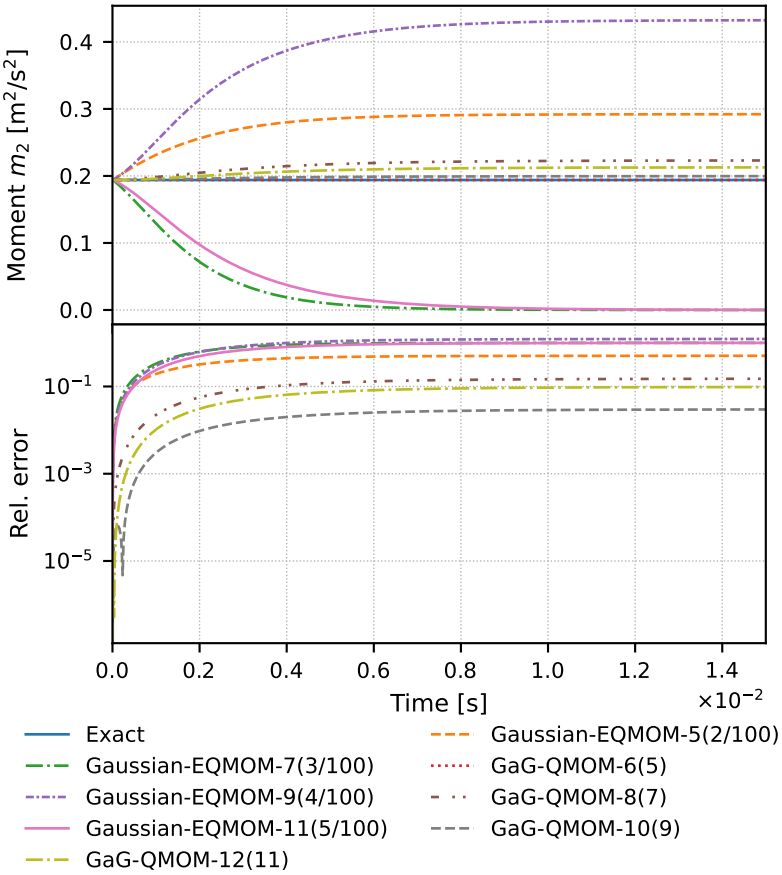

Figure 5.11.: The second (top) and fourth moment (bottom) for Case 3 (stationary Fokker-Planck equation) using QBMMs with up to 12 moments and the RK2SSP scheme.

QMOM also displays errors that seem, at first, uncorrelated with the order of the respective method, which is detailed further below. Overall, the results in Figure 5.11 confirm the observation in Section 5.4.2 that the EQMOM is not able to significantly improve the quality of results for the investigated type of problem. Thus, the EQMOM will hereafter be disregarded. Instead, the rest of this

section is primarily focused on the GaG-QMOM.

The signed relative errors in the second moment resulting from the GaG-QMOM with up to 16 moments are illustrated in Figure 5.12, where the solid lines represent the RK2SSP scheme and the dashed lines the RK2SSP-AR scheme. First, it is evident that the RK2SSP-AR scheme is a suitable realizable alternative to the regular RK2SSP scheme, displaying only a slightly larger error, whereas the results were virtually identical in Section 5.4.2. The difference is not surprising considering that the steps accounting for microscale advection (see Section 5.3) have no effect in case of the pure Itô diffusion problem. Furthermore, it can be seen that the GaG-QMOM generally appears to overestimate the second moment.

The most striking results in Figure 5.12 are those of the GaG-QMOM6(5), exhibiting very small errors when combined with the RK2SSP-AR method while the results are even exact with the RK2SSP scheme. The explanation for this behavior is not that the quadrature is exact (otherwise the GaG-QMOM6(5) would have been exact as well in the previously investigated cases) but that the errors of the quadrature approximations to the integral terms in (5.22) cancel each other out in the very specific case that the NDF equals the steady-state solution of the Fokker-Planck equation, see Appendix A.5. As regards the other approximations, it can be said that there is still a notable difference depending on whether n is even or odd: With even n the quadrature approximations have larger errors but display the generally expected behavior that they decrease with increasing number of nodes, whereas the methods with even n display significantly higher accuracy in general with an error of about 3 %, albeit without further improvement when using a larger number of quadrature nodes.

As the integral terms in the moment equations have different forms with different quadrature errors and the resulting moments represent the sum of those, it is natural to take a closer look at the errors of each term contributing to $\mathrm{d}m_k/\mathrm{d}t$, see Figure 5.13. The exact expressions for the integral terms in the stationary moment equations are given in Appendix A.4. In Figure 5.13 the terms representing noise-induced advection and diffusion are summarized because both terms differ only in constants for all moments with orders greater than one. Further, the presented results were computed with the ordinary RK2SSP method since, contrary to the RK2SSP-AR scheme, the integral terms appearing

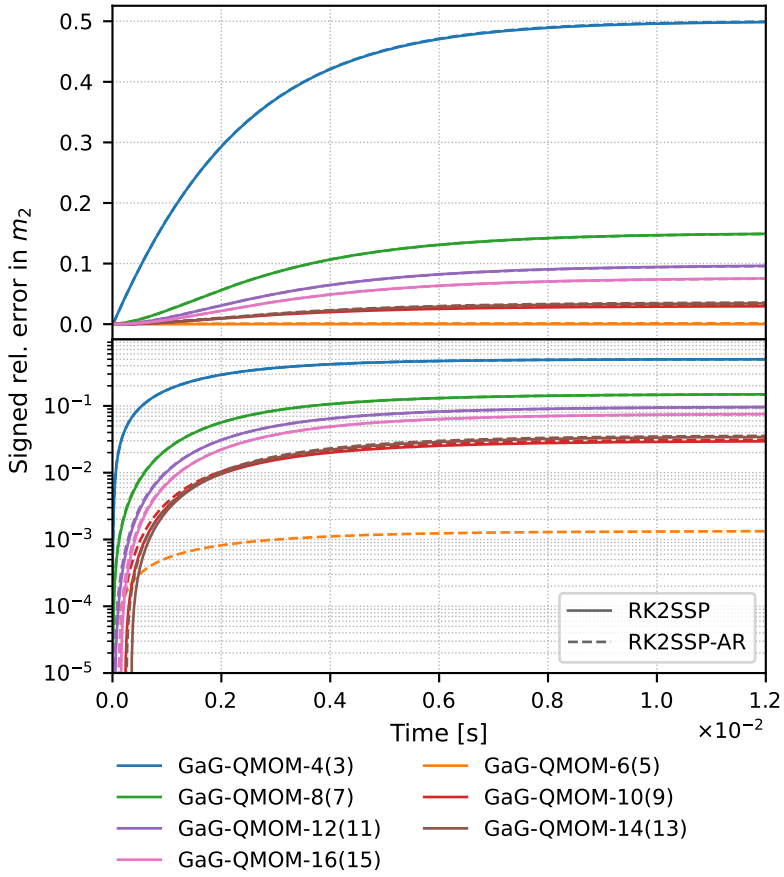

Figure 5.12.: The signed relative error in the second moment for Case 3 (stationary Fokker-Planck equation) resulting from the GaG-QMOM with the RK2SSP and the RK2SSP-AR scheme, scaled linearly (top) and logarithmically (bottom).

in the moment equations are calculated explicitly. The behavior of the errors related to the GaG-QMOM6(5) highlights the fact that the exactness of moments in the stationary case is a result of a beneficial cancellation of errors rather than an exact quadrature, exhibiting the largest errors at time $t = 0$. With the ex-

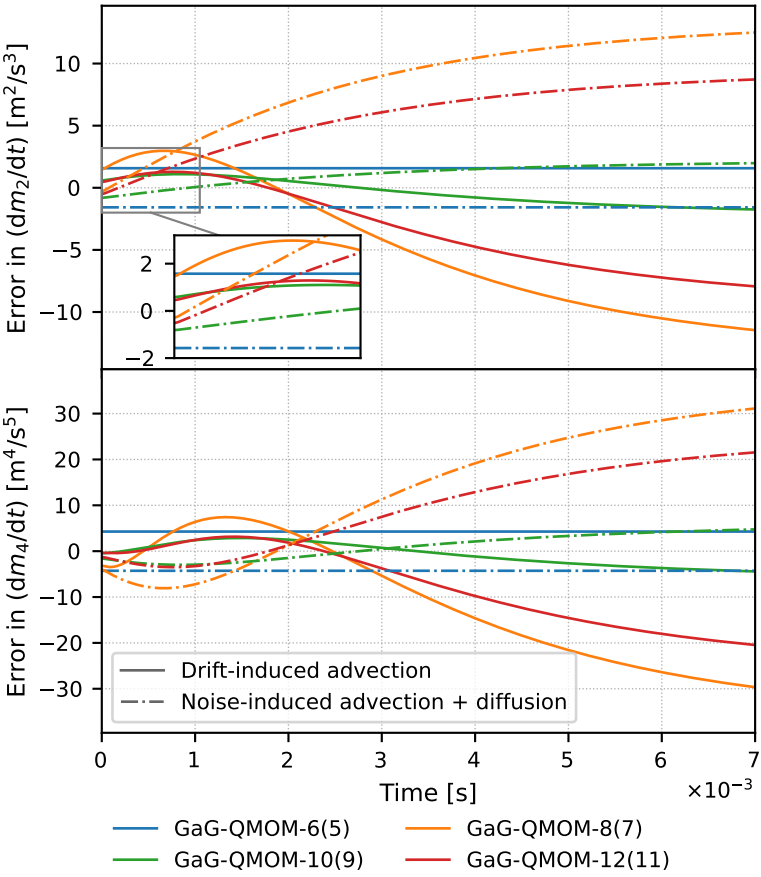

Figure 5.13.: Errors in the second moment (top) and fourth moment (bottom) equations for Case 3 (stationary Fokker-Planck equation) using the GaG-QMOM with up to 12 moments and the standard RK2SSP scheme.

act solution as the initial condition, it can be said that all errors over time until reaching an equilibrium originate from the errors at time $t = 0$. Initially, the noise-induced terms in the second moment equation are underestimated by all methods, whereas the advection is overestimated. However, the introduced mo-

ment errors interact in a way that this effect is reversed and the noise-induced terms are eventually overestimated to a larger extent than the advection term is underestimated, resulting in moments that correspond to a larger spread of the underlying NDF. It is also apparent that the methods of quadrature-based closure with odd n, i.e. an even-node Gaussian quadrature combined with an odd-node anti-Gaussian quadrature, are more accurate, not only in terms of the resulting moments but also the quadrature approximation of each of the integral terms in the moment equations.

The results of all applied numerical configurations with up to 20 moments are summarized in Figure 5.14. With the exception of the GaG-QMOM6(5), which yields the exact moments as discussed above, only minor deviations of the RK2SSP-AR from the RK2SSP scheme can be observed. Thus, the statement above that the RK2SSP-AR is an adequate alternative to the RK2SSP method in cases where moment realizability is a potentially critical issue can be confirmed, considering all tested methods. As for the quadrature-based closure, the QMOM displays very large errors and only a slight increase in accuracy by raising the number of quadrature nodes, which allows for the conclusion that no standard QMOM approximation can yield sufficiently accurate results for this type of problem. Using the GaG-QMOM, the quality of the approximation in terms of the relative error could be improved by one to two orders of magnitude, though lower-degree approximations still exhibit a relatively large error. Furthermore, the results in Figure 5.14 confirm the general trend found above, namely that higher-order moments display smaller relative errors for all methods.

To conclude this final test case, it can be said that the trends identified in the numerical investigation of the previous test cases were confirmed and quantified. The main findings are the following: First, the RK2SSP-AR scheme, displaying only small deviations from the original RK2SSP method, is a suitable alternative for cases where moment realizability is expected to become a potentially critical problem. Second, the approximation by the standard QMOM results in very large errors with the sign depending on the parity of n. Using the well-established EQMOM with Gaussian KDFs did not lead to a substantial improvement in accuracy, even with a large number of second quadrature nodes. Even though the dependence on the parity of n is still observable using the GaG-QMOM, the errors can be reduced significantly, more precisely, from

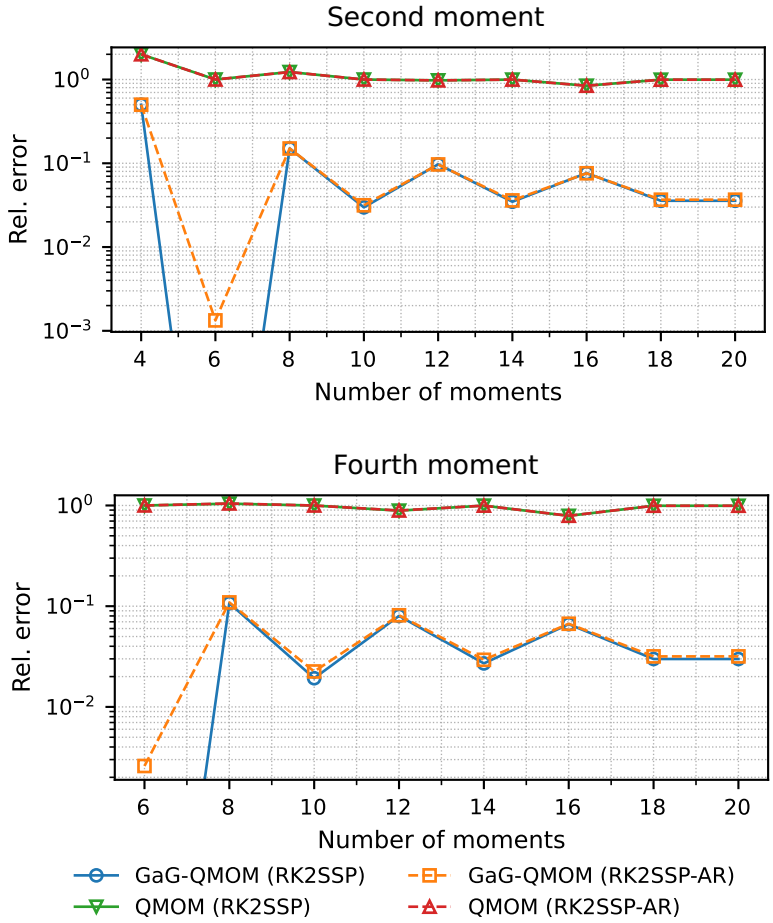

Figure 5.14.: Summary of investigated methods used for Case 3 (stationary Fokker-Planck equation) in terms of the relative error in the second (top) and fourth (bottom) moment against the number of solved moment equations.

relative errors in the order of unity to errors in the order of 10^{-2} when considering more than four moments. Moreover, the GaG-QMOM6(5) is exact when the underlying PBE is a Fokker-Planck equation with advection and diffusion coefficients of the form derived in Section 5.1. This property, albeit the result of

error cancellation, could be exploited in particular cases close to the equilibrium state.

5.5. Summary and Conclusion

This chapter has focused on the numerical solution of moment transport equations derived from PBEs with turbulence-induced diffusion in phase space using QBMMs. Based on a simplified microscopic and the corresponding mesoscopic description of turbulent momentum exchange, which takes the form of a nonlinear Fokker-Planck equation, the macroscale equations were formulated, that is, the moment equations governing a spatially homogeneous system. The arising unclosed integral terms are nonlinear and non-smooth, which was, in accordance with the theory of Gaussian quadratures, identified as a source of potentially large errors. Based on theoretical considerations as well as numerical results, the sign of those errors were found to be largely determined by the parity of the number of Gaussian quadrature nodes. Making use of this information, the standard QMOM was modified using an alternative quadrature rule that is formed by the average of an ordinary Gaussian quadrature and a so-called anti-Gaussian quadrature [86], referred to as Gauss/anti-Gauss (GaG) quadrature, in order to mitigate the undesired effects entailed by the nonlinear turbulence-induced terms. Moreover, a variation of the second-order strong-stability preserving Runge-Kutta (RK2SSP) method was provided that ensures the preservation of moment realizability in the presence of phase-space diffusion.

These numerical methods were applied in a series of univariate test cases with analytical reference solutions and compared to the standard QMOM as well as the Gaussian-EQMOM. The major findings were the following:

- The ordinary Gaussian quadrature used by the standard QMOM is accompanied by very large approximation errors with the expected dependence on the parity of the number of quadrature nodes, particularly in the important second moment, which is proportional to kinetic energy.
- Using the Gaussian-EQMOM does not lead to a significant gain in accuracy, even with many second quadrature nodes.

- The GaG-QMOM is able to reduce these large errors by one to two orders of magnitude.
- As a consequence of error cancellation, the five-node (six-moment) GaG-QMOM yields, depending on the used temporal discretization, accurate or even exact results for the steady-state Fokker-Planck equation.
- The realizable variation of the RK2SSP scheme can serve as an adequate alternative scheme in cases where moment realizability is expected to become a critical issue.

To conclude this chapter, it should be emphasized that the proposed extension of the QMOM, the GaG-QMOM, is not limited to the particular physical problem investigated here, but rather an alternative closure of moment equations involving non-smooth integral terms. The generalization to multivariate PBEs as well as its application to other physical problems are possible subjects of future research.

6. Performance and Accuracy of the Basic Quadrature-Based Closure Algorithm

The method introduced by McGraw [107] as the QMOM (see Section 3.5.1) is, at least in parts, the fundamental core routine of most QBMMs. For the numerical simulation of transient, spatially three-dimensional systems, the moment closure algorithm must be performed at every point in discretized time and physical space, for some QBMMs even multiple times, as highlighted in Section 3.5.2 (in particular Figure 3.3) for the EQMOM, and in Section 3.5.3 for common multivariate QBMMs. Accordingly, the algorithm is executed many millions to billions of times in large-scale simulations. That as well as the fact that the use of QBMMs is often motivated by computational efficiency [32, 100, 179] raises the question of how to choose the building blocks of the core algorithm appropriately in different cases to optimize it and potentially save tremendous computational resources. Of the countless publications on the development and application of QBMMs, computational costs are only addressed in a few, e.g. [76, 100], where computation times are reported for the QMOM procedure in its entirety. Detailed analyses in terms of the computational costs of the algorithm's components, are, to the author's best knowledge, not available in the literature.

The main objective of this chapter is to investigate which parts of the basic quadrature-based moment closure algorithm are the most critical with respect to performance and accuracy in different numerical and physical configurations. More precisely, the following questions will be addressed:

1) What are suitable numerical methods for different parts of the algorithm?

2) Are some of those methods more efficient or accurate than others?

3) Are certain common practical implementations advantageous with respect to performance and accuracy?

4) How is accuracy of different numerical configurations affected by the processed moment sequence?

5) What parts of the moment closure algorithm are dominant in terms of computational costs and should be optimized to enhance the overall performance?

For this purpose, the three main components of the quadrature-based moment closure algorithm will be briefly summarized first. Then, after discussing the methodology underlying the numerical study on performance and accuracy, the most important results will be presented, before concluding this chapter with a summary of the major findings.

6.1. Components of the Quadrature-Based Closure Algorithm

One of the main objectives of the numerical investigations in this chapter is to quantify the effects of each step in the basic moment closure algorithm on overall performance and accuracy. These steps are:

(I) Computation of the recurrence coefficients from a sequence of moments to assemble the Jacobi matrix:

$$\boldsymbol{m}_{2n-1} \rightarrow \mathbf{J}_n.$$

(II) Solution of the eigenvalue/eigenvector problem associated with $\mathbf{J}_n$ to obtain the quadrature nodes and weights:

$$\mathbf{J}_n \rightarrow w_j, \xi_j, \quad j = 1, \ldots, n.$$

(III) Application of the quadrature rule to approximate the integral terms in the moment equations:

$$w_j, \xi_j \rightarrow \mathrm{d}m_k/\mathrm{d}t, \quad j = 1, \ldots, n, \quad k = 0, \ldots, 2n-1.$$

Corresponding to the numbering above, the three components are hereinafter referred to as Subroutine I, Subroutine II and Subroutine III. The following subsections provide some important details on the methods applied in each of those steps.

6.1.1. Subroutine I: Computing the Jacobi Matrix from Moments

Algorithms suitable to compute the Jacobi matrix $\mathbf{J}_n$ from a sequence of moments $\boldsymbol{m}_{2n-1}$ have already been discussed in Section 3.4. The numerical study in this chapter includes the comparison of two of those, namely

- the long quotient-modified difference algorithm (LQMDA) in the form proposed by Sack and Donovan [143] (see Section 3.4.1),
- the Golub-Welsch algorithm (GWA, see Section 3.4.2).

As to the latter, it was mentioned in Section 3.4.2 that the unavailable moment m_{2n} must be chosen appropriately for the Hankel moment matrix $\mathbf{M}_{n+1}$ to become positive-definite when using implementations of the Cholesky factorization provided by common numerical linear algebra packages. The approach employed for the investigations in Section 6.3 is as simple as setting m_{2n} to the value 10^{200}, which should suffice for all realistic configurations. The PDA and QDA are disregarded for the reasons stated in Section 3.4.

6.1.2. Subroutine II: Solving the Eigenvalue Problem for the Jacobi Matrix

As pointed out in Section 3.2, the quadrature abscissas are the eigenvalues of the Jacobi matrix $\mathbf{J}_n$ while the quadrature weights result from its eigenvectors. In order to solve the eigenvalue problem associated with general matrices, one may choose from numerous methods, which can be found in most textbooks on numerical linear algebra, e.g. [30, 57]. However, comparatively few algorithms to solve the eigenvalue problem associated with tridiagonal symmetric matrices are practically used and implemented in established numerical linear algebra packages such as *LAPACK* [4], namely the well-known QR algorithm, the Divide

& Conquer (DC) algorithm [26], Relatively Robust Representations (RRR) [36, 121] and bisection with inverse iteration (BI) [6].

Demmel et al. [31] compared the *LAPACK* implementations of the four above-mentioned algorithms in terms of performance and accuracy and concluded that the DC and RRR are much faster than QR and BI on large matrices and that QR and DC are the most accurate algorithms of those investigated. While these findings may give valuable hints as to which methods are most suitable for the application of interest, they are hardly transferable to the eigenvalue problem associated with QBMMs due to the focus on larger matrices, whereas the primary concern here are very small matrices with $n \leq 10$. Moreover, instead of a general set of test matrices, the numerical study in this chapter aims to quantify accuracy depending on characteristics of the underlying moment set.

The DC algorithm uses QR iterations to compute the eigenvalues of submatrices, which is a very efficient approach for matrices larger than $n \approx 25$ [30, 31]. For matrices as small as the Jacobi matrices in the inversion procedure of QBMMs, the DC algorithm is not suitable and is thus not considered any further, neither is the BI, which is most suited to finding subsets instead of the entire spectrum [30]. Both of the remaining two algorithms, namely the QR and the RRR algorithm, need $O(n^2)$ FLOPs to find all eigenvalues [30, 36, 121]. If the eigenvectors are also computed, the complexity of the QR algorithm is $O(n^3)$ while that of RRR is only $O(n^2)$.

Given the computational complexity to compute the eigenvectors, the question arises whether it is more efficient in some cases to use the computed eigenvalues and available moment information with a fast $O(n^2)$ algorithm like that of Björck and Pereyra [12] to solve the Vandermonde system

$$\begin{pmatrix} 1 & 1 & \dots & 1 \\ \xi_1 & \xi_2 & \dots & \xi_n \\ \vdots & \vdots & \ddots & \vdots \\ \xi_1^{n-1} & \xi_2^{n-1} & \dots & \xi_n^{n-1} \end{pmatrix} \begin{pmatrix} w_1 \\ w_2 \\ \vdots \\ w_n \end{pmatrix} = \begin{pmatrix} m_0 \\ m_1 \\ \vdots \\ m_{n-1} \end{pmatrix}. \tag{6.1}$$

Even though Vandermonde matrices tend to be ill-conditioned [120] it is worth examining if, in specific cases, this approach could be the faster alternative to compute the weights of the Gaussian quadrature.

6.1.3. Subroutine III: Closing the Moment Equations

With an available n-node Gaussian quadrature, the $2n$ moment transport equations can be closed. For the univariate PBE for a spatially homogeneous system (2.18), the quadrature form can be written as

$$\begin{aligned}\frac{\mathrm{d}m_k}{\mathrm{d}t} \approx k\sum_{j=1}^{n} w_j \xi_j^{k-1} a(\xi_j) \;+\; k(k-1)\sum_{j=1}^{n} w_j \xi_j^{k-2} d(\xi_j) \\ +\; Q_k(\boldsymbol{w}_n, \boldsymbol{\xi}_n), \quad k = 0, \ldots, 2n-1,\end{aligned} \tag{6.2}$$

where $Q_k(\boldsymbol{w}_n, \boldsymbol{\xi}_n)$ is the source term approximation using the Gaussian quadrature with weights $\boldsymbol{w}_n \in \mathbb{R}_+^n$ and abscissas $\boldsymbol{\xi}_n \in \mathbb{R}^n$, i.e.

$$Q_k(\boldsymbol{w}_n, \boldsymbol{\xi}_n) \approx \int_\Omega \xi^k \mathcal{S}(f, \xi)\, \mathrm{d}\xi. \tag{6.3}$$

The computational costs of this subroutine primarily depend on what point processes, if any, are represented by $\mathcal{S}$. In the absence of point processes or in the presence of, at most, first-order processes, e.g. particle breakage, the moment closure step has complexity $O(n^2)$. In the presence of second-order point processes, i.e. processes with particle-particle interactions such as collisions, the evaluation of each Q_k requires $O(n^2)$ FLOPs, resulting in an overall computational complexity of $O(n^3)$. Both cases are considered here (see Section 6.2.3).

6.2. Methodology

In what follows, the methodology underlying the numerical study in this chapter will be detailed, starting with a discussion on what parts of the algorithm are problem-specific with respect to performance and accuracy. Following that, the investigated configurations will be detailed in terms of test moment sequences as well as representative PBEs, and important implementation details will be addressed. Finally, the section will conclude with a description of how output data was generated and processed for meaningful results.

6.2.1. Identification of Problem-Specific Effects

Both performance and accuracy may be problem-dependent, which must be taken into account when designing a suitable set of test moments. In the fol-

lowing, this issue is addressed for each of the three subroutines separately.

Regardless of which specific algorithm is used to compute the recurrence coefficients, Subroutine I is non-iterative and the number of FLOPs depends solely on n. Thus, the performance of Subroutine I can be considered to be problem-independent. Its accuracy, on the other hand, can be expected to depend on the input moment set, more precisely, on its distance from the moment space boundary. If a moment sequence $\boldsymbol{m}_{2n-1}$ is close to $\partial\mathcal{M}_{2n-1}$, the moment matrix $\mathbf{M}_{n+1}$ for the Cholesky factorization will be almost singular when using the GWA. In case of the LQMDA, such moment sets will result in very small s_{ii} in (3.33)–(3.35) for some $i < n-1$ and, consequently, lead to larger numerical errors in the next iteration.

Subroutine II may be affected by the input moment set in terms of both performance and accuracy. This is due to the fact that commonly used eigenvalue algorithms are iterative and that their accuracy depends on how well the eigenvalues are separated [30, 57]. The robustness of such algorithms generally decreases with stronger clustering of eigenvalues. The relationship between moment sequences close to the moment space boundary and clustered eigenvalues is well illustrated by the simple example in Figure 6.1. It shows three degenerate NDFs: a three-node NDF corresponding to a realizable moment set $\boldsymbol{m}_5 \in \mathcal{M}_5 \setminus \partial\mathcal{M}_5$ (left), a two-node NDF corresponding to a weakly realizable moment set $\boldsymbol{m}_5 \in \partial\mathcal{M}_5$ (center) and a three-node NDF with a moment set close to $\partial\mathcal{M}_5$ (right). Obviously, the latter case is equivalent to clustered quadrature nodes, i.e. clustered eigenvalues of the Jacobi matrix.

The sole purpose of including Subroutine III as part of the numerical study is to gain knowledge of what steps of the algorithm require most of the computation time in specific cases and are thus worth optimizing. Naturally, the required computation time of Subroutine III is extremely problem-dependent with respect to the underlying PBE. For this reason, different representative cases are considered, as will be detailed in Section 6.2.3.

6.2.2. Data Generation

The basis of the numerical study in this chapter is a test data set comprising sequences of $2n = 4, 6, \ldots, 20$ moments. Based on the considerations in the previ-

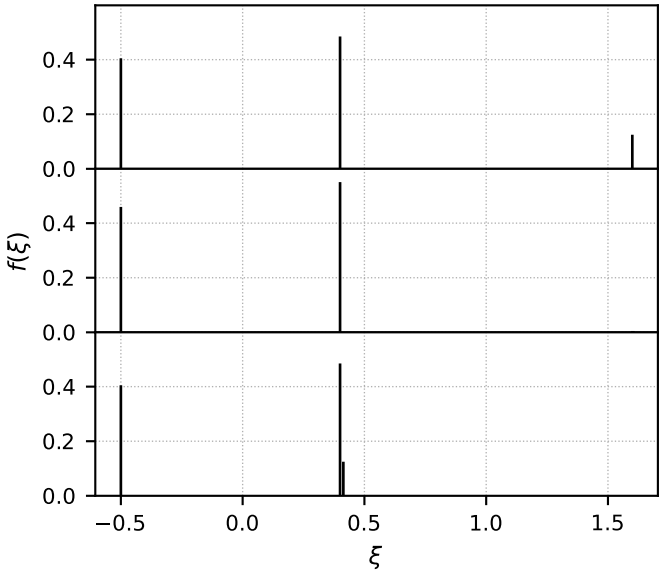

Figure 6.1.: Illustration of the relationship between the distance of moment sequences to the moment space boundary and the separation of eigenvalues of the associated Jacobi matrix. The shown NDFs correspond to moment sequences that are realizable (top), weakly realizable (center) and close to weakly realizable (bottom) with respect to the moment space $\mathcal{M}_5$.

ous section, 10^5 pseudo-random moment sequences were generated for each n to cover an appropriate range of cases with particular emphasis on moments close to the moment space boundary. This was achieved by sampling the recurrence coefficients α_i and β_i from a normal distribution and a gamma distribution[1], respectively, that is

$$\alpha_i \sim \mathcal{N}(0, \tfrac{1}{2\delta}), \quad \beta_i \sim \text{Gamma}(\lambda, \delta), \tag{6.4}$$

[1]The shape/rate parametrization with probability density $\varphi(x) = \frac{\delta^\lambda}{\Gamma(\lambda)} x^{\lambda-1} e^{-\delta x}$ is used here, where Γ denotes the gamma function.

with parameters $\delta = 1$ and $\lambda = 1/2$. It is worth noting that, with this choice of distributions for the recurrence coefficients, the probability density of the distribution of moments is known explicitly [34, 35]. However, instead of sampling the moments directly based on a relatively complex probability density for the moments, the well-known distributions in (6.4) were used to generate a pseudo-random Jacobi matrix and subsequently calculate the moment sequences from the relationship [150]

$$m_k = \boldsymbol{e}_1^T \mathbf{J}_n^k \boldsymbol{e}_1, \quad \boldsymbol{e}_1 = (1, 0, 0, \ldots, 0)^T . \tag{6.5}$$

By carrying out this calculation in long double (80-bit) precision, it is ensured that the input moments for Subroutine I are "exact" in terms of their 64-bit representation, and erroneous input data can be ruled out as a potential source of errors. For the investigation of Subroutine II, the sampled recurrence coefficients are used directly, and the moments from (6.5) are used as reference values for the calculation of errors, see also Section 6.2.6.

For later analysis, it is necessary to characterize the distance of moment sets from the moment space boundary in terms of a single scalar quantity. To this end, several options are conceivable. The simplest choice would be the smallest recurrence coefficient $\beta_{\min}$. Further possible choices are e.g. the Hankel determinant $\det(\mathbf{M}_n)$, the smallest singular value of $\mathbf{M}_n$, or its radius of regularity (radius of non-singularity) [129]. The latter defines a distance to the closest singular matrix, which is, in this sense, very similar to the smallest singular value. In fact, the smallest singular value provides a lower bound for the radius of regularity [129]. While all the mentioned quantities showed plausible and similar correlations with resulting errors, it was found in the course of the numerical investigations that the distribution of the radius of regularity, henceforth denoted by $r_{\text{reg}}(\mathbf{M}_n)$, is the most convenient for error analysis.

6.2.3. Representative Moment Equations

For a meaningful relative comparison of the subroutines in terms of computation times, three different representative PBEs are considered. As the moment sequences of interest are of Hamburger type, models with velocity as the internal coordinate, denoted by v, are used in all three cases. It should be emphasized that the equations presented below serve as representative examples for

moment equations derived from PBEs with typical terms to help estimate the computational costs for closing the moment equations. The independent process of solving the resulting system of differential equations is not subject of the study in this chapter.

Fokker-Planck equation with a constant drag coefficient

The first PBE representing a simple first-order process is the one-dimensional Fokker-Planck equation with drag and turbulence-induced diffusion that was derived in Chapter 5. Thus, the moment equations in closed quadrature form read

$$\begin{aligned}\frac{\mathrm{d}m_k(t)}{\mathrm{d}t} \approx & -k\gamma \sum_{j=1}^{n} w_j \operatorname{sgn}(v_j) v_j^{k+1} + k\frac{\phi^2}{4} \sum_{j=1}^{n} w_j \operatorname{sgn}(v_j) v_j^{k-1} \\ & + k(k-1)\frac{\phi^2}{2} \sum_{j=1}^{n} w_j \operatorname{sgn}(v_j) v_j^{k-1}, \quad k = 0, \ldots, 2n-1.\end{aligned} \tag{6.6}$$

Fokker-Planck equation with a velocity-dependent drag coefficient

The second set of tested moment equations results from the Fokker-Planck equation underlying the moment equations above, extended by a velocity-dependent drag coefficient C_d in (5.5). In fact, C_d is often modeled as a function of the velocity-dependent particle Reynolds number $\mathrm{Re_p}$. A commonly accepted expression for such a velocity-dependent drag coefficient is

$$C_d(v) = \frac{24}{\mathrm{Re_p}} \left(1 + \frac{1}{6}\mathrm{Re_p}^{2/3}\right), \tag{6.7}$$

where $\mathrm{Re_p}$ is defined as in (4.9). Evidently, this expression entails additional divisions and powers with fractional exponents to compute the RHS of the moment equations. Therefore, the second PBE can be deemed representative for other common first-order models such as particle breakage models, many of which have similar forms, see e.g. [90] and [96, Sec. 5.7.2].

Population balance equation with hard-sphere collisions

The third set of moment equations results from a PBE with a term accounting for hard-sphere collisions. It represents second-order processes, i.e. processes

with particle-particle interactions resulting in a total of $O(n^3)$ FLOPs for Subroutine III. For this purpose, a simplified form of the quadrature-based moment model for hard-sphere collisions of Fox and Vedula [47] is used, which is based on the inelastic Boltzmann-Enskog kinetic equation. In quadrature form reduced to one dimension, the collision source term can be expressed as

$$Q_k(\boldsymbol{w}_n, \boldsymbol{v}_n) = C \sum_{i=1}^{n} \sum_{j=1}^{n} w_i w_j \left|g_{i,j}\right| I_k^{(0)}(\omega_{i,j}, v_i, g_{i,j}), \tag{6.8}$$

where C is a model constant that can be determined from the particle diameter and the particle volume fraction [96, Sec. 6.1.2]. The relative velocity between particles is $g_{i,j} = v_i - v_j$ and $\omega_{i,j}$ is a measure of the elasticity of collisions. It may depend on $g_{i,j}$ or be constant, which is assumed here for the sake of simplicity, i.e.

$$\omega_{i,j} = \omega_0 = \text{const.}, \quad i, j = 1, \ldots, n. \tag{6.9}$$

The function $I_k^{(0)}(\omega, v, g)$ is a kth-degree homogeneous polynomial in v and g and results from the analytical integration over collision angles, see [47]. Defining

$$\tilde{I}_k^{(0)}(v_i, v_j) \coloneqq I_k^{(0)}(\omega_0, v_i, v_i - v_j), \tag{6.10}$$

the moment equations in closed quadrature form can be written as

$$\frac{\mathrm{d}m_k(t)}{\mathrm{d}t} \approx Q_k(\boldsymbol{w}_n, \boldsymbol{v}_n) = C \sum_{i=1}^{n} \sum_{j=1}^{n} w_i w_j \left|v_i - v_j\right| \tilde{I}_k^{(0)}(v_i, v_j). \tag{6.11}$$

6.2.4. Implementation

The applications for the numerical study were implemented in C++, see Appendix A.7 for more details. The implementation uses the *Intel® Math Kernel Library (MKL)* interface to *LAPACK*, primarily for Cholesky factorizations and for the computation of eigenvalues and eigenvectors. Moreover, to rule out implementation details as the root of significant differences in performance and accuracy, methods provided by the C++ template library *Eigen3* [63] were additionally tested as an alternative to *MKL/LAPACK* functions. The *chrono* library,

which is part of the C++ standard template library, was used to quantify performance in terms of CPU times.

Besides different libraries for numerical linear algebra operations, another measure that was taken to ascertain the meaningfulness of results was to test two different compilers, namely the C++ compiler from the *GNU Compiler Collection* as well as the *Intel® oneAPI DCP++/C++ Compiler* (see Appendix A.7). After ensuring that no significant compiler-dependent differences in computing times occurred, the *Intel®* compiler was used for the main parts of the study.

Finally, to make results more hardware-independent with respect to relative computation times, multithreading was disabled, whereas vectorization with *Advanced Vector Extensions (AVX2)* was enabled since it is supported by most processors, e.g. virtually all modern *Intel®* and *AMD* processors.

6.2.5. Execution

The numerical study was carried out using a workstation with an *Ubuntu* system and an *Intel® Core™ i7-9700K* processor. Since most test cases were executed using up to six cores simultaneously and independently, the results of selected cases were compared to those from single-core computations to make certain that the use of multiple cores does not entail any bottlenecks corrupting the results.

For the quantification of performance in terms of computation times, wall clock times were measured using the *chrono::high_resolution_clock* class. Naturally, the times measured in this way are affected by fluctuations. For this reason, the computation time for each subroutine of the closure algorithm was obtained by averaging the times of 10^4 executions.

6.2.6. Error Analysis

The main objective of the numerical investigations in this chapter is, besides measuring performance, the quantification of accuracy of the moment closure algorithm using different configurations. To this end, appropriate error measures for each of the subroutines must be defined, which is the purpose of this section.

Subroutine I takes a sequence of moments as input and computes the entries of the associated Jacobi matrix. The latter are, as explained in Section 6.2.2, the most basic output of the data generation process. Thus, the error of Subroutine I, say E_1, is measured by the relative error of the Jacobi matrix in terms of the Frobenius norm, i.e.

$$E_1(\mathbf{J}_n) = \frac{\left\| \mathbf{J}_n - \mathbf{J}_n^{(r)} \right\|_F}{\left\| \mathbf{J}_n^{(r)} \right\|_F}, \tag{6.12}$$

where $\mathbf{J}_n^{(r)}$ is the original reference matrix.

Subroutine II computes the nodes and weights of a Gaussian quadrature from a given Jacobi matrix. To quantify the accuracy, the quality of the computed quadrature is evaluated in terms of moments by first computing a set of reconstructed moments

$$m_k = \sum_{j=1}^{n} w_j \xi_j^k, \quad k = 0, 1, \ldots, 2n-1 \tag{6.13}$$

and then calculating an error with respect to the original reference moments. In this case, however, defining a relative error analogously to (6.12) would not be a suitable approach because the elements of the moment vector may differ by several orders of magnitude, which is particularly true for Hamburger sequences where the values of higher-order moments are usually significantly larger than those of lower-order moments. Thus, to prevent the errors from being determined by the higher-order moments, it is sensible to calculate a vector of relative errors first and subsequently take the norm to obtain a scalar quantity. Mathematically, the error induced by Subroutine II can then be expressed as

$$E_2(\boldsymbol{m}_{2n-1}) = \left\| \operatorname{diag}^{-1}(\boldsymbol{m}_{2n-1}^{(r)}) \left(\boldsymbol{m}_{2n-1} - \boldsymbol{m}_{2n-1}^{(r)} \right) \right\|, \tag{6.14}$$

where, again, the superscript (r) indicates the reference values.

As mentioned previously, Subroutine III is only analyzed in terms of computation times used to close the moment equations, i.e. to apply the quadrature to the RHS of (6.2). Hence, no other error measures than those defined above are needed for the interpretation of the numerical results in the following section.

6.3. Results

In this section, some major results are presented and discussed. The conducted numerical study is composed of three parts, one for each of the subroutines I and II, and one final part quantifying the relative contributions to the total computational costs of the algorithm under investigation. The number of moments was varied from 4 to 20. The more detailed illustrations in this section are based on representative numbers of 6 and 16 moments.

The tested numerical configurations include several methods for each of the algorithm's steps as well as various implementations of those methods, using the *MKL* interface to *LAPACK*, the *Eigen3* library, or C++ codes developed as part of this work, see Appendix A.7 for details.

6.3.1. Subroutine I: Computation of the Jacobi Matrix

The first subroutine of the quadrature-based closure algorithm takes a sequence of moments as input and computes, as output, the recurrence coefficients of the associated orthogonal polynomials to assemble the Jacobi matrix. As described in Section 6.2, the regularity radius of the Hankel moment matrix $r_{\mathrm{reg}}(\mathbf{M}_n)$ and the relative error of the Jacobi matrix in terms of the Frobenius norm are used to characterize the input and output quantities, respectively.

Figure 6.2 shows the distribution of the relative error over the radius of regularity for 6 and 16 moments employing the LQMDA and the GWA with a plain C++ implementation of the Cholesky decomposition, where the colors indicate the absolute frequency corresponding to each hexagonal bin. The solid line indicates the conditional geometric mean of the relative error, i.e. the mean given a fixed range of $r_{\mathrm{reg}}(\mathbf{M}_n)$. Besides the observation that, with a larger number of moments, very large errors appear to be more frequent when using the LQMDA, no significant differences in terms of the sensitivity to input quantities are visible. This is also highlighted by Figure 6.3 showing the conditional geometric mean of the relative error for all methods and implementations. The only visible differences are very close to the boundary of the moment space, which may, however, be caused by the very low sample density in that region rather than actual substantial differences in the methods' behavior.

The performance of various methods and implementations measured in terms

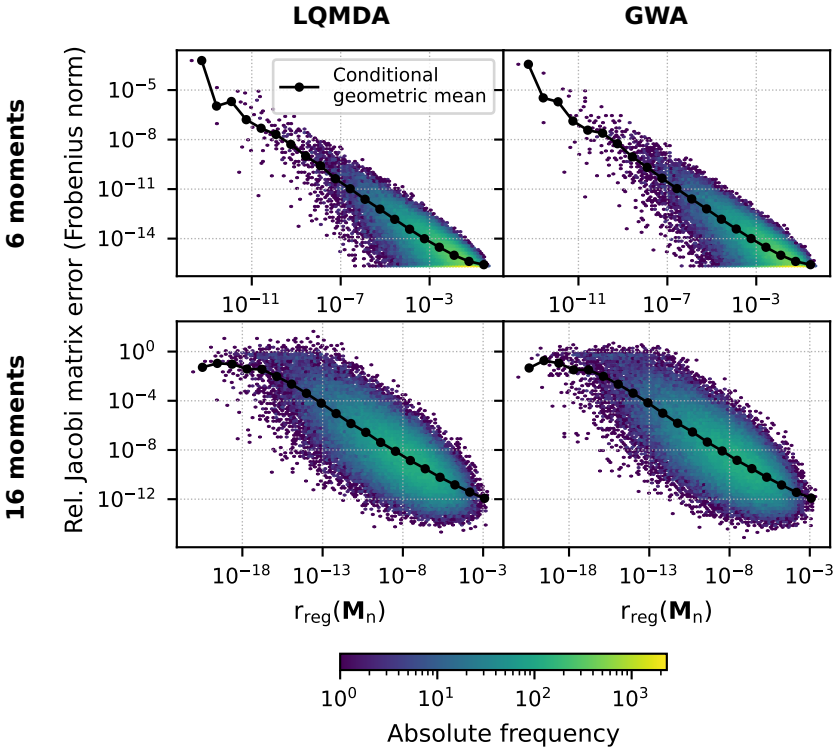

Figure 6.2.: Distribution of the error resulting from the LQMDA and GWA (with plain C++ implementation of the Cholesky decomposition) solving for 6 and 16 moments.

of executions per second is compared in Figure 6.4. The implementation of the GWA using the *LAPACK* routine POTRF2 (recursive algorithm) to compute the Cholesky decomposition is obviously not suitable for this type of problem. Further, the pure C++ implementations of the GWA are considerably faster than that using the *LAPACK* routine POTRF for small numbers of moments and twice as fast for 20 moments. Since *LAPACK* is generally known to be efficient due to the extensive use of *BLAS* (Basic Linear Algebra Subprograms [13]) operations, this clearly indicates that the computation time is dominated by data conversion and calls to interfaces to the underlying Fortran routines, which can-

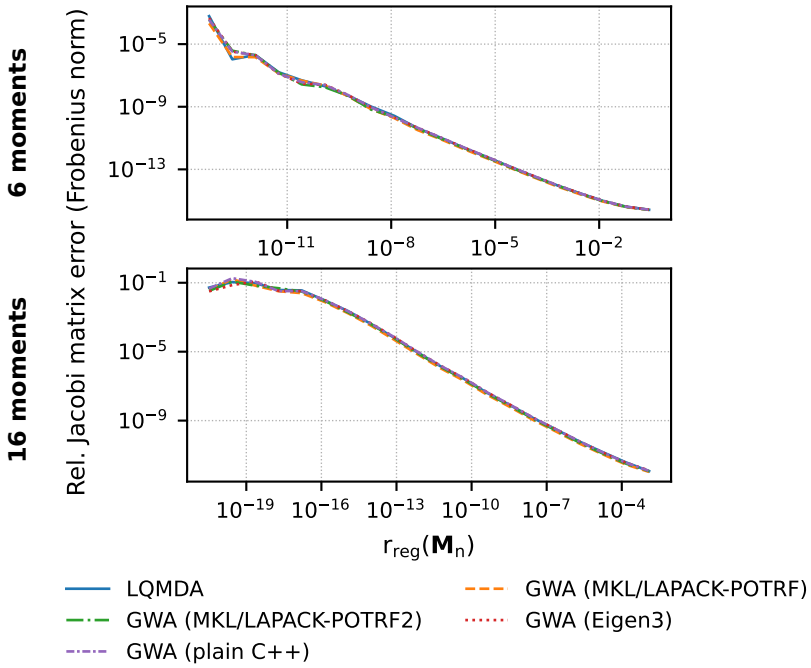

Figure 6.3.: Conditional geometric mean error of the Jacobi matrix resulting from different implementations of computing the Jacobi matrix from moments (Subroutine I).

not be compensated by performant linear algebra routines due to the very small matrices. The fastest variant of Subroutine I is the LQMDA, which, compared to the fastest version of the GWA, increases the execution frequency by a factor of about 2 for moment sequences with a size greater than 6.

Based on this first part of the study, it can be concluded that no significant differences in sensitivity to input moment sets could be observed between different methods. As regards performance, the use of standard linear algebra packages may come with significant drawbacks due to data conversion/transfer and interface calls. Moreover, the LQMDA is superior to the GWA for the considered range of moments and should be preferred unless, for some reason, additional quantities resulting from the GWA, e.g. the Hankel determinant, are needed.

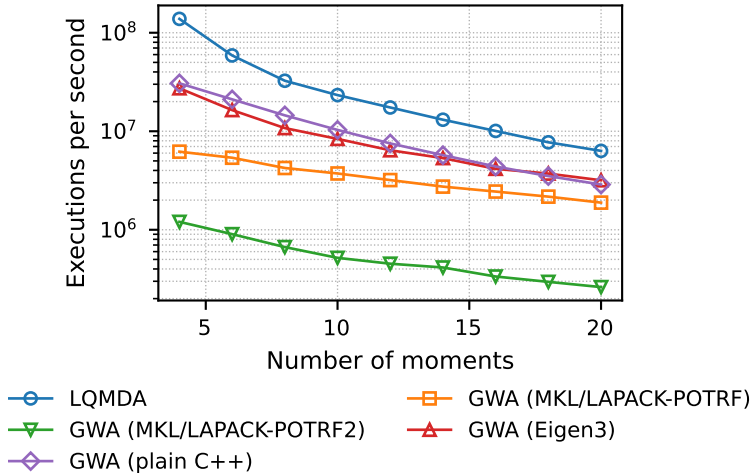

Figure 6.4.: Number of executions per second of different implementations of computing the Jacobi matrix from moments (Subroutine I).

6.3.2. Subroutine II: Solution of the Eigenvalue Problem

This section is concerned with the computation of the Gaussian quadrature rule from the Jacobi matrix. As described in Section 6.1.2, this is done by finding the eigenvalues and subsequently computing the eigenvectors or, alternatively, solving the linear Vandermonde system in (6.1). For the sake of brevity, the former will be referred to as eigenvector method and the latter as Vandermonde method for the remainder of this section.

The input of Subroutine II are the diagonals of the Jacobi matrix, i.e. the recurrence coefficients of orthogonal polynomials, which are the original quantities obtained from the sampling procedure described in Section 6.2.2. The output of Subroutine II are the abscissas and weights of the related Gaussian quadrature. However, since there is no particular interest in errors of individual nodes and weights but rather in the induced moment errors, the following results will focus on the error in reconstructed moments as defined in (6.14).

Figure 6.5 shows a comparison between the eigenvector method and the Vandermonde method in terms of relative moment errors. No substantial differences

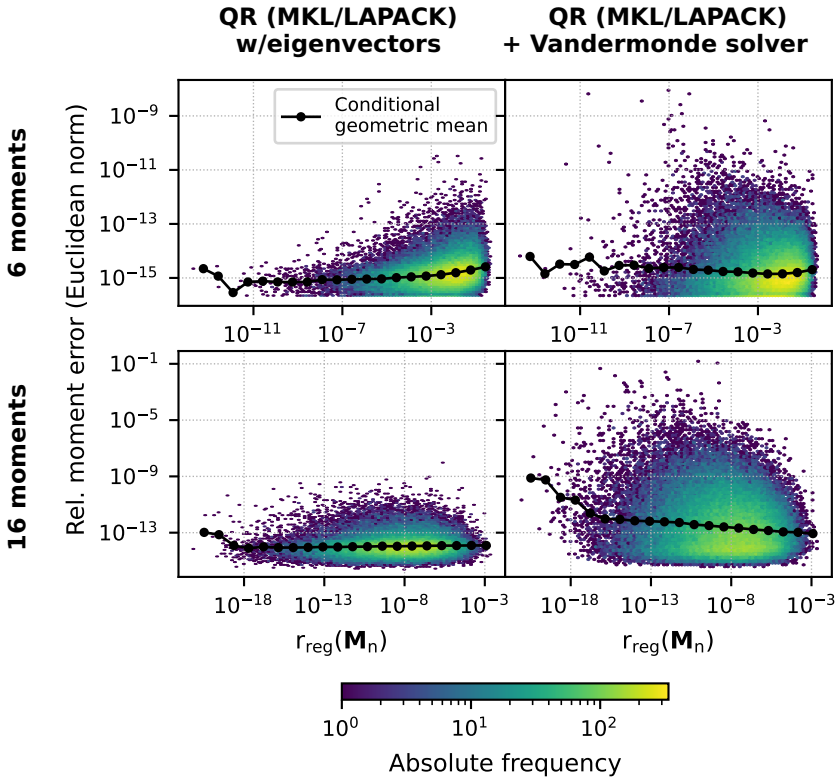

Figure 6.5.: Distribution of the relative moment error resulting from the QR algorithm with the eigenvector method (left) and the Vandermonde method (right) solving for 6 and 16 moments.

in the shape of the distribution could be observed between the tested eigenvalue algorithms. Thus, the *LAPACK* implementation of the QR algorithm is shown as an exemplary eigenvalue algorithm in both cases. Interestingly, the eigenvector method is virtually unaffected by the underlying moment sequence, even when solving for 16 moments, whereas the Vandermonde method appears to yield more accurate results with increasing distance to the moment space boundary. Generally, the Vandermonde method exhibits a higher frequency of larger errors and, with an increasing number of moments, also a significantly larger mean er-

ror in the region close to the moment space boundary. This is highlighted even more clearly in Figure 6.6, which shows a comparison of the mean relative moment errors between all tested variants. Using only 6 moments, the difference in mean errors is negligible, and all methods display an accuracy not too far from machine precision. When solving for a larger number of moments close to the moment space boundary, however, the Vandermonde method produces relative errors that exceed those of the eigenvector method by several orders of magnitude. As the distance to the critical region increases, the accuracy of the Vandermonde method approaches that of the eigenvector method.

A comparison in terms of performance over the entire investigated range of moment sets is shown in Figure 6.7. It reveals that the Vandermonde method generally tends to be faster, albeit to a very minor extent in case of the *Eigen3*

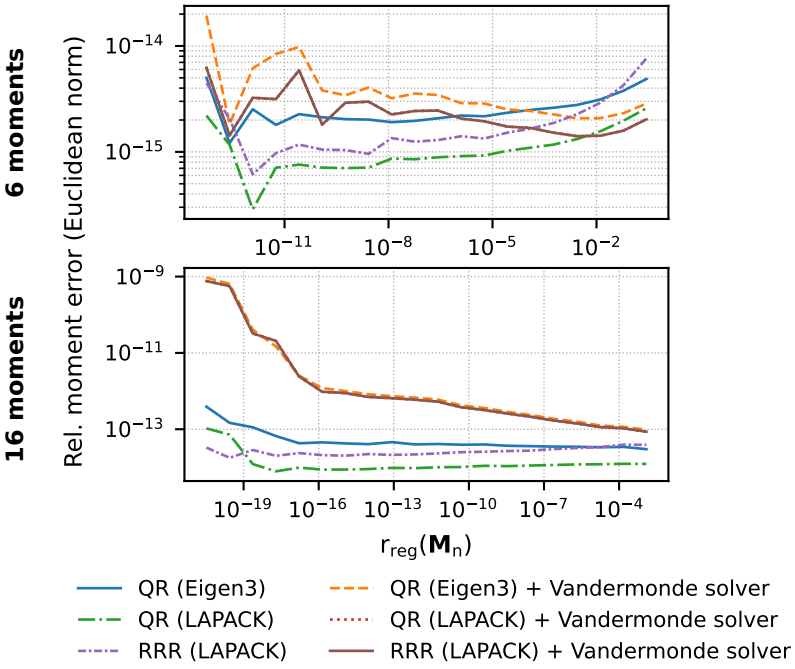

Figure 6.6.: Conditional geometric mean of relative moment errors from different implementations to solve the eigenvalue problem (Subroutine II).

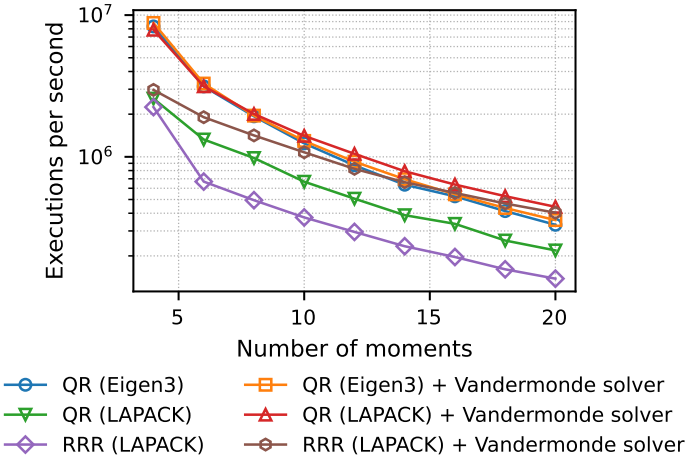

Figure 6.7.: Number of executions per second of different implementations to solve the eigenvalue problem (Subroutine II).

implementation. In contrast to Subroutine I, the superior efficiency of *LAPACK* seems to compensate the overhead due to data conversion and interface calls when computing eigenvalues only. Compared to the eigenvector method with *LAPACK*, the Vandermonde method is about twice as fast. In terms of computational efficiency, the RRR algorithm does not appear to have any advantages for the solution of the small tridiagonal symmetric eigenvalue problems arising in the moment closure algorithm.

To summarize this section, it can be said that, for the investigated moment sequences, the relative moment errors resulting from the calculation of Gaussian quadrature rules from the Jacobi matrix by computing its eigenvalues and eigenvectors is practically independent of the input moments. Solving the Vandermonde system instead of computing the eigenvectors could be an efficient alternative in cases where only a few moment equations are solved or where the distance to the moment space boundary is known to be large, e.g. in systems tending to a known equilibrium state satisfying that condition. The RRR algorithm did not display any beneficial properties for this type of problem.

6.3.3. Relative Contributions to Total Computational Costs

The last part of this numerical study deals with the question of which subroutines contribute most to the total computational costs, which is essential information needed to identify bottlenecks and to be able to properly optimize the algorithm that is executed so many times during a simulation. Since computation times and the relative contributions of the three subroutines are heavily dependent on the specific form of the moment equations, the three representative problems described in Section 6.2.3 were investigated, first, the Fokker-Planck equation with a constant drag coefficient, second, the same equation only with a velocity-dependent drag coefficient and third, hard-sphere collision. Only a single numerical configuration with regard to subroutines I and II is shown here, namely the LQMDA with the *LAPACK* implementation of the QR algorithm computing both the eigenvalues and eigenvectors. The relative computational costs for other combinations of numerical methods can be estimated using the results of the previous investigations.

The results in terms of computation times are shown in Figure 6.8. Evidently, the computational costs of Subroutine I are negligible in all cases. Accordingly, the choice between LQMDA and the GWA to compute the Jacobi matrix should hardly affect the overall performance in most cases.[2] When only first order processes are present, the computational costs are mainly determined by the solution of the eigenvalue problem, regardless of whether the specific operations are slightly more complex. However, the moment closure may become dominant in the presence of second-order processes as the number of moments increases.

As a concluding remark, it should be stressed that the results presented here can only be interpreted qualitatively due to the strong dependence on the physical problem. Even though representative terms were chosen for first-order and second-order processes, highly dynamic modular codes may be significantly less efficient and lead to a larger contribution of Subroutine III. However, the results

[2] Some QBMMs may involve multiple executions of Subroutine I before solving the eigenvalue problem in Subroutine II, e.g. the EQMOM (see Section 3.5.2) with the improved root search algorithms due to Pigou et al. [126] where the recurrence coefficients of orthogonal polynomials are repeatedly computed in an iterative procedure.

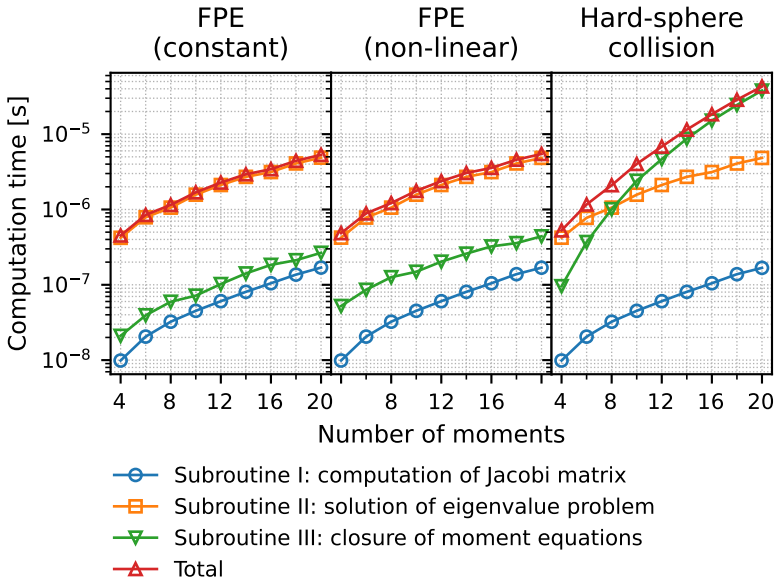

Figure 6.8.: Mean computation times of all subroutines vs. number of moments for different physical configurations, namely the Fokker-Planck equation (FPE) with a constant drag coefficient (left), the FPE with a velocity-dependent drag coefficient (center) and hard-sphere collision (right).

above justify the generalization that, for performance optimization, the computation of the Jacobi matrix from a set of moments is secondary while the solution of the eigenvalue problem to compute the Gaussian quadrature rule plays a major role in terms of the overall performance of the quadrature-based moment closure algorithm.

6.4. Summary and Conclusion

To revisit the questions raised in the very beginning of this chapter one by one, the conclusions of this chapter can be summarized as follows:

1) The LQMDA and the GWA were identified as suitable methods to calcu-

late the Jacobi matrix from moments and the QR and RRR algorithms to solve the eigenvalue problem. Additionally, the possibility to solve a linear system of Vandermonde form to determine the quadrature weights was considered as an alternative to computing the eigenvectors using the mentioned methods.

2) For the computation of the recurrence coefficients of orthogonal polynomials, the LQMDA displays the highest computational efficiency while both tested methods are almost equally accurate for the investigated moment sequences. As for solving the eigenvalue problem, the QR algorithm was found to be superior for the small eigenvalue problems appearing in QBMMs. The approach solving the Vandermonde system tends to be faster than computing the eigenvectors of the Jacobi matrix, though accuracy may suffer when using this approach with a larger number of moments or with moment sequences in the more critical region of the moment space.

3) In general, simple implementations avoiding excessive data conversions, data transfer and interface calls should be preferred for optimal performance. This is particularly true for the algorithm to compute the Jacobi matrix where the use of the *MKL* interface to *LAPACK* entails significant overhead. When computing only the eigenvalues of the Jacobi matrix that effect appears to be largely neutralized by the optimized efficiency of *LAPACK*.

4) The computed Jacobi matrix can be expected to be less accurate the closer the input moments are to an unrealizable moment set, i.e. a set corresponding to no valid density function. The same applies to the calculation of the quadrature nodes and weights by finding the eigenvalues of the Jacobi matrix and subsequently solving the Vandermonde system. In contrast, the computation of the complete eigendecomposition is apparently unaffected in terms of accuracy.

5) The extent to which each of the subroutines contributes to the overall computational costs of the algorithm is heavily dependent on the considered PBE. The contribution of the computation of recurrence coefficients

can be expected to be negligible in most cases. The solution of the eigenvalue problem is dominant when only first-order processes are present in the PBE, whereas computing the RHS of the moment equations determines the computational costs when solving a relatively large number of moment equations derived from a PBE with second-order processes. However, these statements rely on the efficient implementation of common physical models and should be understood as a qualitative conclusion.

These results can be used to estimate the computational costs of common univariate and multivariate QBMMs as well as new developments, such as the GaG-QMOM introduced in Section 5.2, and help optimize the overall efficiency of such methods.

7. Conclusion

7.1. Summary

The work presented in this thesis has been intended to contribute to the advancement of QBMMs for population balances. This includes both the formulation of physical models and the investigation and development of numerical methods, with the main focus on the latter. The reported research can be divided into three parts: First, the formulation of a commonly used model for droplet breakup in the context of QBMMs and the numerical investigation with different methods. Second, the derivation of a quadrature-based moment model for the effects of fluid phase turbulence on dispersed particles and the development of suitable methods for the numerical solution of the resulting system of moment equations. Third, the numerical exploration and analysis of the core algorithm of QBMMs in terms of performance and accuracy. The results and major conclusions, which can be found in a more comprehensive form in the concluding sections of the respective chapters, are summarized below.

For the numerical investigation of droplet breakup with QBMMs in Chapter 4, a quadrature-based moment model was first derived from the well-established Reitz-Diwakar model, a relatively simple Lagrangian model for bag and shear breakup, which are the breakup modes most frequently observed in dynamic particulate systems such as sprays. A key feature is the simplifying assumption that, for a specific breakup mode and given fluid properties, the fragments formed as a result of breakup are of constant size. Mathematically, this corresponds to a degenerate fragment size distribution, which is represented exactly by the QMOM. This property was exploited to successfully validate the model with two simple configurations involving initial populations of droplet with equal sizes. Finally, the model was applied to a more realistic initial population with log-normally distributed droplet sizes. In addition to the QMOM, the

Gamma-EQMOM, which uses Gamma-KDFs to reconstruct a continuous NDF and calculate an arbitrarily large number of quadrature nodes, was also tested. The numerical results showed that QBMMs are generally able to compute a reasonably accurate approximation of the source terms in the moment equations derived from the Reitz-Diwakar model. The application of the Gamma-EQMOM, however, did not result in enhanced accuracy, which can be attributed to the investigated system tending to a three-point distribution as well as the inaccurate representation of the initial log-normal distribution by Gamma-KDFs. Generally, the results indicated that the solved system should consist of at least six moment equations to obtain adequately accurate results.

The second major part of this work, presented in Chapter 5, was concerned with the formulation of a quadrature-based moment model for the effects of fluid turbulence on particle velocities and the identification and development of suitable methods for the numerical solution. First, starting from a simplified microscopic and the derived mesoscopic description of turbulent momentum exchange in the form of a nonlinear Fokker-Planck equation, the corresponding system of moment transport equations was formulated for a spatially homogeneous system. The nonlinear and non-smooth integral terms were identified as a source of potentially large errors when using the standard QMOM with an n-point Gaussian quadrature. Theoretical considerations suggested that the signs of those errors are primarily determined by the parity of n, which was confirmed by numerical results. Based on this information, the standard QMOM was modified using an alternative $(2n-1)$-point quadrature rule that is formed by the average of an ordinary $(n-1)$-point Gaussian quadrature and an n-point anti-Gaussian quadrature as proposed by Laurie [86]. The corresponding QBMM, referred to as Gauss/anti-Gauss QMOM (GaG-QMOM), was shown to reduce the initially large errors by one to two orders of magnitude compared to the QMOM, as opposed to the EQMOM with Gaussian KDFs, which did not bring any significant improvement in accuracy for the considered test cases. Moreover, a variation of the second-order strong-stability preserving Runge-Kutta (RK2SSP) method was developed that guarantees the unconditional preservation of moment realizability in the presence of phase-space diffusion in spatially homogeneous systems. It was shown to be a suitable alternative scheme in cases where moment realizability is expected to be critical.

The third part of the conducted research work, which was dealt with in Chapter 6, focused on the numerical exploration of the core algorithm of most QBMMs, which is performed many millions to billions of times in large-scale simulations, in terms of performance and accuracy. Essentially, the algorithm can be divided into three subroutines: first, computing the first n pairs of recurrence coefficients of the orthogonal polynomials corresponding to a given sequence of $2n$ moments to assemble the associated symmetric tridiagonal Jacobi matrix, second, solving the related eigenvalue problem to obtain n nodes and weights of the Gaussian quadrature, and third, applying the quadrature to approximate the integral terms and close the system of $2n$ moment equations. It was found that available algorithms to compute the recurrence coefficients are about equally sensitive to the input moment sequence. There are considerable differences in performance, but the contribution to the overall computational costs of the closure algorithm is negligible. The standard method to solve the eigenvalue problem associated with the Jacobi matrix was found to be insensitive to the input moment set in contrast to a less robust but slightly faster alternative that involves solving a linear system of Vandermonde form. For relatively simple physical problems, the overall computational costs were found to be mostly determined by the eigenvalue problem, whereas closing the moment equations becomes important in the presence of more complex processes with particle-particle interactions. The presented findings can help identify the potentials of optimization and make QBMMs as efficient as possible.

7.2. General Conclusions

Based on the contents of this dissertation, the following general conclusions can be inferred:

- Whenever the quantities of interest are macroscopic, QBMMs can serve as a computationally efficient alternative to more detailed mesoscale approaches for the numerical simulation of particulate systems described by PBEs. However, in contrast to computationally more expensive methods, such as stochastic methods that are theoretically applicable to arbitrarily complex models, QBMMs are limited to relatively simple mathematical

relationships in low-dimensional internal-coordinate space.

- Numerical simulations of the many physical processes best described by mathematical models involving non-smooth expressions, e.g. those studied in Chapters 4 and 5, may yield extremely inaccurate results when using common QBMMs. In such cases, special approaches are required, one of which is the GaG-QMOM developed as part of this work.

- Moment realizability may be a critical issue not only with respect to physical transport, which has been the main focus of the related research [23, 77, 85, 147, 166, 167], but also transport in phase space. This must be taken into account by using appropriate methods. A method specifically suited to phase-space diffusion is the absolutely realizable variant of the RK2SSP scheme proposed in Chapter 5.

- For the efficient solution of moment transport equations with QBMMs, the primary focus should be on the fast solution of the eigenvalue problem in the moment inversion procedure and, depending on the presence or absence of second-order processes in the underlying PBE, the efficient implementation of the moment source term evaluation.

7.3. Suggestions for Future Research

To conclude this thesis, some suggestions for future research topics are provided below.

- *Applications involving more complex integral expressions:* For the most part, the numerical studies conducted in the course of this work were based on simplified models to enable a thorough analysis of the applied numerical methods with respect to analytical reference solutions. Potentially physically relevant effects resulting in more complex expressions in the moment equations, e.g. a velocity-dependent drag coefficient in the Fokker-Planck equation in Chapter 5, were neglected. The extension of the models to more complex forms as well as the application and, if necessary, adaptation of the developed numerical methods are possible research tasks for the future.

- *Extension of the GaG-QMOM to Hausdorff and Stieltjes problems:* It was highlighted that the GaG-QMOM is only suitable for Hamburger problems as the outer nodes of the anti-Gaussian quadrature may be located outside the support interval. Extending the method to NDFs with finite support $[a, b]$ (Hausdorff problem) and semi-infinite support $[a, \infty)$ (Stieltjes problem) to make it applicable to common internal coordinates such as particle size is a possibly interesting subject of future research. A possible approach to accomplish that is the combination with a Gauss-Radau quadrature for Hausdorff problems or a Gauss-Lobatto quadrature for Stieltjes problems to fix the outer quadrature nodes at the phase-space boundaries.

- *Extension to multivariate problems:* Except for the model formulation in Chapter 5, the presented research was limited to univariate problems. However, many physical problems require a multivariate description, i.e. multiple internal coordinates. Accordingly, the extension of the developed methods to multivariate problems is an interesting topic of future research. While the necessary modification of the RK2SSP requires only minor adjustments like the use of multivariate instead of univariate normal moments, the extension of the GaG-QMOM must be combined with multivariate approaches such as the CQMOM. First considerations imply that this is theoretically possible by raising the number of conditional moments to match the increased number of quadrature nodes. However, that approach can be expected to aggravate the known problem of moment realizability with multivariate QBMMs, another challenge that would have to be met with novel numerical methods.

The setups for the conducted numerical studies as well as the software developed as part of this work can serve as a solid basis to approach these challenges.

References

[1] R. V. Abramov. "An improved algorithm for the multidimensional moment-constrained maximum entropy problem." *Journal of Computational Physics* **226** (2007), 621–644. DOI: https://doi.org/10.1016/j.jcp.2007.04.026.

[2] M. Abramowitz and I. A. Stegun, eds. *Handbook of Mathematical Functions with Formulas, Graphs, and Mathematical Tables*. Tenth Printing. U.S. Government Printing Office, 1972.

[3] "An algorithm for finding the distribution of maximal entropy." *Journal of Computational Physics* **30** (1979), 250–258. DOI: https://doi.org/10.1016/0021-9991(79)90102-5.

[4] E. Anderson et al. *LAPACK Users' Guide*. Third. Society for Industrial and Applied Mathematics, 1999.

[5] G. A. Athanassoulis and P. N. Gavriliadis. "The truncated Hausdorff moment problem solved by using kernel density functions." *Probabilistic Engineering Mechanics* **17** (2002), 273–291. DOI: https://doi.org/10.1016/S0266-8920(02)00012-7.

[6] W. Barth, R. S. Martin, and J. H. Wilkinson. "Calculation of the eigenvalues of a symmetric tridiagonal matrix by the method of bisection." *Numerische Mathematik* **9** (1967), 386–393.

[7] G. K. Batchelor. *An Introduction to Fluid Dynamics*. Cambridge Mathematical Library. Cambridge University Press, 2000.

[8] A. Bensberg, P. Roth, R. Brink, and H. Lange. "Modeling of particle evolution in aerosol reactors with coflowing gaseous reactants." *AIChE Journal* **45** (1999), 2097–2107. DOI: https://doi.org/10.1002/aic.690451008.

[9] M. Bini and W. P. Jones. "Large-eddy simulation of particle-laden turbulent flows." *Journal of Fluid Mechanics* **614** (2008), 207–252. DOI: https://doi.org/10.1017/S0022112008003443.

[10] M. Bini and W. P. Jones. "Particle acceleration in turbulent flows: A class of nonlinear stochastic models for intermittency." *Physics of Fluids* **19** (2007), 035104. DOI: https://doi.org/10.1063/1.2709706.

[11] V. S. Birchal, L. Huang, A. S. Mujumdar, and M. L. Passos. "Spray Dryers: Modeling and Simulation." *Drying Technology* **24** (2006), 359–371. DOI: https://doi.org/10.1080/07373930600564431.

[12] Å. Björck and V. Pereyra. "Solution of Vandermonde systems of equations." *Mathematics of Computation* **24** (1970), 893–903. DOI: https://doi.org/10.2307/2004623.

[13] L. S. Blackford et al. "An updated set of basic linear algebra subprograms (BLAS)." *ACM Transactions on Mathematical Software* **28** (2002), 135–151.

[14] N. Böhmer and M. Torrilhon. "Entropic quadrature for moment approximations of the Boltzmann-BGK equation." *Journal of Computational Physics* **401** (2020), 108992. DOI: https://doi.org/10.1016/j.jcp.2019.108992.

[15] J.-P. Bourgade and F. Filbet. "Convergence of a finite volume scheme for coagulation-fragmentation equations." *Mathematics of Computation* **77** (2008), 851–883. DOI: https://doi.org/10.1090/S0025-5718-07-02054-6.

[16] J. R. Brock and J. Oates. "Moment simulation of aerosol evaporation." *Journal of Aerosol Science* **18** (1987), 59–64. DOI: https://doi.org/10.1016/0021-8502(87)90010-3.

[17] I. N. Bronshtein, K. A. Semendyayev, G. Musiol, and H. Mühlig. *Handbook of Mathematics*. 5th ed. Springer, 2007.

[18] X.-K. Cao, Z.-G. Sun, W.-F. Li, H.-F. Liu, and Z.-H. Yu. "A new breakup regime of liquid drops identified in a continuous and uniform air jet flow." *Physics of Fluids* **19** (2007), 057103. DOI: https://doi.org/10.1063/1.2723154.

[19] C. Cercignani. *The Boltzmann Equation and its Applications*. Springer, 1988.

[20] C. Chalons, R. O. Fox, and M. Massot. "A multi-Gaussian quadrature method of moments for gas-particle flows in a LES framework." *Proceedings of the Summer Program*. Center for Turbulence Research. 2010, 347–358.

[21] C. Chalons, R. O. Fox, F. Laurent, M. Massot, and A. Vié. "Multivariate Gaussian Extended Quadrature Method of Moments for Turbulent Disperse Multiphase Flow." *Multiscale Modeling & Simulation: A SIAM Interdisciplinary Journal* **15** (2017), 1553–1583. DOI: https://doi.org/10.1137/16M109209X.

[22] T. S. Chihara. *An Introduction to Orthogonal Polynomials*. Gordon and Breach, 1978.

[23] B. Choi, J. Baek, and D. You. "A realizable second-order advection method with variable flux limiters for moment transport equations." *Journal of Computational Physics* **473** (2023), 111767. DOI: https://doi.org/10.1016/j.jcp.2022.111767.

[24] W.-H. Chou and G. M. Faeth. "Temporal properties of secondary drop breakup in the bag breakup regime." *International Journal of Multiphase Flow* **24** (1998), 889–912. DOI: https://doi.org/10.1016/S0301-9322(98)00015-9.

[25] P. A. Cundall and O. D. L. Strack. "A discrete numerical model for granular assemblies." *Géotechnique* **29** (1979), 47–65. DOI: https://doi.org/10.1680/geot.1979.29.1.47.

[26] J. J. M. Cuppen. "A divide and conquer method for the symmetric tridiagonal eigenproblem." *Numerische Mathematik* **36** (1980), 177–195. DOI: https://doi.org/10.1007/BF01396757.

[27] Z. Dai and G. M. Faeth. "Temporal properties of secondary drop breakup in the multimode breakup regime." *International Journal of Multiphase Flow* **27** (2001), 217–236. DOI: https://doi.org/10.1016/S0301-9322(00)00015-X.

[28] P. J. Davis and P. Rabinowitz. *Methods of Numerical Integration*. Computer Science and Applied Mathematics. Academic Press, 1975.

[29] L. G. M. de Souza, G. Janiga, V. John, and D. Thévenin. "Reconstruction of a distribution from a finite number of moments with an adaptive spline-based algorithm." *Chemical Engineering Science* **65** (2010), 2741–2750. DOI: https://doi.org/10.1016/j.ces.2010.01.007.

[30] J. W. Demmel. *Applied Numerical Linear Algebra*. Society for Industrial and Applied Mathematics, 1997.

[31] J. W. Demmel, O. A. Marques, B. N. Parlett, and C. Vömel. "Performance and accuracy of LAPACK's symmetric tridiagonal eigensolvers." *SIAM Journal on Scientific Computing* **30** (2008), 1508–1526. DOI: https://doi.org/10.1137/070688778.

[32] O. Desjardins, R. O. Fox, and P. Villedieu. "A quadrature-based moment method for dilute fluid-particle flows." *Journal of Computational Physics* **227** (2008), 2514–2539. DOI: https://doi.org/10.1016/j.jcp.2007.10.026.

[33] H. Dette and W. J. Studden. *The Theory of Canonical Moments with Applications in Statistics, Probability, and Analysis*. Wiley Series in Probability and Statistics. John Wiley & Sons, 1997.

[34] H. Dette and J. Nagel. "Distributions on unbounded moment spaces and random moment sequences." *Annals of Probability* **40** (2012), 2690–2704. DOI: https://doi.org/10.1214/11-AOP693.

[35] H. Dette and D. Tomecki. "Hankel determinants of random moment sequences." *Journal of Theoretical Probability* **30** (2017), 1539–1564. DOI: https://doi.org/10.1007/s10959-016-0699-z.

[36] I. S. Dhillon. "A New $O(n^2)$ Algorithm for the Symmetric Tridiagonal Eigenvalue/Eigenvector Problem." PhD thesis. University of California, Berkeley, 1997.

[37] R. B. Diemer and J. H. Olson. "A moment methodology for coagulation and breakage problems: Part 2—moment models and distribution reconstruction." *Chemical Engineering Science* **57** (2002). Population balance modelling of particulate systems, 2211–2228. DOI: https://doi.org/10.1016/S0009-2509(02)00112-4.

[38] C. F. Dunkl and Y. Xu. *Orthogonal Polynomials of Several Variables*. 2nd ed. Encyclopedia of Mathematics and its Applications. Cambridge University Press, 2014.

[39] J. Fang and I. A. Bolotnov. "Bubble tracking analysis of PWR two-phase flow simulations based on the level set method." *Nuclear Engineering and Design* **323** (2017), 68–77. DOI: https://doi.org/10.1016/j.nucengdes.2017.07.034.

[40] J. H. Ferziger and M. Peric. *Computational Methods for Fluid Dynamics*. Springer, 2002.

[41] F. Filbet and P. Laurençot. "Numerical simulation of the Smoluchowski coagulation equation." *SIAM Journal on Scientific Computing* **25** (2004), 2004–2028. DOI: https://doi.org/10.1137/S1064827503429132.

[42] C. Forbes, M. Evans, N. Hastings, and B. Peacock. *Statistical distributions. Fourth Edition*. John Wiley & Sons, 2011.

[43] L. Forestier-Coste and S. Mancini. "A finite volume preserving scheme on nonuniform meshes and for multidimensional coalescence." *SIAM Journal on Scientific Computing* **34** (2012), B840–B860. DOI: https://doi.org/10.1137/110847998.

[44] R. O. Fox. "A quadrature-based third-order moment method for dilute gas-particle flows." *Journal of Computational Physics* **227** (2008), 6313–6350. DOI: https://doi.org/10.1016/j.jcp.2008.03.014.

[45] R. O. Fox. *Computational Models for Turbulent Reacting Flows*. Cambridge University Press, 2003.

[46] R. O. Fox. "Introduction and fundamentals of modeling approaches for polydisperse multiphase flows." *Multiphase reacting flows: modelling and simulation*. Ed. by D. L. Marchisio and R. O. Fox. Springer, 2007, 1–40.

[47] R. O. Fox and P. Vedula. "Quadrature-based moment model for moderately dense polydisperse gas-particle flows." *Industrial & Engineering Chemistry Research* **49** (2010), 5174–5187. DOI: https://doi.org/10.1021/ie9013138.

[48] R. O. Fox. "On multiphase turbulence models for collisional fluid-particle flows." *J. Fluid Mech.* **742** (2014), 368–424. DOI: https://doi.org/10.1017/jfm.2014.21.

[49] R. O. Fox, F. Laurent, and A. Passalacqua. "The generalized quadrature method of moments." *Journal of Aerosol Science* **167** (2023), 106096. DOI: https://doi.org/10.1016/j.jaerosci.2022.106096.

[50] R. O. Fox, F. Laurent, and A. Vié. "Conditional hyperbolic quadrature method of moments for kinetic equations." *Journal of Computational Physics* **365** (2018), 269–293. DOI: https://doi.org/10.1016/j.jcp.2018.03.025.

[51] M. Frenklach. "Method of moments with interpolative closure." *Chemical Engineering Science* **57** (2002), 2229–2239. DOI: https://doi.org/10.1016/S0009-2509(02)00113-6.

[52] S. Ganesan and L. Tobiska. "An operator-splitting finite element method for the efficient parallel solution of multidimensional population balance systems." *Chemical Engineering Science* **69** (2012), 59–68. DOI: https://doi.org/10.1016/j.ces.2011.09.031.

[53] C. W. Gardiner. *Handbook of Stochastic Methods for Physics, Chemistry, and the Natural Sciences*. 2nd ed. Springer, 1985.

[54] W. Gautschi. *Orthogonal Polynomials: Computation and Approximation*. Numerical mathematics and scientific computation. Oxford University Press, 2004.

[55] B. E. Gelfand. "Droplet breakup phenomena in flows with velocity lag." *Progress in Energy and Combustion Science* **22** (1996), 201–265. DOI: https://doi.org/10.1016/S0360-1285(96)00005-6.

[56] D. T. Gillespie. "A general method for numerically simulating the stochastic time evolution of coupled chemical reactions." *Journal Computational Physics* **22** (1976), 403–434. DOI: https://doi.org/10.1016/0021-9991(76)90041-3.

[57] G. H. Golub and C. F. Van Loan. *Matrix Computations (3rd Ed.)* Johns Hopkins University Press, 1996.

[58] G. H. Golub and J. H. Welsch. "Calculation of Gauss quadrature rules." *Mathematics of Computation* **23** (1969), 221–230. DOI: https://doi.org/10.1090/S0025-5718-69-99647-1.

[59] R. G. Gordon. "Error bounds in equilibrium statistical mechanics." *Journal of Mathematical Physics* **9** (1968), 655–663. DOI: https://doi.org/10.1063/1.1664624.

[60] M. Gorokhovski and R. Zamansky. "Modeling the effects of small turbulent scales on the drag force for particles below and above the Kolmogorov scale." *Physical Review Fluids* **3** (2018), 034602. DOI: https://doi.org/10.1103/PhysRevFluids.3.034602.

[61] A. D. Gosman and E. Ioannides. "Aspects of computer simulation of liquid-fueled combustors." *Journal of Energy* **7** (1983), 482–490. DOI: https://doi.org/10.2514/3.62687.

[62] H. Grad. "On the kinetic theory of rarefied gases." *Communications on Pure and Applied Mathematics* **2** (1949), 331–407. DOI: https://doi.org/10.1002/cpa.3160020403.

[63] G. Guennebaud, B. Jacob, et al. *Eigen v3*. http://eigen.tuxfamily.org. 2010.

[64] D. R. Guildenbecher, C. López-Rivera, and P. E. Sojka. "Secondary atomization." *Experiments in Fluids* **46** (2009), 371–402. DOI: https://doi.org/10.1007/s00348-008-0593-2.

[65] B. Guo, D. F. Fletcher, and T. A. Langrish. "Simulation of the agglomeration in a spray using Lagrangian particle tracking." *Applied Mathematical Modelling* **28** (2004), 273–290. DOI: https://doi.org/10.1016/S0307-904X(03)00133-1.

[66] Y. Guo and J. S. Curtis. "Discrete Element Method Simulations for Complex Granular Flows." *Annual Review of Fluid Mechanics* **47** (2015), 21–46. DOI: https://doi.org/10.1146/annurev-fluid-010814-014644.

[67] E. Hairer, S. P. Nørsett, and G. Wanner. *Solving Ordinary Differential Equations I: Nonstiff Problems*. Springer, 1993.

[68] N. Hanchate, S. Ramani, C. Mathpati, and V. H. Dalvi. "Biomass gasification using dual fluidized bed gasification systems: A review." *Journal of Cleaner Production* **280** (2021), 123148. DOI: https://doi.org/10.1016/j.jclepro.2020.123148.

[69] C. W. Hirt and B. D. Nichols. "Volume of fluid (VOF) method for the dynamics of free boundaries." *Journal of Computational Physics* **39** (1981), 201–225. DOI: https://doi.org/10.1016/0021-9991(81)90145-5.

[70] M. J. Hounslow, R. L. Ryall, and V. R. Marshall. "A discretized population balance for nucleation, growth, and aggregation." *AIChE Journal* **34** (1988), 1821–1832. DOI: https://doi.org/10.1002/aic.690341108.

[71] L.-P. Hsiang and G. M. Faeth. "Drop deformation and breakup due to shock wave and steady disturbances." *International Journal of Multiphase Flow* **21** (1995), 545–560. DOI: https://doi.org/10.1016/0301-9322(94)00095-2.

[72] M. Jalaal and K. Mehravaran. "Transient growth of droplet instabilities in a stream." *Physics of Fluids* **26** (2014), 012101. DOI: https://doi.org/10.1063/1.4851056.

[73] E. T. Jaynes. "Information Theory and Statistical Mechanics." *Physical Review* **106** (4 1957), 620–630. DOI: https://doi.org/10.1103/PhysRev.106.620.

[74] V. John, I. Angelov, A. Öncül, and D. Thévenin. "Techniques for the reconstruction of a distribution from a finite number of its moments." *Chemical Engineering Science* **62** (2007), 2890–2904. DOI: https://doi.org/10.1016/j.ces.2007.02.041.

[75] V. John, T. Mitkova, M. Roland, K. Sundmacher, L. Tobiska, and A. Voigt. "Simulations of population balance systems with one internal coordinate using finite element methods." *Chemical Engineering Science* **64** (2009), 733–741. DOI: https://doi.org/10.1016/j.ces.2008.05.004.

[76] V. John and F. Thein. "On the efficiency and robustness of the core routine of the quadrature method of moments (QMOM)." *Chemical Engineering Science* **75** (2012), 327–333. DOI: https://doi.org/10.1016/j.ces.2012.03.024.

[77] D. Kah, F. Laurent, M. Massot, and S. Jay. "A high order moment method simulating evaporation and advection of a polydisperse liquid spray." *Journal of Computational Physics* **231** (2012), 394–422. DOI: https://doi.org/10.1016/j.jcp.2011.08.032.

[78] N. G. van Kampen. "Itô versus Stratonovich." *Journal of Statistical Physics* **24** (1981), 175–187. DOI: https://doi.org/10.1007/BF01007642.

[79] I. Khan, M. Wang, Y. Zhang, W. Tian, G. Su, and S. Qiu. "Two-phase bubbly flow simulation using CFD method: A review of models for interfacial forces." *Progress in Nuclear Energy* **125** (2020), 103360. DOI: https://doi.org/10.1016/j.pnucene.2020.103360.

[80] F. E. Kruis, K. A. Kusters, S. E. Pratsinis, and B. Scarlett. "A Simple Model for the Evolution of the Characteristics of Aggregate Particles Undergoing Coagulation and Sintering." *Aerosol Science and Technology* **19** (1993), 514–526. DOI: https://doi.org/10.1080/02786829308959656.

[81] S. A. Krzeczkowski. "Measurement of liquid droplet disintegration mechanisms." *International Journal of Multiphase Flow* **6** (1980), 227–239. DOI: https://doi.org/10.1016/0301-9322(80)90013-0.

[82] V. Kulkarni and P. E. Sojka. "Bag breakup of low viscosity drops in the presence of a continuous air jet." *Physics of Fluids* **26** (2014), 072103. DOI: https://doi.org/10.1063/1.4887817.

[83] H. J. Kull. "Theory of the Rayleigh-Taylor instability." *Physics Reports* **206** (1991), 197–325. DOI: https://doi.org/10.1016/0370-1573(91)90153-D.

[84] S. Laín and M. Sommerfeld. "Numerical calculation of pneumatic conveying in horizontal channels and pipes: Detailed analysis of conveying behaviour." *International Journal of Multiphase Flow* **39** (2012), 105–120. DOI: https://doi.org/10.1016/j.ijmultiphaseflow.2011.09.006.

[85] F. Laurent and T. T. Nguyen. "Realizable second-order finite-volume schemes for the advection of moment sets of the particle size distribution." *Journal of Computational Physics* **337** (2017), 309–338. DOI: https://doi.org/10.1016/j.jcp.2017.02.046.

[86] D. Laurie. "Anti-Gaussian quadrature formulas." *Mathematics of Computation* **65** (1996), 739–747. DOI: https://doi.org/10.1090/S0025-5718-96-00713-2.

[87] R. J. LeVeque. *Finite Volume Methods for Hyperbolic Problems*. Cambridge Texts in Applied Mathematics. Cambridge University Press, 2002.

[88] R. W. Lewis, P. Nithiarasu, and K. N. Seetharamu. *Fundamentals of the Finite Element Method for Heat and Fluid Flow*. John Wiley & Sons, 2004.

[89] D. Li, Z. Gao, A. Buffo, W. Podgorska, and D. L. Marchisio. "Droplet breakage and coalescence in liquid-liquid dispersions: Comparison of different kernels with EQMOM and QMOM." *AIChE J.* **63** (2017), 2293–2311. DOI: https://doi.org/10.1002/aic.15557.

[90] Y. Liao and D. Lucas. "A literature review of theoretical models for drop and bubble breakup in turbulent dispersions." *Chemical Engineering Science* **64** (2009), 3389–3406. DOI: https://doi.org/10.1016/j.ces.2009.04.026.

[91] Y. Liao and D. Lucas. "A literature review on mechanisms and models for the coalescence process of fluid particles." *Chem. Eng. Sci.* **65** (2010), 2851–2864. DOI: https://doi.org/10.1016/j.ces.2010.02.020.

[92] J. D. Lister, D. J. Smit, and M. J. Hounslow. "Adjustable discretized population balance for growth and aggregation." *AIChE Journal* **41** (1995), 591–603. DOI: https://doi.org/10.1002/aic.690410317.

[93] E. Madadi-Kandjani, R. O. Fox, and A. Passalacqua. "Application of the Fokker-Planck molecular mixing model to turbulent scalar mixing using moment methods." *Physics of Fluids* **29** (2017), 065109. DOI: https://doi.org/10.1063/1.4989421.

[94] E. Madadi-Kandjani and A. Passalacqua. "An extended quadrature-based moment method with log-normal kernel density functions." *Chemical Engineering Science* **131** (2015), 323–339. DOI: https://doi.org/10.1016/j.ces.2015.04.005.

[95] A. W. Mahoney and D. Ramkrishna. "Efficient solution of population balance equations with discontinuities by finite elements." *Chemical Engineering Science* **57** (2002), 1107–1119. DOI: https://doi.org/10.1016/S0009-2509(01)00427-4.

[96] D. L. Marchisio and R. O. Fox. *Computational Models for Polydisperse Particulate and Multiphase Systems*. Cambridge University Press, 2013.

[97] D. L. Marchisio. "Quadrature method of moments for poly-disperse flows." *Multiphase reacting flows: modelling and simulation*. Ed. by D. L. Marchisio and R. O. Fox. Springer, 2007, 41–77.

[98] D. L. Marchisio and R. O. Fox. "Solution of population balance equations using the direct quadrature method of moments." *Journal of Aerosol Science* **36** (2005), 43–73. DOI: https://doi.org/10.1016/j.jaerosci.2004.07.009.

[99] D. L. Marchisio, J. T. Pikturna, R. O. Fox, R. D. Vigil, and A. A. Barresi. "Quadrature method of moments for population-balance equations." *AIChE Journal* **49** (2003), 1266–1276. DOI: https://doi.org/10.1002/aic.690490517.

[100] D. L. Marchisio, R. D. Vigil, and R. O. Fox. "Quadrature method of moments for aggregation-breakage processes." *Journal of Colloid and Interface Science* **258** (2003), 322–334. DOI: https://doi.org/10.1016/S0021-9797(02)00054-1.

[101] M. Massot, F. Laurent, D. Kah, and S. de Chaisemartin. "A Robust Moment Method for Evaluation of the Disappearance Rate of Evaporating Sprays." *SIAM Journal on Applied Mathematics* **70** (2010), 3203–3234. DOI: https://doi.org/10.1137/080740027.

[102] K. Masters. *Spray Drying: An Introduction to Principles, Operational Practice and Applications*. Chemical and Process Engineering Series. L. Hill, 1972.

[103] S. Matveev, A. Smirnov, and E. Tyrtyshnikov. "A fast numerical method for the Cauchy problem for the Smoluchowski equation." *Journal of Computational Physics* **282** (2015), 23–32. DOI: https://doi.org/10.1016/j.jcp.2014.11.003.

[104] S. A. Matveev, D. A. Zheltkov, E. E. Tyrtyshnikov, and A. P. Smirnov. "Tensor train versus Monte Carlo for the multicomponent Smoluchowski coagulation equation." *Journal of Computational Physics* **316** (2016), 164–179. DOI: https://doi.org/10.1016/j.jcp.2016.04.025.

[105] L. Mazzei, D. L. Marchisio, and P. Lettieri. "New quadrature-based moment method for the mixing of inert polydisperse fluidized powders in commercial CFD codes." *AIChE Journal* **58** (2012), 3054–3069. DOI: https://doi.org/10.1002/aic.13714.

[106] J. McDonald and M. Torrilhon. "Affordable robust moment closures for CFD based on the maximum-entropy hierarchy." *Journal of Computational Physics* **251** (2013), 500–523. DOI: https://doi.org/10.1016/j.jcp.2013.05.046.

[107] R. McGraw. "Description of aerosol dynamics by the quadrature method of moments." *Aerosol Science and Technology* **27** (1997), 255–265. DOI: https://doi.org/10.1080/02786829708965471.

[108] L. R. Mead and N. Papanicolaou. "Maximum entropy in the problem of moments." *Journal of Mathematical Physics* **25** (1984), 2404–2417. DOI: https://doi.org/10.1063/1.526446.

[109] E. Michaelides, C. T. Crowe, and J. D. Schwarzkopf, eds. *Multiphase Flow Handbook, Second Edition*. CRC Press, 2016.

[110] E. Michaelides, B. van Wachem, and M. Sommerfeld. *Multiphase Flows with Droplets and Particles, Third Edition*. CRC Press, 2022.

[111] J. W. Miles. "On the generation of surface waves by shear flows Part 3. Kelvin-Helmholtz instability." *Journal of Fluid Mechanics* **6** (1959), 583–598. DOI: https://doi.org/10.1017/S0022112059000842.

[112] J.-P. Minier. "A methodology to devise consistent probability density function models for particle dynamics in turbulent dispersed two-phase flows." *Physics of Fluids* **33** (2021), 023312. DOI: https://doi.org/10.1063/5.0039249.

[113] J.-P. Minier and E. Peirano. "The pdf approach to turbulent polydispersed two-phase flows." *Physics Reports* **352** (2001), 1–214. DOI: https://doi.org/10.1016/S0370-1573(01)00011-4.

[114] A. Mukhopadhyay, G. Jasor, and W. Polifke. "Simulation of pure sedimentation of raindrops using quadrature method of moments." *Atmospheric Research* **106** (2012), 61–70. DOI: https://doi.org/10.1016/j.atmosres.2011.11.008.

[115] T. T. Nguyen, F. Laurent, R. O. Fox, and M. Massot. "Solution of population balance equations in applications with fine particles: Mathematical modeling and numerical schemes." *Journal Computational Physics* **325** (2016), 129–156. DOI: https://doi.org/10.1016/j.jcp.2016.08.017.

[116] J. A. Nicholls. *Stream and droplet breakup by shock waves.* Tech. rep. NASA SP-194, 1972, 126–128.

[117] S. Osher and J. A. Sethian. "Fronts propagating with curvature-dependent speed: algorithms based on Hamilton-Jacobi formulations." *Journal of Computational Physics* **79** (1988), 12–49. DOI: https://doi.org/10.1016/0021-9991(88)90002-2.

[118] P. Ostermeier, F. Fischer, S. Fendt, S. DeYoung, and H. Spliethoff. "Coarse-grained CFD-DEM simulation of biomass gasification in a fluidized bed reactor." *Fuel* **255** (2019), 115790. DOI: https://doi.org/10.1016/j.fuel.2019.115790.

[119] D. L. Otten and P. Vedula. "A quadrature based method of moments for nonlinear Fokker-Planck equations." *Journal of Statistical Mechanics: Theory and Experiment* **2011** (2011), P09031. DOI: https://doi.org/10.1088/1742-5468/2011/09/P09031.

[120] V. Y. Pan. "How bad are Vandermonde matrices?" *SIAM Journal on Matrix Analysis and Applications* **37** (2016), 676–694. DOI: https://doi.org/10.1137/15M1030170.

[121] B. N. Parlett and I. S. Dhillon. "Relatively robust representations of symmetric tridiagonals." *Linear Algebra and its Applications* **309** (2000), 121–151. DOI: https://doi.org/10.1016/S0024-3795(99)00262-1.

[122] R. G. Patel, O. Desjardins, and R. O. Fox. "Three-dimensional conditional hyperbolic quadrature method of moments." *Journal of Computational Physics: X* **1** (2019), 100006. DOI: https://doi.org/10.1016/j.jcpx.2019.100006.

[123] E. Peirano, S. Chibbaro, J. Pozorski, and J. P. Minier. "Mean-field/PDF numerical approach for polydispersed turbulent two-phase flows." *Prog. Energy Combust. Sci.* **32** (2006), 315–371. DOI: https://doi.org/10.1016/j.pecs.2005.07.002.

[124] M. Petitti et al. "Bubble size distribution modeling in stirred gas–liquid reactors with QMOM augmented by a new correction algorithm." *AIChE Journal* **56** (2010), 36–53. DOI: https://doi.org/10.1002/aic.12003.

[125] M. Pigou, J. Morchain, P. Fede, M.-I. Penet, and G. Laronze. "An assessment of methods of moments for the simulation of population dynamics in large-scale bioreactors." *Chemical Engineering Science* **171** (2017), 218–232. DOI: https://doi.org/10.1016/j.ces.2017.05.026.

[126] M. Pigou, J. Morchain, P. Fede, M.-I. Penet, and G. Laronze. "New developments of the Extended Quadrature Method of Moments to solve Population Balance Equations." *Journal of Computational Physics* **365** (2018), 243–268. DOI: https://doi.org/10.1016/j.jcp.2018.03.027.

[127] M. Pilch and C. A. Erdman. "Use of breakup time data and velocity history data to predict the maximum size of stable fragments for acceleration-induced breakup of a liquid drop." *International Journal of Multiphase Flow* **13** (1987), 741–757. DOI: https://doi.org/10.1016/0301-9322(87)90063-2.

[128] E. B. Pitman, C. C. Nichita, A. Patra, A. Bauer, M. Sheridan, and M. Bursik. "Computing granular avalanches and landslides." *Physics of Fluids* **15** (2003), 3638. DOI: https://doi.org/10.1063/1.1614253.

[129] S. Poljak and J. Rohn. "Checking robust nonsingularity is NP-hard." *Mathematics of Control, Signals, and Systems* **6** (1993), 1–9. DOI: https://doi.org/10.1007/BF01213466.

[130] M. Pollack, S. Salenbauch, D. L. Marchisio, and C. Hasse. "Bivariate extensions of the Extended Quadrature Method of Moments (EQMOM) to describe coupled droplet evaporation and heat-up." *Journal of Aerosol Science* **92** (2016), 53–69. DOI: https://doi.org/10.1016/j.jaerosci.2015.10.008.

[131] M. Pollack. "Quadrature based moment methods for sprays and turbulent premixed combustion." PhD thesis. TU Darmstadt, 2021.

[132] M. Pollack, F. Ferraro, J. Janicka, and C. Hasse. "Evaluation of Quadrature-based Moment Methods in turbulent premixed combustion." *Proceedings of the Combustion Institute* **38** (2021), 2877–2884. DOI: https://doi.org/10.1016/j.proci.2020.06.127.

[133] M. Pollack, M. Pütz, D. L. Marchisio, M. Oevermann, and C. Hasse. "Zero-flux approximations for multivariate quadrature-based moment methods." *Journal of Computational Physics* **398** (2019), 108879. DOI: https://doi.org/10.1016/j.jcp.2019.108879.

[134] S. B. Pope. *Turbulent Flows.* Cambridge University Press, 2000.

[135] J. Pozorski and J.-P. Minier. "Probability density function modeling of dispersed two-phase turbulent flows." *Physical Review E* **59** (1999), 855–863. DOI: https://doi.org/10.1103/PhysRevE.59.855.

[136] D. Ramkrishna. *Population Balances: Theory and Applications to Particulate Systems in Engineering.* Academic Press, 2000.

[137] L. E. Reichl. *A Modern Course in Statistical Physics, 2nd Edition.* John Wiley & Sons, 1998.

[138] R. D. Reitz and R. Diwakar. "Effect of drop breakup on fuel sprays." *SAE Technical Paper 860469* (1986). DOI: https://doi.org/10.4271/860469.

[139] R. D. Reitz and R. Diwakar. "Structure of high-pressure fuel sprays." *SAE Technical Paper 870598* (1987). DOI: https://doi.org/10.4271/870598.

[140] H. Risken. *The Fokker-Planck Equation: Methods of Solution and Applications Second Edition.* 2nd ed. Springer, 1989.

[141] H. Rutishauser. "Der Quotienten-Differenzen-Algorithmus." *Zeitschrift für angewandte Mathematik und Physik (ZAMP)* **5** (1954), 233–251.

[142] M. Sabat. "Eulerian modeling and numerical methods for the description of turbulent polydisperse sprays." PhD thesis. Université Paris-Saclay, 2016.

[143] R. A. Sack and A. F. Donovan. "An algorithm for Gaussian quadrature given modified moments." *Numerische Mathematik* **18** (1972), 465–478. DOI: https://doi.org/10.1007/BF01406683.

[144] P. Sagaut. *Large Eddy Simulation for Incompressible Flows.* Springer, 2006.

[145] S. Salenbauch, A. Cuoci, A. Frassoldati, C. Saggese, T. Faravelli, and C. Hasse. "Modeling soot formation in premixed flames using an Extended Conditional Quadrature Method of Moments." *Combustion and Flame* **162** (2015), 2529–2543. DOI: https://doi.org/10.1016/j.combustflame.2015.03.002.

[146] K. Schmüdgen. *The Moment Problem*. Vol. 277. Graduate Texts in Mathematics. Springer, 2017.

[147] M. Shiea, A. Buffo, M. Vanni, and D. L. Marchisio. "A novel finite-volume TVD scheme to overcome non-realizability problem in quadrature-based moment methods." *Journal of Computational Physics* **409** (2020), 109337. DOI: https://doi.org/10.1016/j.jcp.2020.109337.

[148] J. A. Shohat, J. D. Tamarkin, and A. M. Society. *The Problem of Moments*. Mathematical Surveys and Monographs. American Mathematical Society, 1943.

[149] C.-W. Shu and S. Osher. "Efficient implementation of essentially non-oscillatory shock-capturing schemes." *Journal Computational Physics* **77** (1988), 439–471. DOI: https://doi.org/10.1016/0021-9991(88)90177-5.

[150] B. Simon. "The Classical Moment Problem as a Self-Adjoint Finite Difference Operator." *Advances in Mathematics* **137** (1998), 82–203. DOI: https://doi.org/10.1006/aima.1998.1728.

[151] M. Singh, V. Ranade, O. Shardt, and T. Matsoukas. "Challenges and opportunities concerning numerical solutions for population balances: a critical review." *Journal of Physics A: Mathematical and Theoretical* **55** (2022), 383002. DOI: https://doi.org/10.1088/1751-8121/ac8a42.

[152] J. Solsvik and H. A. Jakobsen. "The Foundation of the Population Balance Equation: A Review." *Journal of Dispersion Science and Technology* **36** (2015), 510–520. DOI: https://doi.org/10.1080/01932691.2014.909318.

[153] L. A. Spielman and O. Levenspiel. "A Monte Carlo treatment for reacting and coalescing dispersed phase systems." *Chemical Engineering Science* **20** (1965), 247–254. DOI: https://doi.org/10.1016/0009-2509(65)80035-5.

[154] M. Strumendo and H. Arastoopour. "Solution of Bivariate Population Balance Equations Using the Finite Size Domain Complete Set of Trial Functions Method of Moments (FCMOM)." *Industrial & Engineering Chemistry Research* **48** (2009), 262–273. DOI: https://doi.org/10.1021/ie800272a.

[155] M. Strumendo and H. Arastoopour. "Solution of PBE by MOM in finite size domains." *Chemical Engineering Science* **63** (2008), 2624–2640. DOI: https://doi.org/10.1016/j.ces.2008.02.010.

[156] M. Strumendo and H. Arastoopour. "Solution of Population Balance Equations by the Finite Size Domain Complete Set of Trial Functions Method of Moments (FCMOM) for Inhomogeneous Systems." *Industrial & Engineering Chemistry Research* **49** (2010), 5222–5230. DOI: https://doi.org/10.1021/ie901407x.

[157] S. Subramaniam. "Lagrangian–Eulerian methods for multiphase flows." *Progress in Energy and Combustion Science* **39** (2013), 215–245. DOI: https://doi.org/10.1016/j.pecs.2012.10.003.

[158] P.-Y. C. Taunay and M. E. Mueller. "Quadrature-based moment methods for kinetic plasma simulations." *Journal of Computational Physics* **473** (2023), 111700. DOI: https://doi.org/10.1016/j.jcp.2022.111700.

[159] T. G. Theofanous. "Aerobreakup of Newtonian and viscoelastic liquids." *Annual Review of Fluid Mechanics* **43** (2011), 661–690. DOI: https://doi.org/10.1146/annurev-fluid-122109-160638.

[160] T. G. Theofanous and G. J. Li. "On the physics of aerobreakup." *Physics of fluids* **20** (2008), 052103. DOI: https://doi.org/10.1063/1.2907989.

[161] T. G. Theofanous, V. V. Mitkin, C. L. Ng, C. H. Chang, X. Deng, and S. Sushchikh. "The physics of aerobreakup. II. Viscous liquids." *Physics of Fluids* **24** (2012), 022104. DOI: https://doi.org/10.1063/1.3680867.

[162] M. Uhlmann. "An immersed boundary method with direct forcing for the simulation of particulate flows." *Journal of Computational Physics* **209** (2005), 448–476. DOI: https://doi.org/10.1016/j.jcp.2005.03.017.

[163] R. E. M. Verdurmen et al. "Simulation of Agglomeration in Spray Drying Installations: The EDECAD Project." *Drying Technology* **22** (2004), 1403–1461. DOI: https://doi.org/10.1081/DRT-120038735.

[164] H. K. Versteeg and W. Malalasekera. *An Introduction to Computational Fluid Dynamics: The Finite Volume Method*. Pearson Education, 2007.

[165] A. Vié, F. Doisneau, and M. Massot. "On the Anisotropic Gaussian Velocity Closure for Inertial-Particle Laden Flows." *Communications in Computational Physics* **17** (2015), 1–46. DOI: https://doi.org/10.4208/cicp.021213.140514a.

[166] V. Vikas, Z. J. Wang, and R. O. Fox. "Realizable high-order finite-volume schemes for quadrature-based moment methods applied to diffusion population balance equations." *Journal of Computational Physics* **249** (2013), 162–179. DOI: https://doi.org/10.1016/j.jcp.2013.05.002.

[167] V. Vikas, Z. J. Wang, A. Passalacqua, and R. O. Fox. "Realizable high-order finite-volume schemes for quadrature-based moment methods." *Journal of Computational Physics* **230** (2011), 5328–5352. DOI: https://doi.org/10.1016/j.jcp.2011.03.038.

[168] M. Visone, M. Lanzetta, M. Lappa, C. Lanzaro, and L. Polizio. "Three-dimensional simulation of clouds of multi-disperse evaporating saliva droplets in a train cabin." *Physics of Fluids* **33** (2021), 083318. DOI: https://doi.org/10.1063/5.0059649.

[169] J. Werther. "Fluidized-Bed Reactors." *Ullmann's Encyclopedia of Industrial Chemistry*. John Wiley & Sons, 2007, 319–366. DOI: https://doi.org/10.1002/14356007.b04_239.pub2.

[170] J. C. Wheeler. "Modified moments and Gaussian quadratures." *Rocky Mountain Journal of Mathematics* **4** (1974), 287–296. DOI: https://doi.org/10.1216/RMJ-1974-4-2-287.

[171] D. Wilcox. *Turbulence Modeling for CFD*. DCW Industries, 2006.

[172] H. S. Wilf. *Mathematics for the Physical Sciences*. John Wiley & Sons, 1962.

[173] D. L. Wright. "Numerical advection of moments of the particle size distribution in Eulerian models." *Journal of Aerosol Science* **38** (2007), 352–369. DOI: https://doi.org/10.1016/j.jaerosci.2006.11.011.

[174] M. Yamakawa, A. Kitagawa, K. Ogura, Y. M. Chung, and M. Kim. "Computational investigation of prolonged airborne dispersion of novel coronavirus-laden droplets." *Journal of Aerosol Science* **155** (2021), 105769. DOI: https://doi.org/10.1016/j.jaerosci.2021.105769.

[175] M. Yang, S. M. Mousavi, H. Fatehi, and X.-S. Bai. "Numerical simulation of biomass gasification in fluidized bed gasifiers." *Fuel* **337** (2023), 127104. DOI: https://doi.org/10.1016/j.fuel.2022.127104.

[176] Y. Yang, Y. Wang, C. Su, X. Yuan, X. Liu, and Z. Chen. "A rapid method for prediction of airborne disease infection risks in an intercity bus." *Physics of Fluids* **34** (2022), 083323. DOI: https://doi.org/10.1063/5.0107895.

[177] C. Yoon and R. McGraw. "Representation of generally mixed multivariate aerosols by the quadrature method of moments: I. Statistical foundation." *Journal of Aerosol Science* **35** (2004), 561–576. DOI: https://doi.org/10.1016/j.jaerosci.2003.11.003.

[178] C. Yuan and R. O. Fox. "Conditional quadrature method of moments for kinetic equations." *Journal of Computational Physics* **230** (2011), 8216–8246. DOI: https://doi.org/10.1016/j.jcp.2011.07.020.

[179] C. Yuan, F. Laurent, and R. O. Fox. "An extended quadrature method of moments for population balance equations." *Journal of Aerosol Science* **51** (2012), 1–23. DOI: https://doi.org/10.1016/j.jaerosci.2012.04.003.

[180] H. Zhao, H.-F. Liu, W.-F. Li, and J.-L. Xu. "Morphological classification of low viscosity drop bag breakup in a continuous air jet stream." *Physics of Fluids* **22** (2010), 114103. DOI: https://doi.org/10.1063/1.3490408.

[181] H. Zhao, H.-F. Liu, J.-L. Xu, W.-F. Li, and K.-F. Lin. "Temporal properties of secondary drop breakup in the bag-stamen breakup regime." *Physics of Fluids* **25** (2013), 054102. DOI: https://doi.org/10.1063/1.4803154.

Nomenclature

Acronyms and abbreviations

BI	Bisection with inverse iteration
CQMOM	Conditional quadrature method of moments
DC	Divide & Conquer
DEM	Discrete element method
DNS	Direct numerical simulation
DQMOM	Direct quadrature method of moments
EQMOM	Extended quadrature method of moments
FCMOM	Finite-size domain complete set of trial functions method of moments
FLOP	Floating point operation
GPBE	Generalized population balance equation
GWA	Golub-Welsch algorithm
GaG	Gauss/anti-Gauss
KDEM	Kernel density element method
KDF	Kernel density function
LES	Large eddy simulation
LHS	Left-hand side
LQMDA	Long quotient-modified difference algorithm
MOMIC	Method of moments with interpolative closure
NDF	Number density function
PBE	Population balance equation

PDA	Product-difference algorithm
PDE	Partial differential equation
PDF	Probability density function
QBMM	Quadrature-based moment method
QDA	Quotient-difference algorithm
QMOM	Quadrature method of moments
RANS	Reynolds-averaged Navier-Stokes
RHS	Right-hand side
RK2SSP	Second-order strong-stability preserving Runge-Kutta
RKSSP	Strong-stability preserving Runge-Kutta
RRR	Relatively robust representations
SDE	Stochastic differential equation
SGS	Subgrid scale

Variables, functions, constants

$\mathcal{B}_k$	Breakup in the kth moment equation
C_{bag}	Reitz-Diwakar model constant for bag breakup limit
C_d	Drag coefficient
C_{shear}	Reitz-Diwakar model constant for shear breakup limit
C_t	Model constant for turbulence-induced phase space diffusion model
$\mathbf{C}(\cdot)$	Physical diffusion coefficient matrix
D_{bag}	Reitz-Diwakar model constant for bag breakup rate
D_{shear}	Reitz-Diwakar model constant for shear breakup rate
$\mathbf{D}(\cdot)$	Diffusivity matrix in internal-coordinate space
$G_n(\cdot)$	n-point Gaussian quadrature
$\text{Gamma}(\cdot)$	Gamma distribution
$I(\cdot)$	Integral functional defined in (3.15)

$\mathbf{J}_n$	Truncated Jacobi matrix of size n
$\mathbf{J}_n^*$	Modified (anti-Gauss) truncated Jacobi matrix of size n
M_k	Absolute moment of order k
$\mathbf{M}_n$	Hankel moment matrix of size n
N	Number of internal-coordinates
N_p	Number of particles
$\mathcal{N}(\cdot)$	Normal distribution
$\mathcal{Q}_k(\cdot)$	Quadrature approximation of the collision source term in the kth moment equation
$R_n(\cdot)$	Error of n-point quadrature rule
$\mathcal{S}(\cdot)$	Source term in the PBE for discontinuous processes
$\boldsymbol{U}$	Lagrangian fluid velocity
$\overline{\boldsymbol{U}}$	Lagrangian resolved fluid velocity
$\boldsymbol{U}'$	Lagrangian turbulent fluid velocity fluctuation
V	Lagrangian particle velocity (1D)
$\boldsymbol{V}$	Lagrangian particle velocity
W	1D-Wiener process with increment dW
$\boldsymbol{W}$	Wiener process with increment d$\boldsymbol{W}$
$\boldsymbol{X}$	Lagrangian particle position
$a(\cdot)$	Particle acceleration (1D); phase-space advection velocity (1D)
$a^*(\cdot)$	Noise-induced advection function in Fokker-Planck equation (1D)
$\boldsymbol{a}(\cdot)$	Particle acceleration; phase-space advection velocity
$\boldsymbol{a}^*(\cdot)$	Noise-induced advection function in Fokker-Planck equation
$\mathrm{erf}(\cdot)$	Error function
d	Particle diameter
$d(\cdot)$	Diffusivity in phase space (1D)
k_t	Turbulent kinetic energy
$f(\cdot)$	NDF
$f_{st}(\cdot)$	Steady-state NDF

l_0	Integral length scale
l_t	Characteristic turbulence length scale
m_k	Moment of order k
$m_{k_1,k_2,\ldots,k_N}$	Multivariate moment of order $(k_1, k_2, \ldots, k_N)$
$\dot{m}_k$	Moment source term of order k
$\dot{m}_{k_1,k_2,\ldots,k_N}$	Multivariate moment source term of order $(k_1, k_2, \ldots, k_N)$
$\tilde{m}_k(\cdot)$	Moment of normal distribution
$\boldsymbol{m}_p$	Sequence of integer moments up to order p
$p_k(\cdot)$	General polynomial of degree k
$p_i^{(1)}(\cdot)$	One-particle PDF of ith particle
$p^{(N_p)}(\cdot)$	N_p-particle PDF
$r_{\text{reg}}(\cdot)$	Radius of regularity
s_{ij}	Mixed moments used in the LQMDA / Wheeler algorithm
$\text{sgn}(\cdot)$	Sign function
t	Time
u	Fluid velocity (1D)
$\boldsymbol{u}$	Fluid velocity
$\bar{\boldsymbol{u}}$	Resolved fluid velocity
$\boldsymbol{u'}$	Turbulent fluid velocity fluctuation
u_r	Relative velocity
v	Phase-space variable for particle velocity (1D)
$w(\cdot)$	General weight function of orthogonal polynomials
w_j	The jth weight of a quadrature rule
$\boldsymbol{v}$	Phase-space variable for particle velocity vector; general advection velocity
$\boldsymbol{x}$	Point in physical space
$\Gamma(\cdot)$	The gamma function
Δ	LES filter width
Δt	Time step size

$\Theta(\cdot)$	Heaviside step function
$\boldsymbol{\Xi}$	Random variable in internal-coordinate space
$\boldsymbol{\Sigma}(\cdot)$	Noise coefficient matrix in 3D-Langevin equation
α_k	Recurrence coefficient of orthogonal polynomials
$\beta(\cdot)$	Fragment size distribution from breakup
β_k	Recurrence coefficient of orthogonal polynomials
γ	Advection constant in Fokker-Planck equation
$\delta(\cdot)$	Dirac delta function
$\delta_\sigma(\cdot)$	KDF with parameter σ used by the EQMOM
ϵ_t	Turbulent energy dissipation rate
η	Kolmogorov length scale
$\nu(\cdot)$	Breakup rate
ν_e	Effective viscosity
ν_f	Kinematic fluid viscosity
ν_t	Eddy viscosity
ξ	Internal coordinate
$\hat{\xi}_{\text{bag}}$	Critical droplet size for bag breakup
$\hat{\xi}_{\text{shear}}$	Critical droplet size for shear breakup
$\boldsymbol{\xi}$	Internal coordinate vector
$\pi_k(\cdot)$	Monic orthogonal polynomial of degree k
$\tilde{\pi}_k(\cdot)$	Orthonormal polynomial of degree k
ρ_f	Fluid density
ρ_p	Particle density (specific mass)
σ	KDF parameter used by the EQMOM
$\sigma(\cdot)$	Noise function in the 1D-Langevin equation
σ_l	Liquid surface tension
τ_{bag}	Droplet lifetime in the bag breakup regime
τ_{shear}	Droplet lifetime in the shear breakup regime
τ_t	Characteristic turbulence time scale

τ_p	Characteristic particle time scale
ϕ	Diffusion constant in Fokker-Planck equation

Sets, spaces, fields

$\mathbb{B}$	General support interval / field
$\mathcal{M}_p$	The pth moment space
$\partial\mathcal{M}_p$	Boundary of the pth moment space
$\mathcal{P}_n$	Set of real polynomials with degree up to n
$\mathbb{R}$	Set/field of real numbers
Ω	Internal-coordinate space

Superscripts and subscripts

$\|^A$	Anti-Gaussian quadrature
$\|^G$	Gaussian quadrature
$\|_f$	Fluid
$\|_p$	Particle
$\|_t$	Turbulence

Dimensionless numbers

Oh	Ohnesorge number
Re	Reynolds number
$\mathrm{Re_p}$	Particle Reynolds number
St	Stokes number
We	Weber number

List of Figures

List of Tables

A. Appendix

A.1. Python Implementation of QBMMs

The numerical studies in Chapters 4 and 5 were carried out using the Python package *QuadMomPy*, which has been developed by the author as part of this work. The source code is available on

- GitLab: *https://gitlab.com/puetzm/quadmompy*,
- GitHub (mirror): *https://github.com/puetzmi/quadmompy*.

The versions used for the numerical investigations were

- version *v0.9.10* (Git commit hash *01f87b0*) in Chapter 4,
- version *v0.9.8* (Git commit hash *f9aa049*) in Chapter 5.

The basic configurations for the study in Chapter 5 are also included as examples in the code repository.

A.2. Supplementary Results for the Numerical Investigation of Droplet Breakup

In addition to the results presented in Section 4.4, Figure A.1 shows the evolution of the Sauter mean diameter (SMD) and the relative error over time, employing the Gamma-EQMOM with different numbers of quadrature nodes. Using 100 instead of 10 second quadrature nodes does not lead to any visible improvement.

Figure A.2 shows the SMD and the relative error resulting from the QMOM with up to 16 moments. The results display the general expected trend that raising the number of moments leads to increased accuracy.

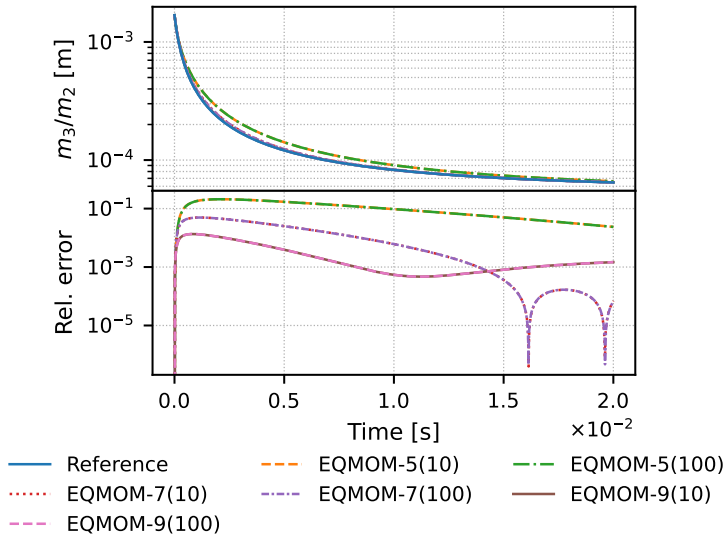

Figure A.1.: SMD (top) and relative error (bottom) for Case 3, using the Gamma-EQMOM with different numbers of second quadrature nodes.

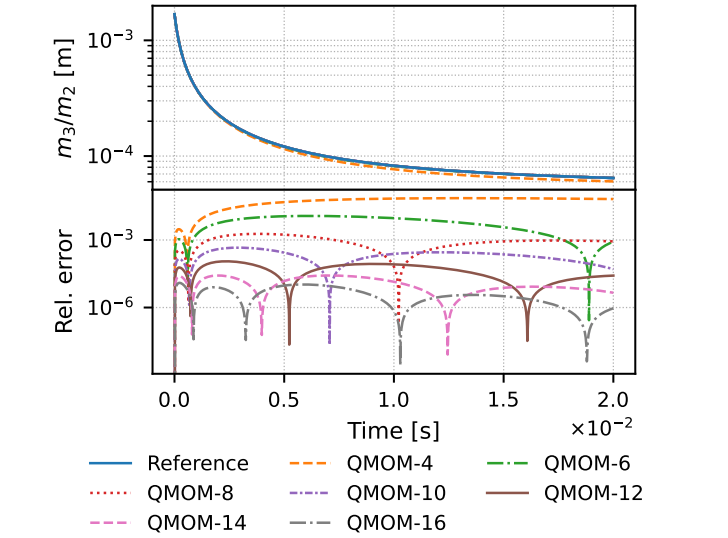

Figure A.2.: SMD (top) and relative error (bottom) for Case 3 using the QMOM with up to 16 moments.

A.3. Central Absolute Moments of the Normal Distribution

It is commonly known that a normal distribution with mean μ and standard deviation s has the probability density function

$$p(x;\mu,s) = \frac{1}{\sqrt{2\pi}s}\exp\left(-\frac{1}{2}\frac{(x-\mu)^2}{s^2}\right). \tag{A.1}$$

With $\mu = 0$ the raw absolute moments are equal to the central absolute moments. Considering the symmetry about the origin, they can be expressed as

$$\begin{aligned} M_k &= \int_{-\infty}^{\infty} |x|^k \, p(x;0,s)\,\mathrm{d}x = 2\int_0^{\infty} x^k p(x;0,s)\,\mathrm{d}x \\ &= \frac{\sqrt{2}}{\sqrt{\pi}s}\int_0^{\infty} x^k \exp\left(-\frac{1}{2}\frac{x^2}{s^2}\right)\mathrm{d}x. \end{aligned} \tag{A.2}$$

According to [17] the analytical expression for the integral is

$$\int_0^{\infty} x^k \exp\left(-\frac{1}{2}\frac{x^2}{s^2}\right)\mathrm{d}x = \frac{1}{2}\,\Gamma\left(\frac{k+1}{2}\right)\left(2s^2\right)^{(k+1)/2} \tag{A.3}$$

Then the kth central absolute moment can finally be written as

$$M_k = \frac{s^k 2^{k/2}}{\sqrt{\pi}}\,\Gamma\left(\frac{k+1}{2}\right). \tag{A.4}$$

A.4. Analytical Solution of the Stationary Fokker-Planck Equation

Let $\mathcal{A}(v)$ denote the advection function, which includes the drift-induced advection as well as the noise-induced advection and $\mathcal{B}(v)$ the diffusion function. Then the Fokker-Planck equation reads

$$\frac{\partial f(v)}{\partial t} = -\frac{\partial}{\partial v}\left[\mathcal{A}(v)f(v)\right] + \frac{1}{2}\frac{\partial^2}{\partial v^2}\left[\mathcal{B}(v)f(v)\right]. \tag{A.5}$$

Setting $\partial f(v;t)/\partial t = 0$, the stationary NDF $f_{st}(v)$ satisfies

$$2\,\frac{\mathrm{d}}{\mathrm{d}v}\left[\mathcal{A}(v)f_{st}(v)\right] = \frac{\mathrm{d}^2}{\mathrm{d}v^2}\left[\mathcal{B}(v)f_{st}(v)\right]. \tag{A.6}$$

Integration with respect to v yields

$$2\mathcal{A}(v)f_{st}(v) + C_1 = \frac{\mathrm{d}}{\mathrm{d}v}\left[\mathcal{B}(v)f_{st}(v)\right], \tag{A.7}$$

and consequently

$$2\mathcal{A}(v)f_{st}(v) + C_1 = \mathcal{B}(v)\,\frac{\mathrm{d}f_{st}(v)}{\mathrm{d}v} + f_{st}(v)\,\frac{\mathrm{d}\mathcal{B}(v)}{\mathrm{d}v}, \tag{A.8}$$

where C_1 is the constant of integration. By separation of variables one obtains

$$2\frac{\mathcal{A}(v)}{\mathcal{B}(v)}\,\mathrm{d}v + \frac{C_1}{\mathcal{B}(v)f_{st}(v)}\,\mathrm{d}v = \frac{\mathrm{d}f_{st}(v)}{f_{st}(v)} + \frac{\mathrm{d}\mathcal{B}(v)}{\mathcal{B}(v)} \tag{A.9}$$

and after integration

$$2\int \frac{\mathcal{A}(v)}{\mathcal{B}(v)}\,\mathrm{d}v + \int \frac{C_1}{\mathcal{B}(v)f_{st}(v)}\,\mathrm{d}v + C_2 = \ln\left[f_{st}(v)\mathcal{B}(v)\right]. \tag{A.10}$$

Since f_{st} must tend to zero in the limits of $v \to \pm\infty$, the second integral diverges for any $C_1 \neq 0$. Thus, C_1 must be zero and (A.10) becomes

$$f_{st}(v) = \frac{1}{\mathcal{B}(v)}\exp\left(2\int \frac{\mathcal{A}(v)}{\mathcal{B}(v)}\,\mathrm{d}v + C_2\right). \tag{A.11}$$

Defining $C := \exp(C_2)$, one finally obtains

$$f_{st}(v) = \frac{C}{\mathcal{B}(v)}\exp\left(2\int \frac{\mathcal{A}(v)}{\mathcal{B}(v)}\,\mathrm{d}v\right), \tag{A.12}$$

where C is the normalization constant that is chosen such that $\int_{\mathbb{R}} f_{st}(v)\,\mathrm{d}v = m_0$, i.e.

$$C = m_0\left[\int_{\mathbb{R}} \frac{1}{\mathcal{B}(v)}\exp\left(2\int \frac{\mathcal{A}(v)}{\mathcal{B}(v)}\,\mathrm{d}v\right)\mathrm{d}v\right]^{-1}. \tag{A.13}$$

Substitution of the general functions with the advection and diffusion coefficients given in Section 5.1

$$\mathcal{A}(v) = \underbrace{-\gamma|v|\,v}_{\text{Drift-induced advection}} + \underbrace{\frac{\phi^2}{4}\mathrm{sgn}(v)}_{\text{Noise-induced advection}}, \tag{A.14}$$

$$\mathcal{B}(v) = \phi^2|v|, \tag{A.15}$$

and integration of the exponent in (A.12) yields

$$f_{st}(v) = \frac{C}{\phi^2\sqrt{|v|}} \exp\left(-2\frac{\gamma}{\phi^2}|v|\right), \tag{A.16}$$

where the normalization constant is

$$C = m_0 \left[\Gamma\left(\frac{1}{4}\right)\phi^{5/2}\gamma^{-1/4}\right]^{-1}. \tag{A.17}$$

Then the exact moments associated with (A.16) can be expressed as

$$m_{st,k} = \int_{\mathbb{R}} v^k f_{st}(v)\,\mathrm{d}v = \frac{1+(-1)^k}{2} C\,\Gamma\left(\frac{1+2k}{4}\right)\frac{\phi^4}{\gamma}\left(\frac{\gamma}{\phi^2}\right)^{(3-2k)/4}. \tag{A.18}$$

With the exact stationary NDF, closed expressions for the integrals in the moment equations can be derived. For the equilibrium state, (5.22) can be written as

$$\frac{\mathrm{d}m_{st,k}}{\mathrm{d}t} = 0 = \dot{m}^{(a,d)}_{st,k} + \dot{m}^{(a,n)}_{st,k} + \dot{m}^{(d)}_{st,k}, \tag{A.19}$$

where the terms on the RHS represent, from the left to the right, the change of the kth moment due to drift-induced advection, noise-induced advection and diffusion. For odd k all terms on the RHS of (A.19) vanish due to symmetry. For even k analytical integration yields

$$\begin{aligned}
\dot{m}^{(a,d)}_{st,k} &= -k\gamma \int_{\mathbb{R}} \mathrm{sgn}(v) v^{k+1} f_{st}(v)\,\mathrm{d}v \\
&= -Ck\,\Gamma\left(\frac{2k+3}{4}\right)\left(\frac{\gamma}{\phi^2}\right)^{(1/2-k)/2}, \\
\dot{m}^{(a,n)}_{st,k} &= k\frac{\phi^2}{4} \int_{\mathbb{R}} \mathrm{sgn}(v) v^{k-1} f_{st}(v)\,\mathrm{d}v \\
&= \frac{Ck\phi^2}{4\gamma}\,\Gamma\left(\frac{2k-1}{4}\right)\left(\frac{\gamma}{\phi^2}\right)^{(5/2-k)/2}, \\
\dot{m}^{(d)}_{st,k} &= k(k-1)\frac{\phi^2}{2} \int_{\mathbb{R}} \mathrm{sgn}(v) v^{k-1} f_{st}(v)\,\mathrm{d}v \\
&= \frac{Ck(k-1)\phi^2}{2\gamma}\,\Gamma\left(\frac{2k-1}{4}\right)\left(\frac{\gamma}{\phi^2}\right)^{(5/2-k)/2}.
\end{aligned} \tag{A.20}$$

A.5. Exactness of the Five-Node GaG-Quadrature for the Stationary Case

For a $(2n-1)$-node GaG-quadrature, $2n$ moments are required. Thus, in order to compute the five-node quadrature rule the first six moments must be known. For the steady-state solution, the exact moments are given in (5.63). They can be expressed as (considering the identity $\Gamma(x+1) = x\,\Gamma(x)$)

$$\begin{aligned} m_0 &= C\Gamma\left(\frac{1}{4}\right)\phi^{5/2}\gamma^{-1/4}, \\ m_2 &= \frac{1}{4}C\Gamma\left(\frac{1}{4}\right)\phi^{9/2}\gamma^{-5/4}, \\ m_4 &= \frac{5}{16}C\Gamma\left(\frac{1}{4}\right)\phi^{13/2}\gamma^{-9/4}, \\ m_1 &= m_3 = m_5 = 0. \end{aligned} \tag{A.21}$$

Application of the Wheeler algorithm [143, 170] with the given moments yields the recurrence coefficents of the first three polynomials orthogonal with respect to f_{st}:

$$\begin{aligned} &\alpha_0 = \alpha_1 = \alpha_2 = 0, \\ &\beta_1 = \frac{\phi^2}{4\gamma}, \quad \beta_2 = \frac{2\phi^2}{\gamma}. \end{aligned} \tag{A.22}$$

Thus, the modified Jacobi matrix can be written as

$$\mathbf{J}_3^* = \begin{pmatrix} \alpha_0 & \sqrt{\beta_1} & 0 \\ \sqrt{\beta_1} & \alpha_1 & \sqrt{2\beta_2} \\ 0 & \sqrt{2\beta_2} & \alpha_2 \end{pmatrix} = \frac{\phi}{\sqrt{\gamma}} \begin{pmatrix} 0 & 1/2 & 0 \\ 1/2 & 0 & \sqrt{2} \\ 0 & \sqrt{2} & 0 \end{pmatrix}. \tag{A.23}$$

Then, as described in Section 3.2, the nodes and weights of the Gaussian and the anti-Gaussian quadrature result from the eigenvalues and eigenvectors of $\mathbf{J}_2$ (the upper left 2×2 submatrix of $\mathbf{J}_3^*$) and $\mathbf{J}_3^*$, respectively. The resulting combined

GaG-quadrature rule is then (with averaged weights)

$$\begin{pmatrix} v_1 \\ v_2 \\ v_3 \\ v_4 \\ v_5 \end{pmatrix} = \frac{1}{2}\frac{\phi}{\sqrt{\gamma}} \begin{pmatrix} -3 \\ -1 \\ 0 \\ 1 \\ 3 \end{pmatrix}, \qquad \begin{pmatrix} w_1 \\ w_2 \\ w_3 \\ w_4 \\ w_5 \end{pmatrix} = \frac{m_0}{36} \begin{pmatrix} 1 \\ 9 \\ 16 \\ 9 \\ 1 \end{pmatrix}, \tag{A.24}$$

where even indices correspond to the Gaussian quadrature and odd indices correspond to the anti-Gaussian quadrature. Applying this quadrature rule, the integral terms on the RHS of the moment equations can be closed. Considering the analytical expressions in (A.20) for the integral terms in the stationary case, the quadrature error can be calculated for each term. Using the same superscripts as in (A.20) to indicate the drift-induced advection, noise-induced advection and diffusion, the errors in the second moment equation are

$$\begin{aligned} R^{(a,d)} &= \dot{m}_{st,2}^{(a,d)} - \sum_{j=1}^{5} -2w_j\gamma\ \mathrm{sgn}(v_j)v_j^3 = \frac{1}{2}\frac{m_0\phi^3}{\sqrt{\gamma}} - \frac{3}{2}\frac{m_0\phi^4\ \Gamma(3/4)}{\gamma\ \Gamma(1/4)}, \\ R^{(a,n)} &= \dot{m}_{st,2}^{(a,n)} - \sum_{j=1}^{5} 2w_j\frac{\phi^2}{4}\mathrm{sgn}(v_j)v_j = -\frac{1}{6}\frac{m_0\phi^3}{\sqrt{\gamma}} + \frac{1}{2}\frac{m_0\phi^4\ \Gamma(3/4)}{\gamma\ \Gamma(1/4)}, \\ R^{(d)} &= \dot{m}_{st,2}^{(a,n)} - \sum_{j=1}^{5} 2w_j\frac{\phi^2}{2}\mathrm{sgn}(v_j)v_j = -\frac{1}{3}\frac{m_0\phi^3}{\sqrt{\gamma}} + \frac{m_0\phi^4\ \Gamma(3/4)}{\gamma\ \Gamma(1/4)}. \end{aligned} \tag{A.25}$$

It is evident that none of the integrals is exactly represented by the quadrature, as expected. However, the errors cancel each other out, i.e.

$$R^{(a,d)} + R^{(a,n)} + R^{(d)} = 0, \tag{A.26}$$

which results in exact moments. The same is true for the fourth moment, though not explicitly shown here.

A.6. Computational Costs of the GaG-QMOM

It is stated in Chapter 5 that the proposed variation of the QMOM, namely the GaG-QMOM, causes only moderate computational overhead, which is illustrated in Figure A.3. It shows the computational costs of the GaG-QMOM in

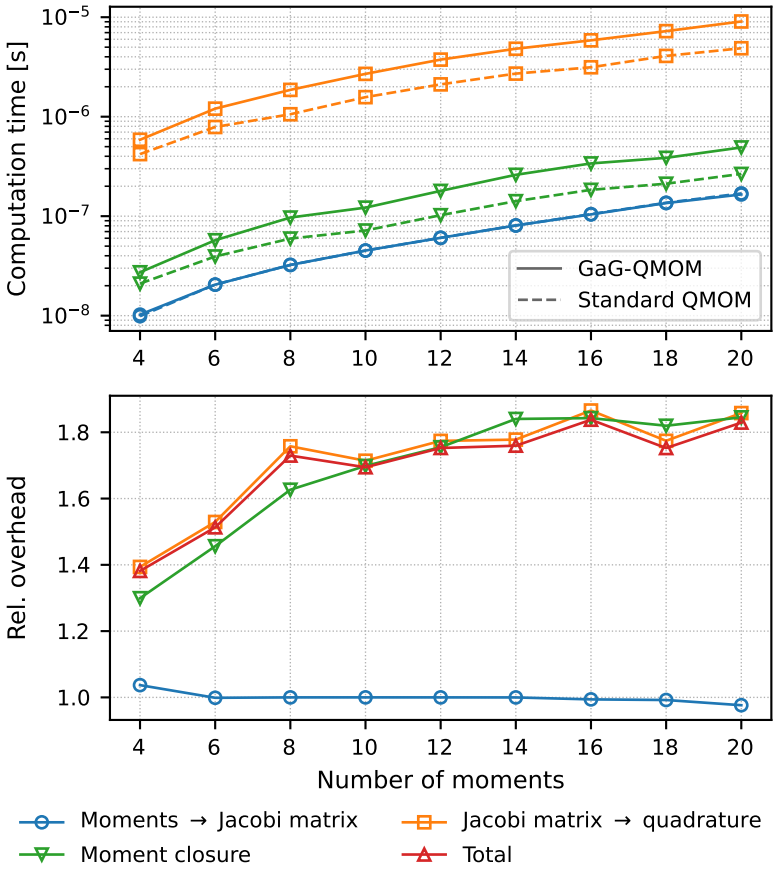

Figure A.3.: Computational costs of the GaG-QMOM compared to the standard QMOM in terms of the mean computation time (based on 10^4 executions per moment set) for each step of the moment closure algorithm (top) and the relative overhead, i.e. the factor by which the GaG-QMOM increases the computation time with respect to the standard QMOM (bottom).

terms of absolute computation time and relative computational overhead compared to the QMOM, using the same set of 10^5 test moments as in the numerical investigations in Chapter 6 and the system of moment equations derived from the Fokker-Planck equation with a constant drag coefficient (5.22). The maximum factor of increase in total computation time is shown to be about 1.8 when solving for 20 moments, which can be deemed moderate considering the gain in accuracy presented in Section 5.4. However, it should be noted that this factor depends on the underlying PBE. The overhead for more complex PBEs (possibly including second-order processes) can be estimated using the results in Section 6.3.3.

A.7. C++ Implementation for Performance and Accuracy Measurements

The source code that was implemented for the numerical study in Chapter 6 is available on

- GitLab: *https://gitlab.com/puetzm/qbmm-profiling-tools*,
- GitHub (mirror): *https://github.com/puetzmi/qbmm-profiling-tools*

The used configurations are provided on

- GitLab: *https://gitlab.com/puetzm/qbmm-profiling-study*
- GitHub (mirror): *https://github.com/puetzmi/qbmm-profiling-study*

Table A.1 lists the versions that were used to obtain the results presented in Section 6.3. Information on the versions of the most important third-party software and libraries used to develop and build the applications is given in Table A.2.

The results in Section 6.3 were produced by applications built with the *Intel®* compiler. To rule out compiler-specific effects that would limit the general validity of results, the *GNU* compiler was also tested on selected cases. Moreover, since most of the numerical investigations were conducted running multiple configurations simultaneously on six cores, it was ensured that the use of multiple cores does not lead to any bottlenecks resulting in substantial differences

Table A.1.: Code versions used for the different parts of the numerical study in Chapter 6.

Part of the numerical study	Version	Git commit hash
Subroutine I: Computation of the Jacobi matrix (Section 6.3.1)	v0.3.1	c26c03c
Subroutine II: Solution of the eigenvalue problem (Section 6.3.2)	v0.3.1	c26c03c
Relative contributions to computational costs (Section 6.3.3)	v0.3.2	0e453ec

Table A.2.: Versions of major third-party software and libraries used for the study in Chapter 6.

Software / library	Version
Intel® oneAPI Math Kernel Library	2022.2.0
LAPACK	3.10.1
Eigen	3.4.0
Intel® oneAPI DCP++/C++ Compiler	2023.0.0
GNU Compiler Collection	11.3.0

from the single-core computation, which would invalidate the measured computation times. Figure A.4 shows the executions per second for solving the eigenvalue problem (Subroutine II) comparing the performance of the *Intel®* build using one/six cores and the *GNU* build using six cores. It is evident that compilation with the *GNU* compiler as well as simultaneous computations on multiple cores result in a slightly decreased performance, though not to an extent that is significant with regard to the conclusions following from Chapter 6.

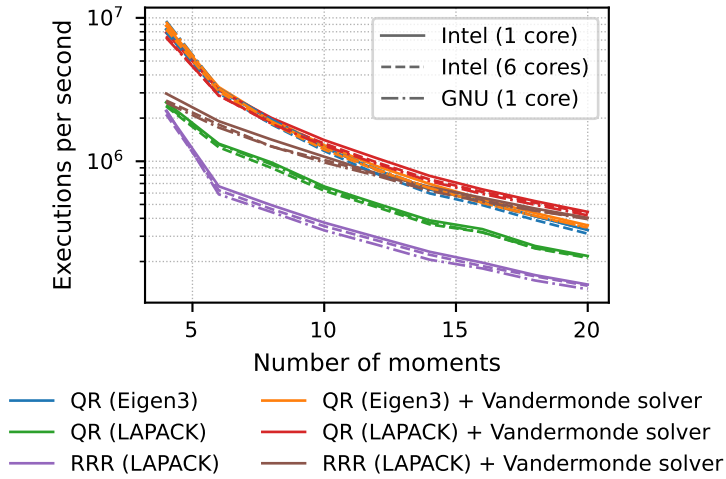

Figure A.4.: Number of executions per second of implementations to solve the eigenvalue problem (Subroutine II), built with different compilers and using different numbers of cores simultaneously.